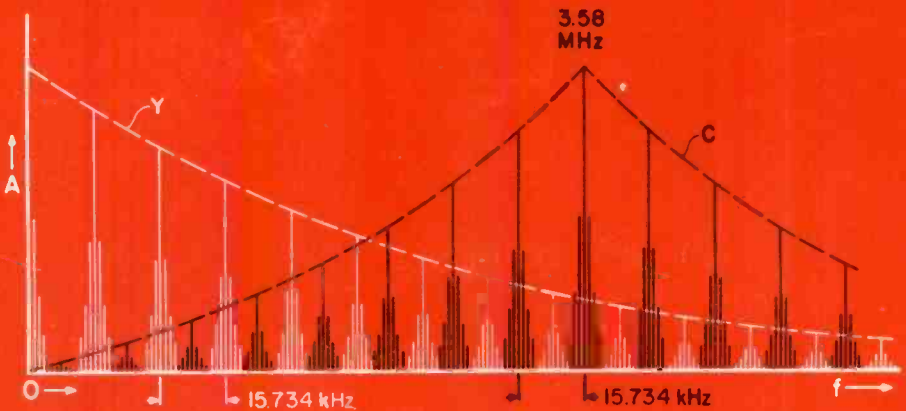


RCA Review

TO BE REMOVED FROM
NASA LIBRARY
AMES RESEARCH CENTER
JUN 9 1980
COPY NO. 1
MOFFETT FIELD, CALIF



March 1980

Volume 41 No. 1

The cover figure (Fig. 1 of the Pritchard paper in this issue) shows the interlaced nature of the luminance (Y) and chrominance (C) information in the basic NTSC signal. The first two papers in this issue of *RCA Review* describe the development of an innovative means for advantageously separating luminance and chrominance in a commercial TV receiver by employing CCD comb filter techniques.

RCA Review, published quarterly in March, June, September and December by RCA Research and Engineering, RCA Corporation, Princeton, New Jersey 08540. Entered as second class matter July 3, 1950 under the Act of March 3, 1879. Second-class postage paid at Princeton, New Jersey, and at additional mailing offices. Effective January 1, 1978, subscription rates as follows: United States and Canada: one year \$8.00, two years \$14.00, three years \$18.00; in other countries, one year \$8.60, two years \$15.20, three years \$19.80. Single copies (except for special issues) up to five years old \$3.00.

Contents

- 3 A CCD Comb Filter for Color TV Receiver Picture Enhancement**
Dalton H. Pritchard
- 29 Design and Performance of a CCD Comb Filter IC**
Donald J. Sauer
- Metaphosphate Glasses**
- 57 Introduction to Luminescent Glasses**
Tatsuo Takahashi
- 65 Fluorescent Properties of Alkali and Alkaline Earth Rare Earth Metaphosphate Glass Phosphors**
T. Takahashi and O. Yamada
- 92 Concentration Quenching of Luminescence in a Disordered System with Dipolar Interaction**
H. Fujita and M. Inoue
- 110 Luminescence of Certain Terbium Metaphosphate Glasses Under X-Ray Excitation**
T. Takahashi and O. Yamada
- 120 Thermal Properties of New Metaphosphate Glasses**
O. Yamada and T. Takahashi
- 127 Authors**
- 129 Patents**

RCA Corporation

E. H. Griffiths President and Chief Executive Officer

Editorial Advisory Board

Chairman, J. J. Tietjen RCA Laboratories

N. L. Gordon RCA Laboratories

G. C. Hennessy RCA Laboratories

E. O. Johnson RCA Research Laboratories, Inc.

H. Kressel RCA Laboratories

W. Merz Laboratories RCA, Ltd.

K. H. Powers RCA Laboratories

L. A. Sholliff International Licensing

T. O. Stanley, RCA Laboratories

W. M. Webster RCA Laboratories

Editor Ralph F. Ciafone

Associate Editors

D. R. Higgs Missile and Surface Radar Division

C. Hoyt Consumer Electronics

T. King RCA Research and Engineering

R. Mausler National Broadcasting Company

M. Rosenthal RCA Americom, Inc.

J. Schoen Solid-State Division

M. G. Pietz Government and Commercial Systems

W. S. Sepich Commercial Communications Systems Division

J. E. Steoger RCA Service Company

D. Tannenbaum Government Communications Systems

© RCA Corporation 1980. All rights reserved, except that express permission is hereby granted for the use in computer-based and other information-service systems of titles and abstracts of papers published in RCA Review.

A CCD Comb Filter for Color TV Receiver Picture Enhancement

D. H. Pritchard

RCA Laboratories, Princeton, NJ 08540

Abstract—The interlaced nature of the luminance and chrominance signal information contained within a common communications channel in the standard NTSC color television system allows the development of an innovative means for advantageously separating luminance and chrominance at the receiver by employing 1-H (one horizontal scan time) delay comb-filter techniques. The objective of this approach is to provide subjective picture quality and sharpness enhancement by minimizing the conventional "dot-crawl" and "cross-color" beats, increasing the horizontal resolution to at least 330 equivalent TV lines, and introducing the concept of vertical detail peaking at the receiver.

The introduction of charge-coupled-device (CCD) technology has made possible the development of a unique 1-H delay device configured in a comb-filter format and developed as a cost-effective integrated circuit that is appropriately interfaced into the baseband signal processing function of a color TV receiver.

1. Introduction

The advent of charge-coupled-device (CCD), NMOS, solid-state technology has made possible the development of a unique 1-H delay device configured in a comb filter format. A cost-effective integrated circuit (IC) has been developed to appropriately interface with the baseband signal processing functions of a color television receiver. Recognition of the interlaced nature of the luminance and chrominance information

contained within a common communications channel, such as the standard NTSC color television system, allows the development of an innovative means for advantageously separating luminance and chrominance at the receiver by employing comb filter techniques.

The objective of this approach is to provide subjective picture-quality and sharpness enhancement. The conventional "dot-crawl" and "cross-color" beats are minimized, the horizontal resolution is increased from the typical value of 260 to at least 330 equivalent TV lines, and the concept of vertical detail enhancement at the receiver is introduced.

The introduction of a new device with new performance capabilities in an imaging system requires a unified approach, since the performance of each function in the system is proportional to and affected by the performance of each of the other functions. In this context, the design of an electronic imaging system is surprisingly complex.

This general principle was applied to the problem of more effectively separating the luminance and chrominance signal components by comb filter techniques, as well as improving the transient response and available bandwidths of the luminance and chrominance signals as specified for NTSC color television.

The innovative CCD IC design that has been developed utilizes the principles of "charge-summation" in combination with a unique arrangement of a "long-line" delay and a "short-line" delay, the *difference* in delay being precisely the required 1-H time delay. A fundamental CCD relationship is that the delay is determined by the number of charge transfers and is inversely proportional to the clock rate. This, along with the linear phase characteristic of such a two-terminal transversal filter, results in an approach that is ideal from the points of view of stability, electrical performance, and freedom from environmental problems.

The inherent baseband characteristic of the CCD as a delay element also allows the introduction of vertical detail enhancement in the combed luminance channel. When this feature is coupled with appropriate nonlinear processing of the detail signal to include conventional horizontal peaking, the result is a surprisingly superior picture sharpness enhancement. This, when combined with the basic comb filter luminance and chrominance separation function, produces a picture whose improved "cleanness" and "sharpness" is recognizable by the average observer and that more nearly utilizes the capability of the NTSC color television system.

This paper gives an overview of the background, concepts, and principles involved in a successful research and development program aimed at improving visible color television picture performance. The details of the special integrated circuit design and fabrication as well as specific receiver circuit considerations are given in References [1] and [2].

2. Related NTSC System Fundamentals

A composite television signal may be described in terms of a sampled-data format in that it is periodic in nature as the result of it being interrupted, or sampled, at repetitive rates of 15.734 KHz, 60 Hz, and 30 Hz. Sampling occurs as a consequence of the horizontal and vertical scanning and blanking process. A Fourier analysis of the signal in the video domain indicates an energy spectrum concentrated in discrete clusters with interval spacings of 15.734 KHz, with sub-sidebands grouped around each 15.734 KHz interval at multiples of 60 Hz and 30 Hz spacing.³ A second signal, such as the color subcarrier and its modulation sidebands in a standard NTSC format, having its own periodic energy spectrum due to sampling (blanking) may be interleaved with the baseband spectrum by synchronizing the subcarrier with horizontal sync as an odd-multiple of one-half line rate. The value chosen in the case of NTSC is 3.579545 MHz. An example of this interleaved relationship in the case of an average signal content is indicated in Fig. 1.

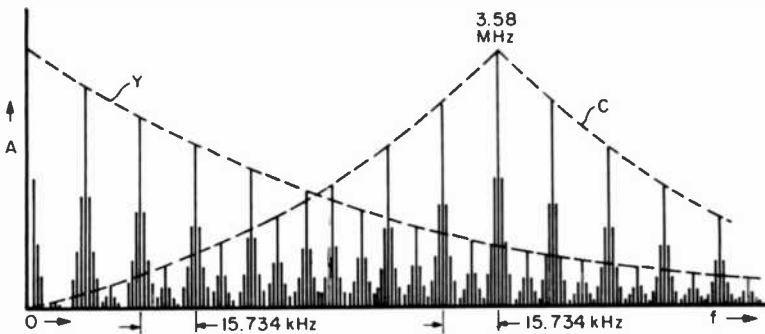


Fig. 1—Basic NTSC interleaved signal relationship.

The derivation of the NTSC specific line, field, and color subcarrier frequencies is as follows:

$$f_{FIELD} = \frac{f_{LINE}}{525/2} \text{ Hz} = 59.94 \text{ Hz} \quad [1]$$

$$f_{LINE} = \frac{4.5 \times 10^6}{286} \text{ Hz} = 15,734.26 \text{ Hz} \quad [2]$$

$$f_{sc} = \frac{13 \times 7 \times 5}{2} \times f_{LINE} \quad [3]$$

$$f_{sc} = \frac{455}{2} \times \frac{4.5 \times 10^6}{286} = 3.579545 \text{ MHz.} \quad [4]$$

Traditionally in NTSC color TV receiver design, where chrominance information is carried by means of such an interlaced subcarrier, the separation of chrominance information from luminance information has been accomplished by the use of over-lapping low-pass (luminance) and band-pass (chrominance) filters, as indicated in Fig. 2. These filters are relatively simple in format and cannot discriminate between luminance and chrominance signal components. The result is image quality degradation in the form of "cross-color" and "dot-crawl" along with certain bandwidth restrictions and transient response problems that result in overall system performance limitations.

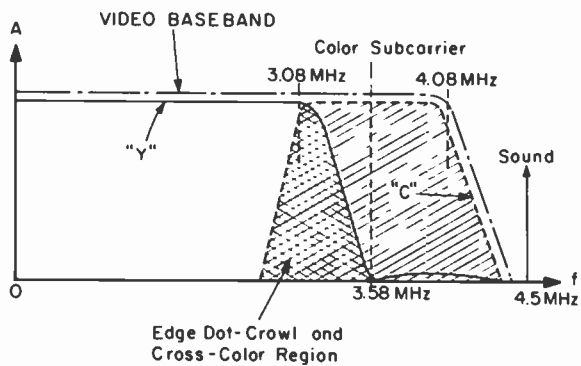


Fig. 2—Conventional NTSC luminance and chrominance separation filters.

Dot-crawl is the term used to describe the visibility of the cycles of the color subcarrier signal components contaminating the luminance channel. The subcarrier interlace provides a 180° line-to-line phase reversal of the color subcarrier, which in a perfectly linear system would cancel. In the actual case, however, due to system nonlinearity, the dot visibility is a function of the chrominance signal amplitude relative to the luminance (saturation). The dot motion is a consequence of the frequency relationship of the color subcarrier to the vertical field 2-to-1 interlace and the odd number (525) of lines.

"Cross-color" is a term used to describe the converse situation, i.e. the contamination of the chrominance signal due to high frequency luminance detail energy included in the chrominance band-pass filter frequency range. As a consequence of the color decoding process, these non-synchronous components are translated to low-frequency (0-500 KHz) color beat patterns on the edges of scene objects and on repetitive patterns. These beats are very visible and subjectively undesirable.

The luminance detail information occupies the same portion of the

frequency spectrum as the color subcarrier and its modulation sidebands. Thus, elimination of the visibility of the color subcarrier dot-crawl in large area color objects requires the use of a rejection trap tuned to 3.58 MHz in conventional receiver design. This procedure results in a luminance resolution limit of about 260 lines, along with potential transient response problems. Dot-crawl due to chrominance sideband energy is not eliminated at color edge transition areas and is therefore still visible.

In addition to these performance deteriorations, the conventional filter techniques require careful engineering practices to avoid excessive phase and/or amplitude transient response distortions that would result in improper edge-color reproduction (color quadrature distortion). The luminance bandwidth restriction manifests itself as "soft" pictures. The desire to improve this situation in a practical as well as cost-effective manner has long been a research and design goal.

3. Basic Comb-Filter Operation

It is apparent that a filter whose passband and stopband characteristics are periodic in character, resembling the teeth of a comb with appropriate spacing, would be more effective in separating the luminance and chrominance components that make up the NTSC signal. Such a filter, and its complementary form, overcomes some of the performance limitations inherent in the conventional separation techniques involving overlapping low-pass and band-pass filters.

The basic principles for the formation of such a filter have been recognized for decades, as has its potential application to television signal processing.⁴ Therefore, the fundamentals will only be briefly reviewed, with the emphasis being placed upon a specific, innovative, implementation in the form of the new charge-coupled-device (CCD) technology. This approach contains certain attendant advantages in an integrated circuit format that makes its application to NTSC color television receiver development of particular interest.

A two-terminal transversal filter configured as shown in Fig. 3 provides the desired comb-filter response when appropriately implemented. The fundamental comb-filter circuit consists of a delayed path and a direct path with appropriate linear summation and subtraction processing circuitry. If the amplitudes of the signals through the delayed path are made equal to the amplitudes of the same signals through the direct path, while maintaining a constant time-delay difference across the frequency band of interest, a linear summation process results in cancellation of interlaced components and reinforcement of the noninterlaced components. Conversely, subtraction (obtained by inverting one signal path

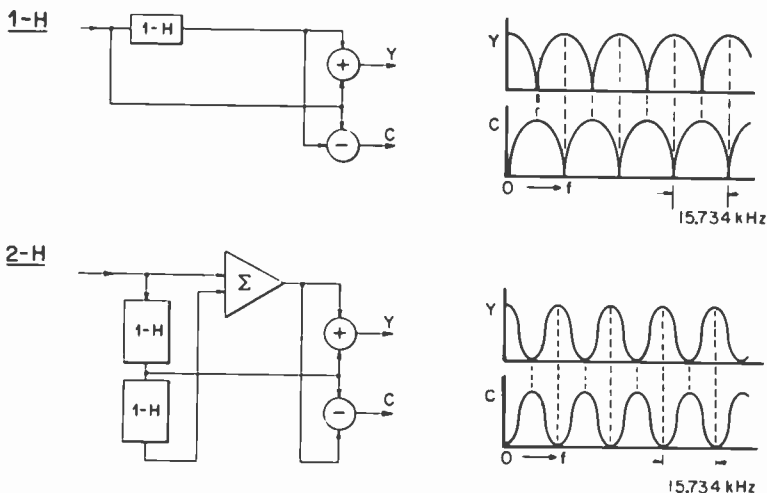


Fig. 3—1-H and 2-H comb filter diagrams.

followed by summation) results in cancellation of the noninterlaced components and reinforcement of the interlaced components.

The basic formation of a comb filter has been described in many ways, but perhaps the most straightforward approach is to employ a phasor concept. The input signal may be represented by a sinusoid as follows:

$$E_{IN} = E \cos \omega t \quad [5]$$

$$E_{IN} = E \cos 2\pi f_s t \quad [6]$$

$$E_{IN} = E \cos 2\pi N f_H t, \quad [7]$$

where

f_s = Specific signal frequency

f_H = Horizontal scan frequency

N = Variable coefficient relative to the delayed path.

Therefore, the instantaneous frequency is determined by Nf_H . In Fig. 4(a), the signal is split into two paths, with one path having no delay and the other path having a delay of τ , which is equal to $1/f_H$. The two signals are then combined in a linear fashion, after reduction to one-half amplitude, in separate adder and subtractor functions. The result is shown by the expression

$$E_{out} = \frac{E}{2} \cos 2\pi N f_H t \pm \frac{E}{2} \cos (2\pi N f_H t + 2\pi N). \quad [8]$$

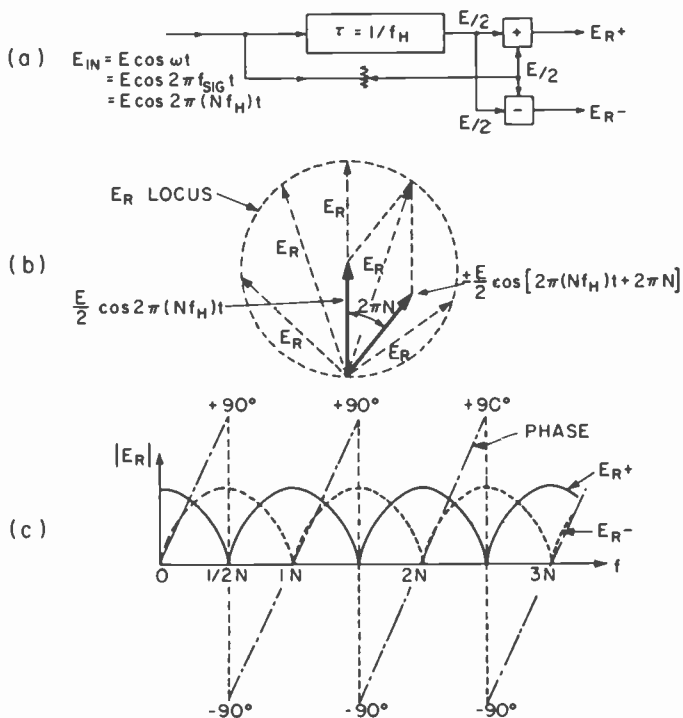


Fig. 4—Basic operation of a 1-H comb filter (phasor diagram).

In order to visualize the results of these combining functions, it is convenient to represent the signal in the direct path as a stationary phase reference vector and the signal from the delayed path as an equal amplitude rotating phase vector whose phase angle relative to the reference vector at any instant is $2\pi N$. Fig. 4(c) indicates the absolute value of the results of such vector summation (solid curve) as well as the vector subtraction (dotted curve). Since N is proportional to frequency, the periodicity of the resulting comb-shaped response has peaks that occur at integral values of N and nulls that occur at odd multiples of $N/2$. In the case of the application to NTSC color television, the value of f_H is made equal to the horizontal scanning frequency and the delay is equal to $1/f_H$ (typically referred to as 1-H delay).

Fig. 4(b) indicates the locus of the vector summation of the direct and delayed signals, while Fig. 4(c) shows the absolute value of the resultant (frequency response) of such a filter along with the linear phase characteristic. Figs. 5(a), 5(b), and 5(c) show the function diagram, phasor summations, and characteristics for a 2-H comb filter circuit resulting

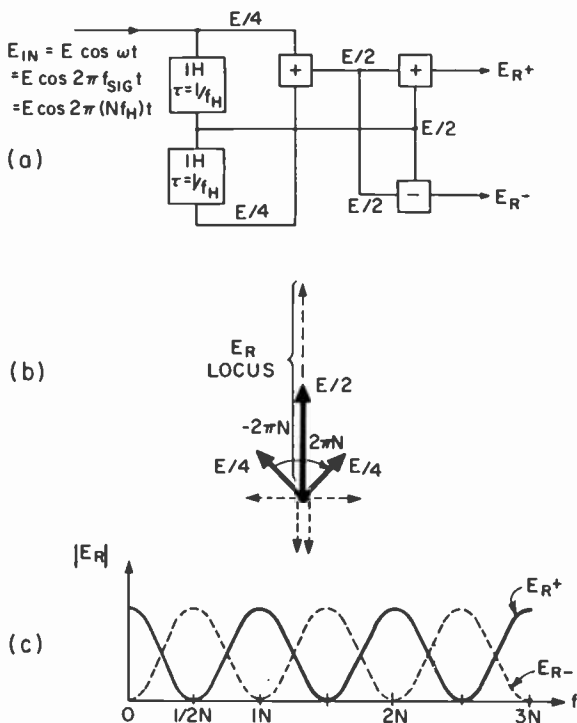


Fig. 5—Basic operation of a 2-H comb filter (phasor diagram).

in an off-set sinusoid response as opposed to the relatively sharp cusp-like response of a 1-H comb filter configuration.

Other than the obvious differences in circuit complexity, there is a tradeoff between timing stability required for a given degree of unwanted-signal rejection and the rejection of sideband signal components due to the sharp, cusp-shaped, response of a 1-H comb relative to the sinusoidal shape of a 2-H comb response. Fig. 6 indicates this relationship.

Fig. 7 is a visualization of the combing process for a signal that is purposely interlaced as an odd multiple of a one-half the horizontal scan rate, such as the color subcarrier in the NTSC system. The summation process reinforces the subcarrier and cancels the luminance (non-interlaced) components, thereby eliminating dot-crawl and cross-color contamination. However, the combing process results in a loss of resolution in the luminance channel at specific spatial angles of the scene content. This spatial angle is determined by the time period, as measured in the horizontal direction from one line to the succeeding line, required

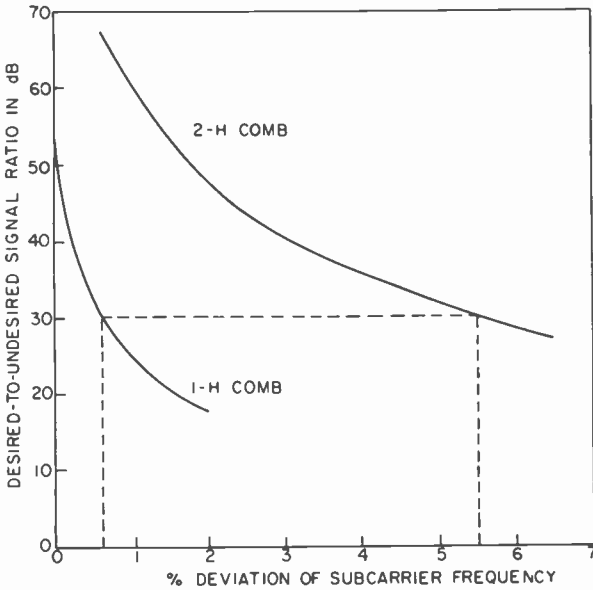


Fig. 6—Comb filter rejection ratio comparing 1-H and 2-H configurations versus carrier frequency stability.

for the signal content to reach a 180° line-to-line relationship. In the case of standard NTSC with a subcarrier of 3.58 MHz this angle for maximum loss is approximately $\pm 45^\circ$. Correspondingly, at this angle, the chrominance channel subtraction process does not cancel, and cross-color still exists. Thus, the spatial-angle spread over which the resolution loss and

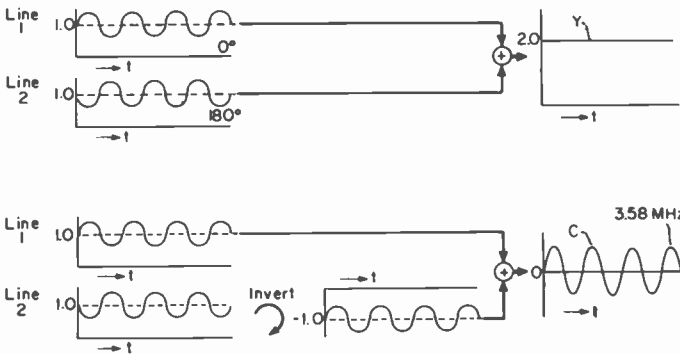


Fig. 7—Comb filter fundamental process relative to interlaced signals.

cross-color contamination exists is smaller for the 1-H cusp-shaped response as opposed to the 2-H sinusoidal response.

The overall quality of the reproduced picture formed from a signal that has undergone a comb filtering process is excellent. However, all of the aforementioned features and tradeoffs must be considered in developing optimum performance as well as cost-effective comb filter systems.

4. Vertical Detail Enhancement Concept

If the assumption is made, as in Figs. 3 and 7, that the combing process is allowed to extend from zero to an arbitrary high frequency, it should be apparent that the integration of two successive line periods results in (1) a 3-dB improvement in signal-to-noise ratio (4.25 dB in the case of 2-H, 3-line integration, comb systems) and (2) the loss of one-half of the *vertical* resolution of the scene content since the first null in the summation channel (luminance) occurs at one-half horizontal period (7.8 KHz). It should also be apparent that to adequately separate chrominance signal information from the luminance signal information, the combed frequency range could simply be limited to approximately 500 KHz on either side of the color subcarrier, thereby leaving the low-frequency vertical detail components untouched.

If, on the other hand, the combing function is allowed to extend down to zero frequency, the low-frequency combed output of the chrominance channel consists of exactly the vertical detail components that are removed from the luminance signal within approximately the first 1.0 MHz. A performance advantage may be realized by re-inserting the major portion of the vertical detail content (approximately 0-1.0 MHz) from the chrominance comb output into the luminance channel to a degree sufficient to restore the vertical resolution to normal. Then, simply by increasing the level of the restoration signal components beyond the normal value, vertical detail enhancement may be provided. This feature may be utilized, along with appropriate nonlinear processing, to produce an observable picture sharpness improvement.

The concept of vertical peaking has been employed in television camera chains and in broadcast-quality signal processing apparatus for some time. Typically, this equipment uses relatively expensive glass acoustic delay elements and discrete-component processing circuitry. As will be shown, the development of CCD devices in 1-H delay and comb-filter signal-processing format allows, for the first time, a cost-effective means for introducing vertical detail enhancement in a consumer color television receiver.

Figs. 8, 9, and 10 indicate the principles involved and the basic means

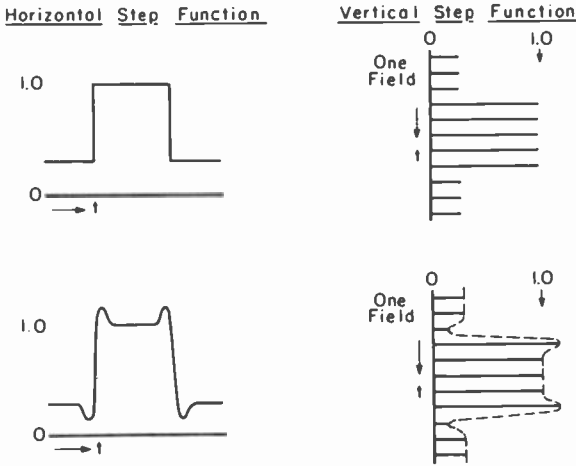


Fig. 8—Horizontal and vertical aperture correction.

for implementing vertical horizontal sharpness enhancement in a comb-filter signal-processing system. Horizontal peaking is accomplished by increasing the high-frequency energy content relative to that of the lower frequencies in a linear-phase circuit. Vertical peaking may be accomplished by recognition that the lower-frequency components of the baseband combed chrominance signal constitute the vertical detail information. This information must be restored, over approximately 0–1.0 MHz bandwidth, to the combed luminance to prevent loss of vertical

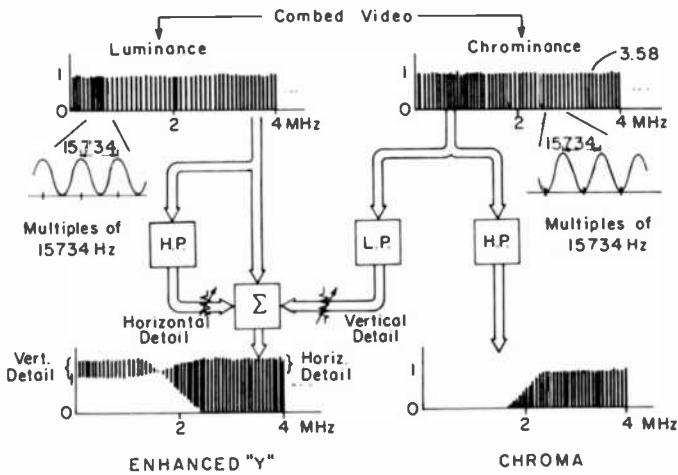


Fig. 9—Comb filter horizontal and vertical peaking system.

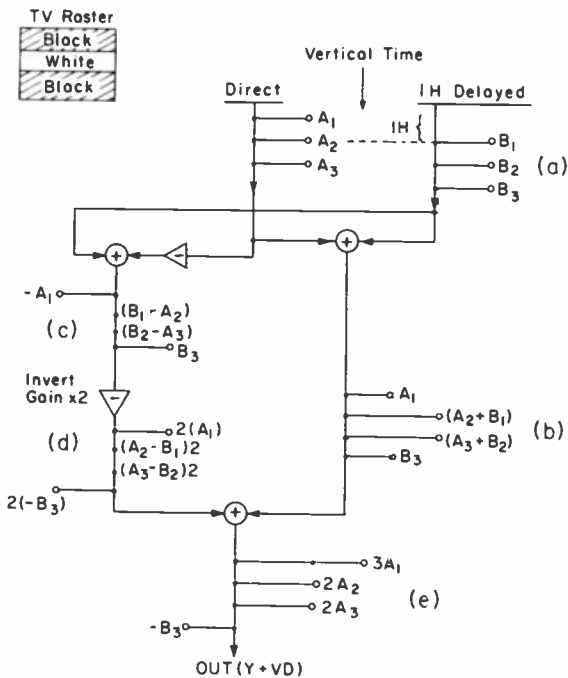


Fig. 10—1-H comb filter plus optimum vertical detail summation.

detail by the line-to-line "averaging" of the combing process. It then becomes a simple matter to add more vertical detail signal in order to enhance the transitions in the vertical direction. In the actual implementation, it is extremely important to process the detail information nonlinearly before re-insertion into the luminance channel to improve performance relative to noise, kine spot blooming, inter-line flicker, and co-channel interference effects. Fig. 11 indicates a typical vertical detail signal channel transfer characteristic deemed effective for best subjective picture performance.

Visualization of the concept of vertical detail signal generation and re-insertion may be accomplished by the approach indicated in Fig. 10. A scene comprising a white horizontal bar against a black background is assumed, with time processing downward in the diagram and light intensity increasing from left to right. The individual lines for the white bar are designated $A_1, A_2,$ and A_3 (a). The lines for the same signal delayed by a 1-H period are designated $B_1, B_2,$ and B_3 . The comb filter summation and subtraction processes result in the signals as shown at (b) and (c). The equivalent rise time, integrated over two line periods,

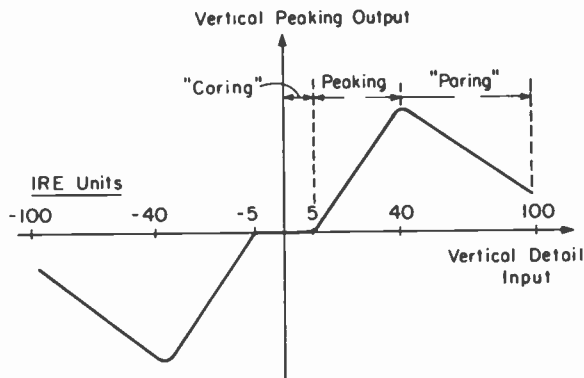


Fig. 11—Vertical detail nonlinear transfer function.

has been reduced by a factor of two at (b). The vertical-edge-detail signal is shown at (c). After polarity inversion (d), the vertical detail is re-inserted by an excess amount resulting in non-symmetric (in the case of a 1-H system) enhancement of the top and bottom transitions of the white bar. The additional polarity inversion and technical points-of-view in the case of 1-H comb filter systems. The subjective advantage results from the appearance of the scene being illuminated from above as opposed to from below, while a technical advantage occurs because the "main" portion of the white bar traverses the direct path of the comb filter circuit, as opposed to the delayed path, thereby avoiding any possible deterioration that might occur in the delay element. In 2-H systems, the peaking is symmetrical on the top and bottom of the transition (Fig. 8).

5. Application of Comb Filter Principles to Color TV Receiver Signal Processing

In the NTSC commercial color television system, the luminance and chrominance signal content may be separated more effectively by use of a 1-H delay device configured as a comb-filter than by conventional receiver techniques. This approach takes advantage of the interlaced nature of the color subcarrier in the standard system format. The luminance information is carried by the noninterlaced frequency components that have the same phase on succeeding scan lines and that are integral multiples of the horizontal scan frequency. Conversely, interlaced frequencies are those whose components are exactly 180° out of

phase on succeeding scan lines. These frequencies are odd multiples of one-half horizontal line frequency and represent the chrominance information.

In the formation of a comb filter for NTSC signals, the delay element is made to be precisely equal to one horizontal line time ($1H = 63.555 \mu s$). Thus, the linear adder circuit output contains only luminance information free of interference effects (dot-crawl) from the color subcarrier and its modulation sidebands. Similarly, the subtractor circuit output consists of the chrominance signal free of cross-color beat contamination (except at about $\pm 45^\circ$ spatial angles) that results from high frequency luminance detail entering the chrominance demodulation process.

The visual performance advantages are:

- (1) the elimination of color subcarrier dot-crawl from the luminance channel in large color areas as well as on signal transitions without the necessity for using a rejection trap at 3.58 MHz with its attendant bandwidth restriction;
- (2) realization of the horizontal resolution out to the system limit of 330 equivalent TV lines as opposed to the conventional value of 260 lines;
- (3) the elimination of cross-color beats on edges (except at 45° spatial frequency content where line-to-line cancellation cannot occur);
- (4) 3.0 dB or 4.25 dB (1-H or 2-H system) improvement in signal-to-noise ratio;
- (5) and the option of introducing vertical aperture compensation and/or peaking for purposes of further picture sharpness improvement.

The last item above is available as a consequence of using the charge-coupled-device approach, whose operating characteristics allow total baseband combing, as contrasted with glass acoustical delay elements that are typically limited to band-pass frequency response centered around the 3.58 MHz subcarrier. Thus, the low frequency (0-1 MHz) vertical detail signal components are available from the combed chrominance channel to be used for vertical detail enhancement purposes. Appropriate external low-pass and band-pass filters provide the interface with conventional luminance and chrominance signal processing receiver circuits.

The reinsertion of the vertical detail signal into the luminance channel is accomplished after passing the vertical detail signal components through a specific nonlinear transfer function. This nonlinear processing provides (1) "coring" of the low-level signal transitions to improve noise and provide co-channel interference rejection; (2) restoration of vertical detail scene content to normal during the coring process to prevent visible loss of vertical detail; (3) vertical peaking in all mid-range vertical

transitions to provide picture sharpness enhancement; and (4) "paring" of maximum dynamic range transitions to prevent excessive kinescope spot blooming and reduce inter-line flicker effects especially on diagonal scene content. During the overall receiver system development, considerable effort went into the choice of the specific nonlinear characteristic to obtain optimum picture quality improvement. A description of the details of this function and circuit implementation may be found in Ref. [1].

Another feature of the system integration into the complete receiver design involves appropriate time delay matching of the luminance, vertical detail, and chrominance signals. As an aid to this process, two additional CCD delay elements (186 ns) are included in the combed luminance channel internal to the CCD IC. This, when combined with the external 4.0 MHz luminance channel low-pass filter, results in matching the delay introduced by the 1.0 MHz vertical detail signal low-pass filter. In turn, this total delay, coupled with the luminance channel transversal peaking filter delay, determines the design of the chrominance channel band-pass ("peaker") filter to match the timing of the luminance and chrominance signals at the summation points in the R, G, B matrix function.

An additional system problem solved in the overall receiver development program relates to the containment of high-frequency harmonic radiation generated by the fast rise-time clock signal and clock-logic circuits in the IC. These components could cause interference to the operation of other functions within the total system. The sources of the harmonics were first identified, then successfully reduced and/or contained by means of electrical filtering, mechanical shielding, and judicious physical layout of the circuit to minimize high-frequency current loops and to provide an adequate ground-plane reference. The most critical paths to contain and/or effectively filter are the V_{CC} and V_{DD} supply current loops.

The results of the design of the CCD comb filter IC to properly interface with a specific receiver signal-processing system in a unified approach provide optimum overall system high performance in a reliable, cost-effective manner.

6. CCD Operation as an Analog Delay Comb Filter IC

The comb filter approach exploits the potential of charge-coupled device technology to provide the 1-H delay device coupled with the necessary processing functions in an IC format. The CCD device has the inherent advantages of being baseband and of having at least 4 MHz of useable bandwidth, along with electronically adjustable linear-phase delay ac-

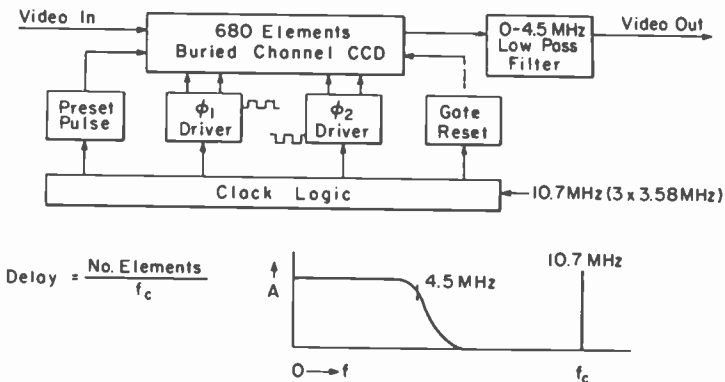


Fig. 12—Basic CCD operation.

completed simply by precise control of the clock frequency (see Fig. 12).

Development of the charge-coupled devices utilizing NMOS, buried-channel, two-phase, technology in an IC format was coordinated with the receiver system interface development in parallel programs. The resultant unified design, in accordance with previously stated principles, insured a high probability of success in a reasonable developmental time frame.

Fig. 13 indicates the manner in which the CCD IC is integrated into the baseband signal processing functions of the color television receiver. The 1-H comb filter IC is fabricated in a 22 pin, dual in-line, plastic

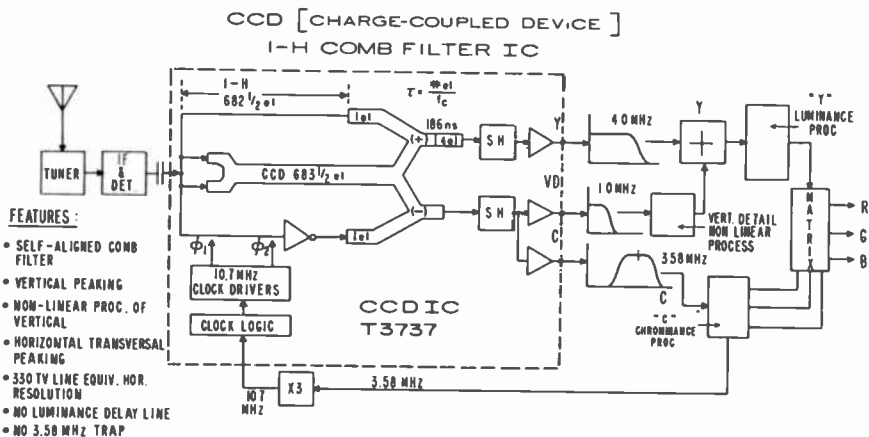


Fig. 13—"Dynamic Detail Processor" function diagram.

package that accepts a composite NTSC color video signal at its input terminal. It produces, at its output terminals, combed separation of chrominance and luminance information together with a second chrominance channel output intended to supply the vertical detail signal. The commercial version also accepts a clock signal input of 10.74 MHz from an external limiter-multiplier circuit. This sinusoidal clock signal is derived from the local 3.579545 MHz color subcarrier synchronized from the standard "color burst" signal.

A significant feature of the CCD IC design is the concept of utilizing parallel input signal paths in one long and two short CCD delay lines using common clock drive.⁵ Thus, the *difference* in delay between the long and short lines determines the effective delay of 1-H. This, in turn, establishes the frequency intervals between the teeth of the comb which are substantially independent of environmental factors and are precisely related to the number of delay stages and the clock frequency. In the specific case of NTSC, with a clock frequency of three times the color subcarrier, the long line contains 683.5 elements while the two short lines consist of one stage each. This results in a *differential* of 682.5 elements necessary to produce the 63.555 μ s effective delay for the 1-H time period as in the following relationship:

$$\text{Delay} = \frac{\text{Number of Elements}}{\text{Clock Frequency}}$$

Such factors as input-signal finite sampling time and modulation-transfer-function (MTF) response, directly related to the value of ϵ (transfer inefficiency), can affect the relative delay of the long versus short lines. A minimum value of $\epsilon = 5 \times 10^{-5}$ is required, with even better ϵ being achieved in practice. Good design and fabrication process control minimizes those variables that may result in differential delay errors of 4 to 5 ns or less. These values are entirely adequate to retain the necessary comb null depths (-30 to -40 dB) across the frequency band of interest.

Another highly important feature of the CCD IC design is the provision for obtaining the two required summation processes by "split-channel" and "charge-summation" techniques. Thus, only a slight relative amplitude trim adjustment is provided to obtain comb null depths of 40 dB or greater. The two amplitude trim adjustments, one for the luminance comb and one for the chrominance comb, are the only external IC controls required.

The output amplifier channels include sample-and-hold circuits to minimize the external filter requirements in reducing clock signal contamination. This process results in a $\sin x/x$ response with a null at the clock frequency of 10.74 MHz. The output source followers are designed

to interface with appropriate external filters. Automatic input-signal CCD biasing circuitry is incorporated that utilizes on-chip reference shift-register elements such that optimum performance of the CCD delay elements are controlled without the necessity for critical external bias adjustments.

In order to produce a viable IC device, clock-driver and clock-logic circuitry capable of operating at the desired clock frequency of 10.74 MHz (three times the system reference frequency of 3.58 MHz) were developed and incorporated on-chip.

In early developmental versions, a phase-locked-loop (PLL) circuit was incorporated on-chip to perform the function of converting 3.58 MHz to the desired value of 10.74 MHz. However, the final version eliminated the on-chip PLL, and the 10.74 MHz is externally generated by limiting the 3.58 MHz reference to create the third harmonic. Then sufficient selectivity at 10.74 MHz in an external LC circuit is provided to drive the IC clock circuits directly. This approach insures that no stray coupling or internally generated 3.58-MHz reference signal contamination components can appear in the combed signal outputs.

Fig. 14 is a photograph of the IC indicating the serpentine layout of the CCD along with the associated circuitry. A detailed discussion of the IC circuit design and fabrication technique may be found in Ref. [2].

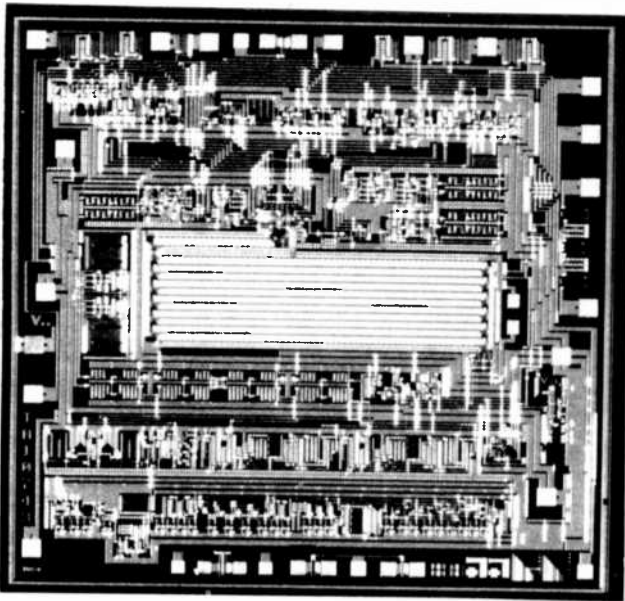
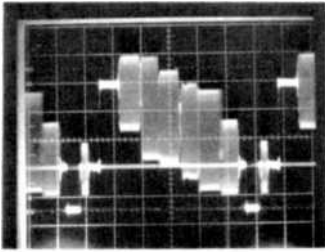
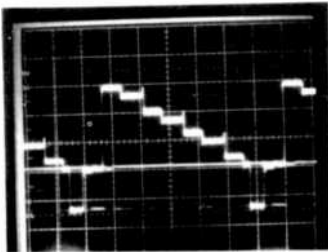


Fig. 14—Photo of CCD comb filter IC.

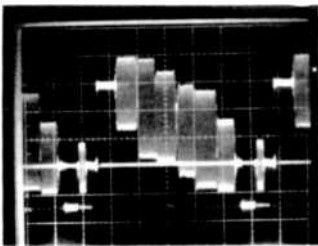


VIDEO INPUT
NTSC COLOR BARS

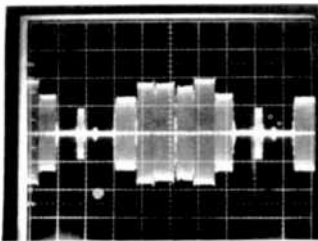


COMBED LUMINANCE
OUTPUT — AFTER
LO-PASS FILTER

Fig. 15—Luminance comb output for color bar signal.

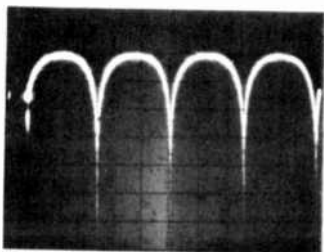


VIDEO INPUT
NTSC COLOR BARS

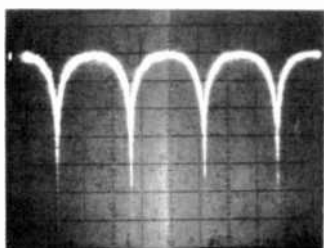


COMBED CHROMINANCE
OUTPUT — AFTER
LO-PASS FILTER

Fig. 16—Chrominance comb output for color bar signal.



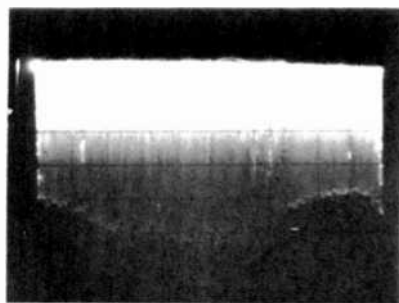
LUMINANCE OUTPUT
(Expanded Scale)
Vert.: 10 dB/div.
Center Freq.: 3.58 MHz



CHROMINANCE OUTPUT
(Expanded Scale)
Vert.: 10 dB/div.
Center Freq.: 3.58 MHz

Fig. 17—Comb response (expanded view).

Figs. 15, 16, 17, and 18 are oscilloscope pictures indicating the comb filter performance of the CCD IC. Fig. 15 shows the luminance comb output and Fig. 16 the chrominance comb output for a color-bar signal input. Fig. 17 shows an expanded view of the luminance and chrominance comb response. Fig. 18 is an overall sweep response from 0 to 5 MHz showing the envelope of the MTF response resulting from both ϵ and $\sin x/x$ characteristics, as well as the resulting comb null depths over the band.



Vert.: 10 dB/div.
Hor.: 0-5 MHz

Fig. 18—Overall 0-5 MHz comb response.

7. Picture Performance Improvements

Figs. 19 through 24 are photographs taken from an operating comb filter system that indicate the basic features realized by a comb filtering process and the inclusion of both vertical and horizontal picture sharpness improvement.

Fig. 19 is an enlarged portion of a color bar picture indicating the 3.58 MHz dot-crawl structure in color areas of the scene in a conventional system. Fig. 20 is the same portion of the scene after it has been processed by a comb filter showing the elimination of the dot structure. Note the one line dot structure remaining at the vertical transition between full-color and no-color signal content. The amplitude of these dots is $1/2$ for 1-H combs and $1/4$ for a 2-H system. The subjective visibility of such effects may be reduced to a satisfactory degree by controlling the overall frequency response relationship or by automatic sensing control means, as desired.

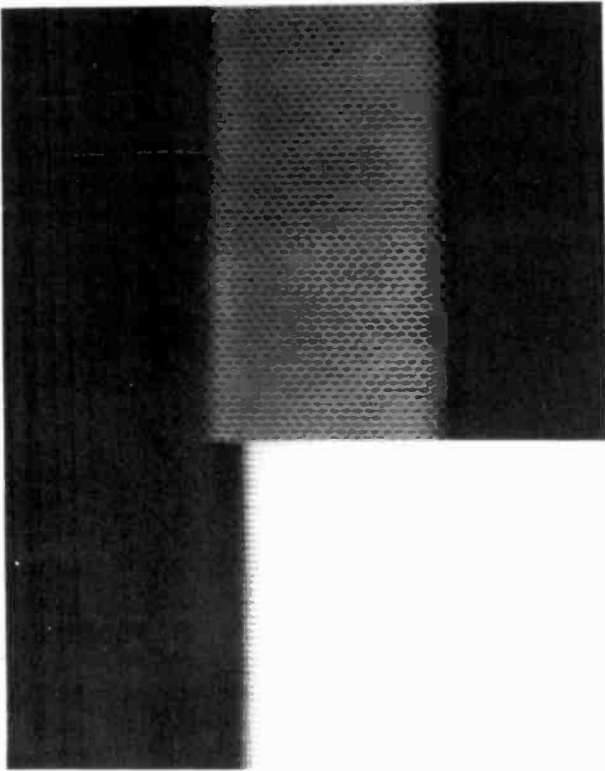


Fig. 19—Color bars in a conventional system showing dot-crawl.

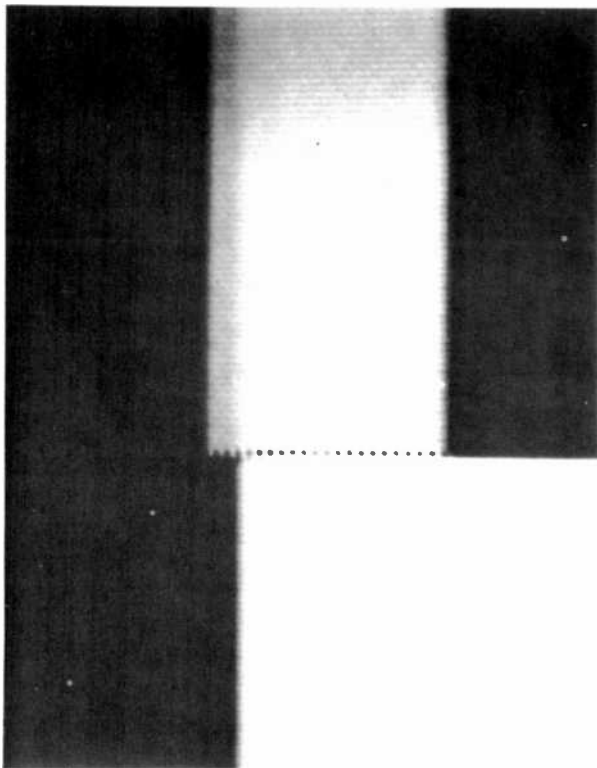


Fig. 20—Color bars in a comb filter system.

Fig. 21 is an indication of the cross-color beats that occur in the conventional approach. In actuality, these beats are reproduced in color and have a high order of visibility as crawling edges (zipper effect) or as moire patterns when repetitive signal content exists (umpire striped shirt effect). These beats consist of high-frequency luminance signal content that is allowed to enter the color demodulation process and is converted to low-frequency (0–500 KHz) nonsynchronous color content on picture edge transitions. Fig. 22 indicates the considerable reduction of these spurious beats after processing by a comb filter system. Note that some beats at 45° are not removed by the comb filter. These beats occur when signal content exists at a spatial angle of about 45° , as previously discussed.

Fig. 22 also shows the additional horizontal resolution realizable in the comb filter system because no 3.58 MHz trap is required.

Fig. 23 indicates the existence of both horizontal peaking and 2-H

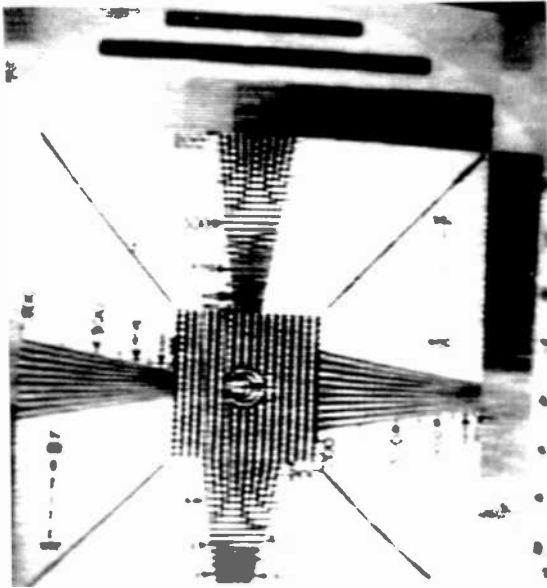


Fig. 21—Test pattern in a conventional system showing cross-color beats.

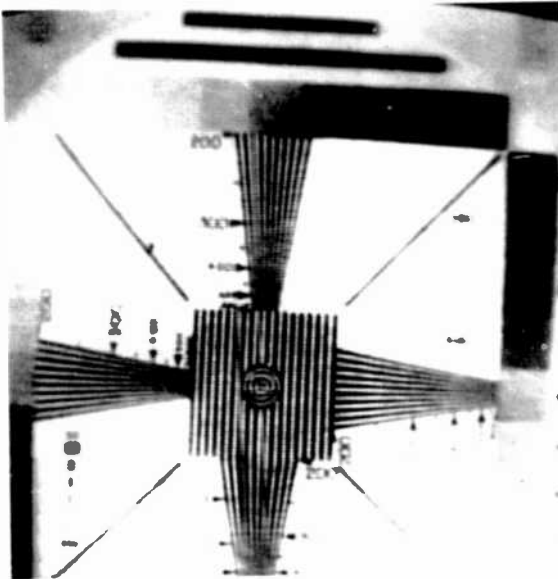


Fig. 22—Test patterns in a comb filter system.

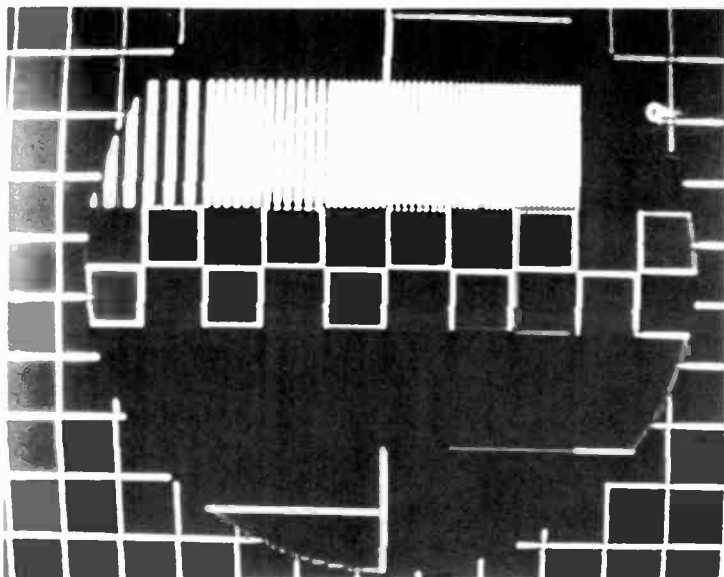


Fig. 23—Pattern generator with 2-H vertical and horizontal peaking.

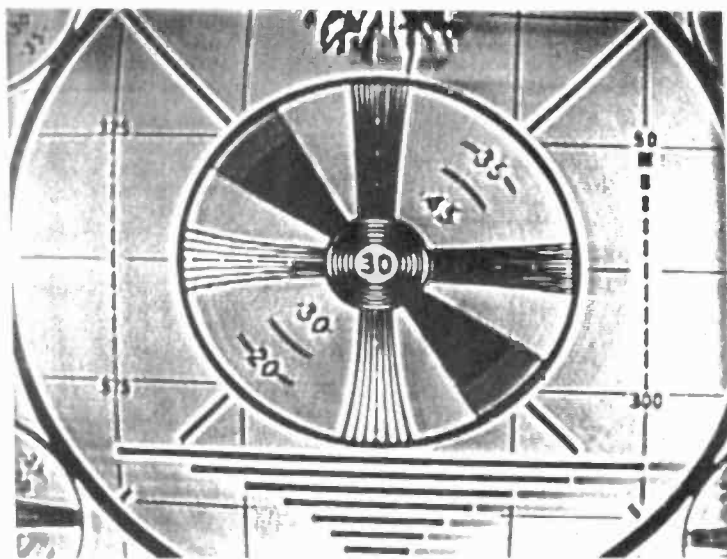


Fig. 24—Conventional test pattern with 2-H vertical and horizontal peaking.

comb filter vertical enhancement, as shown by the vertical and horizontal edges of the squares contained within the test signal. For purposes of illustration, the contrast has been accentuated in the photograph to emphasize the sharpness enhancement.

Fig. 24 is a conventional test pattern after the signal has been passed through a 2-H comb filter system with horizontal and vertical peaking. Note that the picture edge enhancement is continuous around the circle, indicating sharpness enhancement in all spatial directions. In typical scenes, this capability provides a surprisingly visible improvement in picture clarity.

8. Summary

Superior picture display performance by means of improved signal-processing techniques involving a comb-filter function utilizing CCD technology in a cost-effective IC format has been successfully accomplished. A specific IC device, along with the appropriate external interface functions, has been developed to product level and incorporated in a specific commercial color television receiver. The anticipated beneficial image-performance improvements of reduced dot-crawl and cross-color interference with increased resolution and vertical and horizontal picture sharpness enhancement have been realized.

The circuitry and IC device providing the comb-filter function is referred to commercially as the Dynamic Detail Processor. The primary goal of this program has been accomplished to the level of commercial utilization in the Limited Edition ColorTrak 19" and 25" color TV receiver models announced by RCA in May 1979. These receivers have been described as providing TV pictures that are demonstrably superior, clearer, sharper, and more precise than any other ever made by RCA.

Acknowledgment

This project exemplifies the high order of cooperation that is required between many talented and dedicated individuals in the research, engineering, and manufacturing project phases to bring such an effort to a successful completion in the form of a commercial product. The author would like to especially note the contributions of J. Carnes, D. Sauer, W. Kosonocky, F. Shallcross, and P. Levine in the areas of design, fabrication, and testing of the CCD IC. Commercial realization in the form of a viable color TV receiver product could not have been achieved without the vital contributions and tireless efforts of W. A. Lagoni, J. S. Fuhrer, and G. E. Thornberry along with W. E. Sepp and R. D. Hassell.

To those and all individuals involved, the author would like to express heartfelt appreciation.

References:

- ¹ W. A. Lagoni, D. H. Pritchard, and J. S. Fuhrer, "A Baseband Comb Filter For Consumer Television Receivers," *IEEE Consumer Electronics Fall Conf.*, Chicago, Illinois, 1979.
- ² D. Sauer, "An Integrated CCD Comb Filter for Consumer TV Receivers," *RCA Review*, **41**, p. 29, March 1980.
- ³ "A Theory of Scanning and Its Relation to the Characteristics of the Transmitted Signal in Telephotography and Television," *Bell System Tech. J.*, **15**, p. 464, July 1934.
- ⁴ Heinz E. Kallmann, "Transversal Filters," *Proc. IRE*, p. 302-310, July 1940.
- ⁵ A. C. Schroeder and W. Gibson, "Television Vertical Aperture Correction," *J. SMPTE*, **64**, p. 660, Dec. 1955.
- ⁶ D. H. Pritchard, W. G. Gibson, and A. C. Schroeder, "A High Performance Television Receiver Experiment," *IEEE Trans. Broadcast and TV Receivers*, **BTR-18**, No. 2, May 1972.
- ⁷ D. H. Pritchard, "Electronic Signal Processing Apparatus," US Patent #4,096,516, issued June 20, 1978.
- ⁸ J. Carnes and W. Kosonocky, "Basic Concepts of Charge-Coupled Devices," *RCA Review*, **36**, No. 3, p. 566, Sept. 1975.
- ⁹ S. J. Auty, D. C. Read, and G. D. Roe, "Colour Picture Improvements Using Simple Analogue Comb Filters," *BBC Engineering*, Dec. 1977.
- ¹⁰ G. D. Arndt, F. M. Stuber, and R. J. Panneton, "Video Signal Improvement Using Comb Filter Techniques," *IEEE Trans. Communications*, April 1973.
- ¹¹ Takashi Fujio, "Two-Dimensional Processing of TV Signals," *NHK Technical J.* **135**, Vol. 25, No. 3, 1973.
- ¹² D. H. Pritchard, "NTSC Color Television Fundamentals—A Review," *J. SMPTE*, Nov. 1977.
- ¹³ D. J. Sauer, "CCD Input Circuits," US Patent #4,139,784, Feb. 13, 1979.
- ¹⁴ P. A. Levine, "CCD Comb Filters," US Patent #4,158,209, June 12, 1979.

Design and Performance of a CCD Comb Filter IC

D. J. Sauer

RCA Laboratories, Princeton, NJ 08540

Abstract—This article describes a low-cost CCD comb filter IC for video signal processing in color television receivers. The chip combines a buried-channel CCD 1-H (63.5 μ s) analog delay line with all necessary linear and digital support circuitry using an advanced double-polysilicon N-channel self-aligned gate technology. The design of new circuits is discussed, including a linear variable gain BCCD input structure, automatic CCD input and output biasing, and 10.7 MHz on-chip clock drivers. Typical specifications and measured performance data for the CCD comb filter IC are also presented.

1. Introduction

The CCD comb filter IC described in this article represents the first application of charge-coupled-device technology to video signal processing in a consumer television receiver. Until recently, comb filtering techniques were only used in commercial broadcast television equipment due to the relatively high cost of the required 1-H (63.5 μ s) analog delay lines which utilized glass (acoustic) delay elements. However, RCA has developed an advanced N-channel process that combines high-performance buried-channel CCDs with linear and digital NMOS circuits. This process makes it possible to include all of the support circuits needed to operate a 1-H CCD delay line (such as clock drivers and video amplifiers) on a single low-cost chip that is suitable for consumer electronics.

The comb filter is used in a color TV receiver to separate the luminance (Y) and chrominance (C) video information as well as to provide vertical peaking or aperture correction.¹ The advantages of using a comb

filter are described in a companion article in this issue of RCA Review.² Basically, the use of a comb filter permits increased luminance bandwidth and minimizes luma-chroma interference effects found in conventional NTSC TV receivers. These effects include erroneous colors in picture scenes having luminance information at a spatial frequency near the 3.58 MHz color subcarrier (known as "cross-color" or the "umpire shirt" effect), and luminance "dot crawl" on the edge of color transitions.

2. Basic Comb Filter

The basic comb filter shown in Fig. 1 is a simple transversal filter. The delay line is used to delay the video input signal by 1-H (about 63.5 μ s) which is the period of one horizontal line (f_H is the horizontal line frequency). Since alternate-line luminance signals are in phase, the combed Y output is obtained by adding the video input with a signal that has been delayed by 1-H. This also cancels the chroma components in the Y output because alternate-line chroma signals are 180° out of phase (as explained in Ref. [2]).

The combed C output is obtained in a similar fashion by subtracting the video input from the 1-H delayed signal. The subtraction is accomplished by inverting the video input and then adding. Therefore, in the C output the alternate-line chroma components add in phase, and the luminance components are cancelled in the subtraction process.

The amplitude response for both outputs for an ideal case where the analog delay line has a perfectly flat frequency response and exactly unity gain is also shown in Fig. 1. Note that the combed Y output has periodic peaks in the amplitude response at multiples of f_H (15.734 kHz) whereas the combed C output has corresponding nulls in its response at the same frequencies. In general, the amount of rejection at a given null frequency

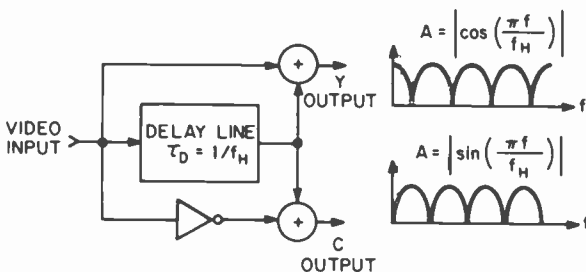


Fig. 1—Basic comb filter circuit and the resulting amplitude response for luminance (Y) and chrominance (C) outputs.

is not infinite, and is measured by a parameter known as the combing magnitude. We define combing magnitude as the ratio in dB of the filter response at a peak frequency to the response at an adjacent null frequency.

The response of a CCD delay line rolls off at higher frequencies because of charge transfer inefficiency.³ This means that a perfect null can only be achieved at one frequency in the pass-band of the comb filter at which the gain in the undelayed and 1-H delayed paths are exactly equal.

To obtain a combing magnitude of 30 dB or better from 0–4 MHz, the frequency response of the delay line must be held within ± 0.5 dB and the 1-H delay time must be accurate within ± 5 ns. This kind of accuracy is difficult to achieve with conventional glass (acoustic) type delay lines because they have to be temperature compensated. The advantage of using a CCD for the delay line is that the time delay (τ_D) is precisely determined by only two factors: (1) the number of CCD stages (N), which is fixed by the layout geometry, and (2) the clock frequency (f_c) which can be synchronized to the 3.58 MHz color subcarrier. The time delay is given by $\tau_D = N/f_c$. Actually, the charge transfer efficiency also affects the time delay slightly. However, this effect is negligible for buried-channel CCDs that have a transfer inefficiency less than 2×10^{-5} . A more general analysis of the response of a comb filter that uses a CCD delay line is presented in Sec. 5.

3. Design of the CCD Comb Filter IC

3.1 General Description

A photomicrograph of the CCD comb filter IC is shown in Fig. 2. The chip size is 3.3×3.1 mm (131×122 mils). The buried-channel CCD 1-H delay line is located in the center of the chip and is surrounded by linear and digital NMOS support circuitry which occupies the major portion of the IC. The NMOS support circuitry includes clock drivers with automatic 50% duty cycle control, a timing generator to operate the variable-gain CCD inputs and the sample-and-hold outputs, an automatic CCD input bias circuit, and linear video amplifiers for the combed luminance and chrominance outputs.

The major features of this IC are as follows:

- Combines buried-channel CCD delay line with analog and digital NMOS circuits.
- Double-poly n-channel self-aligned gate process.
- $682\frac{1}{2}$ -stage 1-H CCD delay line for 10.7 MHz clock frequency.
- $\epsilon \approx 2 \times 10^{-5}$ per transfer.

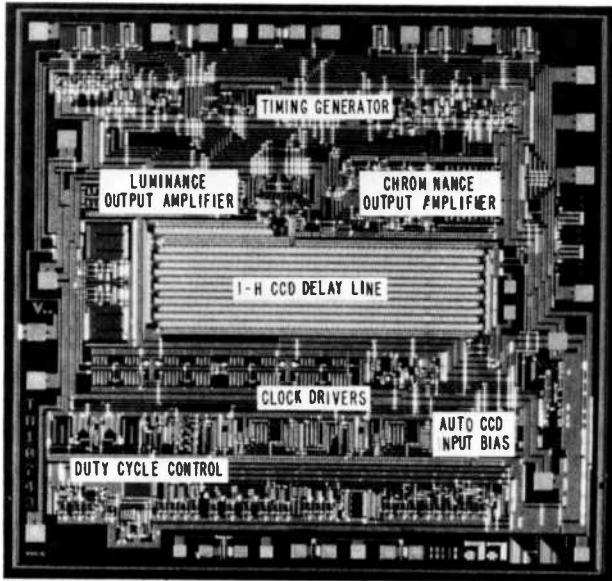


Fig. 2—Photomicrograph of the CCD comb filter IC. Chip size is 3.3 mm X 3.1 mm.

- On-chip clock drivers.
- On-chip timing circuits for charge preset inputs and sample-and-hold outputs.
- Self-adjusting CCD input and output biasing circuits.

Two positive power supplies are required: $V_{cc} = 9\text{ V}$ and $V_{DD} = 16\text{ V}$, as well as a -5 V bias supply for the substrate. The V_{cc} supply is used for the CCD clock driver output section and determines the amplitude of the two-phase clock waveforms. V_{cc} is also used as a reference voltage in some input and output NMOS circuits. The V_{DD} supply is used for the CCD clock driver logic, the timing generator circuits, and the video output amplifiers. The -5 V substrate bias supply is used to (1) increase the parasitic field transistor threshold voltage, (2) reduce junction depletion capacitance to improve circuit speed, and (3) avoid nonlinear threshold characteristics in the video amplifiers due to the NMOS channel doping profile.

The chip is mounted in a standard 22-pin DIP plastic package that has an integral lead-frame heat sink which uses four pins to improve the thermal capability of the package. The maximum operating ambient temperature is 65°C which corresponds to a maximum junction temperature of 95°C .

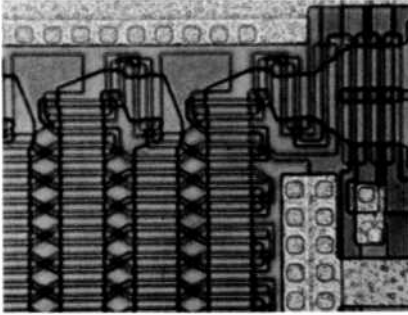


Fig. 3—Photomicrograph of the 180° turn CCD serpentine corner structure.

3.2 Technology

The CCD comb filter IC is fabricated using a double-polysilicon n-channel self-aligned gate process. This process is similar to a double-poly NMOS RAM process, with additional ion-implantation steps to form the buried-channel CCD regions. The CCD delay line is a two-phase serpentine structure with ion-implanted barriers under the second-level polysilicon gates to provide charge directionality when the first-level storage and second-level transfer gates are connected directly together on each clock phase. In the serpentine structure, the direction of charge transfer reverses in alternate channels. This is accomplished by criss-crossing the storage and transfer gates in the intermediate channel-stop regions as shown in Fig. 3. At the ends of the serpentine, a 180° corner turn is accomplished with a gate structure employing two 90° turns in series that operate in a complete charge-transfer mode. This corner structure⁴ maintains a high charge-transfer efficiency compared to alternative floating diffusion corner structures that operate in the so-called bucket-brigade charge transfer mode.⁵ The typical average transfer inefficiency for the CCD delay line is 2×10^{-5} per transfer at the 10.7-MHz clock rate.

The starting material in the process is p-type (100) silicon. Four ion-implantation steps are used during the process in order to control the field threshold and form the buried-channel n-layer. The first ion implantation is a boron field implant which is used in conjunction with a 10,000 Å field oxide to increase the parasitic field transistor threshold beyond 20 V. After the channel regions are defined in the field oxide, a second implantation (phosphorous) is used to adjust the MOS enhancement transistor threshold, and a third implantation (phosphorus) is used to form the buried-channel n-layer. Following the first channel oxidation and first polysilicon gate definition, the fourth implantation

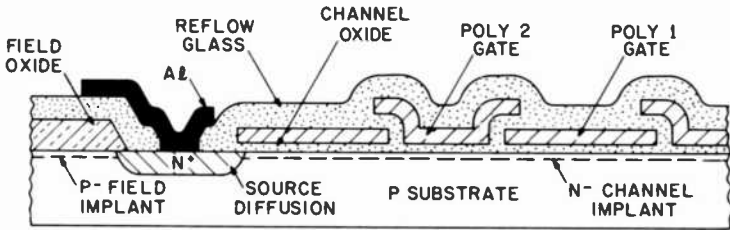


Fig. 4—Cross-sectional view of the double-polysilicon gate n buried-channel CCD.

(boron), which is self-aligned to the first-polysilicon gate edge, is used to form a potential barrier under the second polysilicon level transfer gates. The second polysilicon gates are then defined, and the source and drain regions are formed with a self-aligned N^+ phosphorus diffusion. A phosphorus-doped-glass reflow process is used to improve the step coverage of subsequent aluminum metal lines over the polysilicon gates.

A cross-sectional view of the resulting buried-channel CCD structure is shown in Fig. 4. This process provides both enhancement and deep depletion NMOS transistors which are used in the analog and digital circuits. Typical threshold voltages for these devices are $V_{TE} = 1.5$ V and $V_{TD} = -10$ V, respectively.

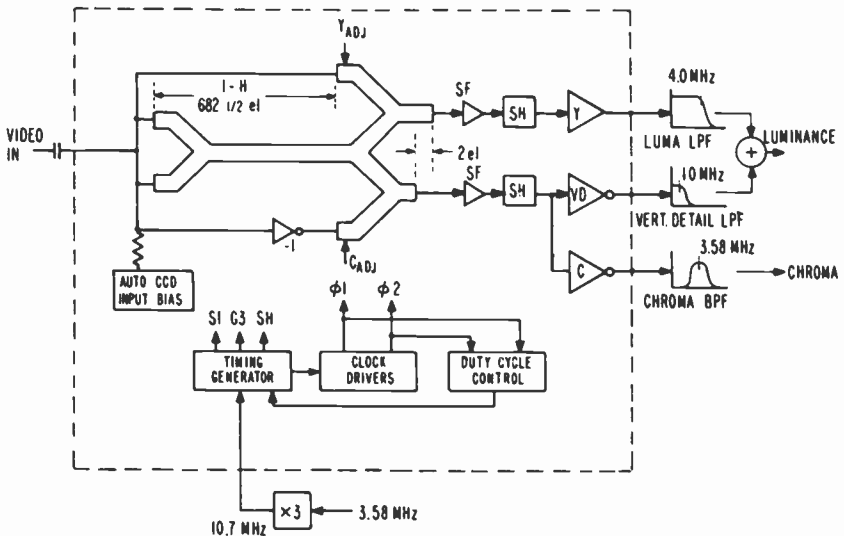


Fig. 5—Block diagram of the CCD comb filter IC.

3.3 CCD Implementation of the Comb Filter

A block diagram of the CCD Comb Filter IC is shown in Fig. 5. The CCD delay line operates at a clock frequency of 10.7 MHz which is exactly 3 times the 3.58 MHz color subcarrier. A single 10.7-MHz reference sine wave input is used to synchronize the timing generator and on-chip clock drivers.

In this design, we have implemented the comb filter function directly in the CCD channel. The signal addition is done by merging two CCD channels together, which essentially makes a perfect adder. The luminance comb is formed by adding signals from a short (1 stage) delay line and a long ($683\frac{1}{2}$ stage) delay line. The difference in delay between the short and long lines is $682\frac{1}{2}$ stages, which is exactly 1-H.⁶ The chroma comb is formed in the same way, except that there is a unity gain inverter at the chroma short-line input.

At the output of the long line, the signal charge is split equally into two channels in order to provide separate 1-H delayed signals for the Y and C adders. Because of this channel split, the signal amplitude in the long line must be twice as large as the signal amplitude in the short lines, so that the long- and short-line signals will have matched amplitudes when they reach the channel summing point. To provide optimum tracking between the long- and short-line input characteristics, two separate inputs followed by channel merging are used for the long-line input. A photomicrograph of the long-line output charge splitter and the signal adding junction is shown in Fig. 6.

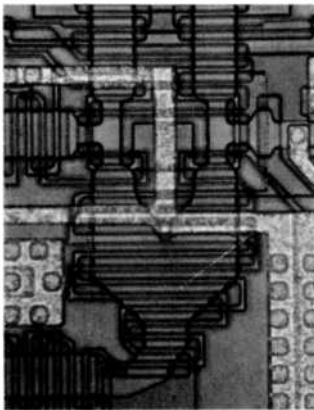


Fig. 6—Photomicrograph of the long-line output charge splitter and signal adding junctions which implement the comb filter function directly in the CCD channel.

In order to achieve the deepest possible null in the filter response, the gain of the two short line inputs may be adjusted with dc control voltages Y_{ADJ} and C_{ADJ} . The operation of these variable-gain inputs is described in Sec. 3.5. Because a half stage of delay is required in the total 1-H delay, the video input for the long line is sampled on ϕ_1 , and the video input for the short line is sampled on ϕ_2 . This means that the duty cycle of the clock waveforms directly affects the 1-H delay time. Therefore, to maintain the advantages of using a CCD for precision delay, the duty cycle is controlled to $50\% \pm 2.5$ ns by a negative feedback circuit. This circuit is described in detail in Sec. 3.4.

As indicated in Fig. 5, the video input is ac coupled. The dc bias on the video input terminal is determined by an automatic CCD input bias circuit which is used to set the bias charge in the CCD registers to an optimum level independent of process variations. The combed luminance and chrominance CCD outputs are buffered on-chip by source followers, sample-and-hold circuits, and video amplifiers. Note that the chroma video amplifier provides two separately buffered outputs, the chroma output signal and the vertical detail signal. The character of these two signals is determined by filtering which is done off the chip since these two outputs are nominally the same at the device pins. The frequency response of the external LC filters used with the CCD comb filter IC is also indicated in Fig. 5. The combed luminance output passes through a 4-MHz low-pass filter to remove 10.7-MHz clock noise. The vertical detail output passes through a 1-MHz low-pass filter and is then added back into the luminance channel. This is done in order to restore vertical detail luminance information and/or provide vertical peaking or aperture correction as explained in Ref. [2]. The combed chroma output passes through a band-pass filter centered at 3.58 MHz before it is fed to the chroma demodulator in the TV receiver. Note that the combed luminance CCD output includes two extra stages of delay relative to the combed chroma CCD output. This extra delay (about 186 ns) is used as a convenient way to match the difference in propagation delay through the external luminance and vertical detail low-pass filters.

3.4 CCD Clock Drivers

The clock drivers are designed to supply two-phase symmetrical clock waveforms to the CCD delay line with an amplitude of 9 V peak-to-peak at 10.7 MHz. For an equivalent load capacitance of 120 pF/phase, the rise and fall times of the driver outputs are about 15 nsec. This section of the IC also contains an integrator and phase comparator as part of an overall negative feedback loop, including the clock drivers, which maintains the duty cycle of outputs ϕ_1 and ϕ_2 at 50%. The total power

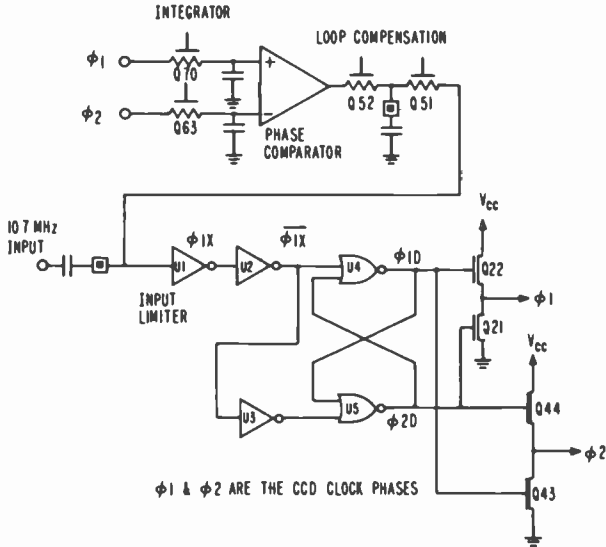


Fig. 7—CCD clock driver logic diagram.

dissipation of the clock driver section is 345 mW at the 10.7-MHz clock frequency.

The logic diagram in Fig. 7 shows how the symmetrical two-phase clock waveforms are generated. A 10.7-MHz reference sine wave is ac coupled to the input limiter where it is amplified to obtain a logic level waveform ϕ_{1X} . The dc level on the input of this limiter relative to its switching

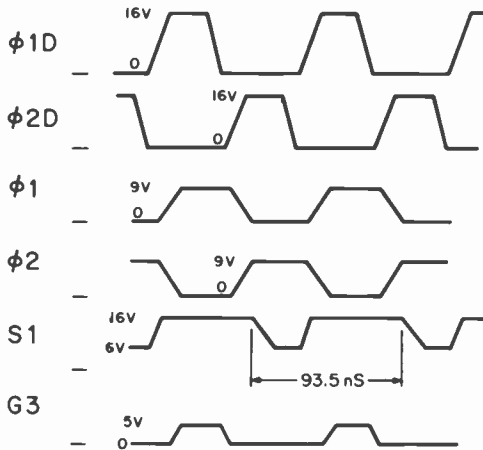


Fig. 8—Timing diagram for the CCD clock drivers.

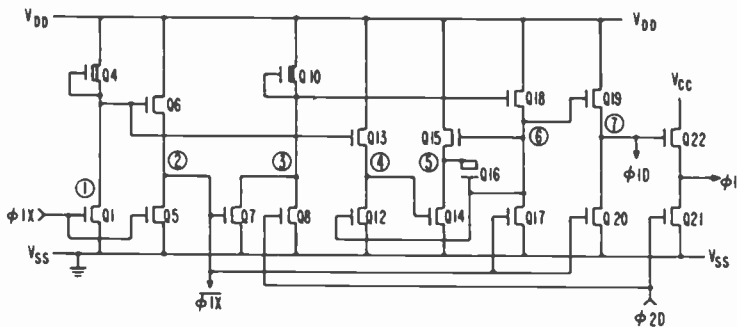


Fig. 9—Detailed schematic diagram for the ϕ_1 section of the clock driver.

threshold determines the clock duty cycle and is set by the duty cycle control feedback circuit.

The input limiter drives a NOR-gate flip-flop which generates two non-overlapping pulses ϕ_{1D} and ϕ_{2D} that swing from 0 to 16 V. These pulses switch the final totem pole output drivers for ϕ_1 and ϕ_2 . The timing of these waveforms is shown in Fig. 8. This diagram also shows two additional pulses, S1 and G3, which are logically derived from ϕ_{1D} , ϕ_{2D} , ϕ_1 , and ϕ_2 and are used to operate the CCD input stage described in Sec. 3.5.

Fig. 9 is a detailed schematic diagram for the ϕ_1 section of the clock driver, showing inverter U2, NOR-gate U4, and the output drivers Q21 and Q22. Inverter U2 is formed by transistors Q1, Q4, Q5, and Q6. Q1 is a grounded source NMOS inverter that uses a depletion current source Q4 for its load device. The maximum load current in Q4 is about 2 mA which provides a very fast rise time (< 10 ns) at node 1. Node 1 is further buffered by a source follower Q6 in order to drive the ϕ_{1x} line capacitance (3 pF) at a slew rate of 1 V/ns.

The simplified NOR gate U4 shown in Fig. 7 actually consists of three circuits: a logical NOR gate (Q7–Q10), a “bootstrap” capacitor drive circuit (Q12–Q18), and a totem pole output stage (Q19–Q20) for ϕ_{1D} . This circuitry is designed to drive the relatively large input gate capacitance of the final clock driver transistors (Q22 and Q43) at very fast slew rates. The logical NOR gate includes two NMOS inverter transistors, Q7 and Q8, and a depletion load device Q10. The “bootstrap” capacitor drive circuit is used to drive node 6 above the V_{DD} supply voltage, so that the ϕ_{1D} pulse will rise all the way to V_{DD} .

In more detail, this circuit operates as follows. When $\overline{\phi_{1x}}$ is high, nodes 3, 6, and ϕ_{1D} are all forced low (by inverters Q7, Q17, and Q20) and node 4 is precharged to $V_{DD} - V_T$ through source follower Q13, which also forces node 5 low by turning ON inverter Q14. When ϕ_{1x} switches low,

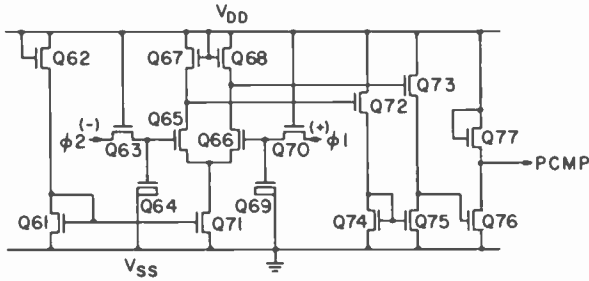


Fig. 10—CCD clock phase comparator schematic diagram. This circuit is used to control the clock duty cycle.

the ϕ_2 section of the clock driver circuit (which is identical to the ϕ_1 section shown in Fig. 9) forces ϕ_{2D} low. Then node 3 switches high and the "bootstrap" MOS capacitor Q16 starts charging up through source follower Q18 and inverter Q14 (which is precharged ON). As node 6 rises it turns ON Q12, and after a 5 ns delay Q12 pulls node 4 low shutting off Q14. This then allows Q15 to pull node 5 up to V_{DD} which forces node 6 above V_{DD} due to the "bootstrap" action of capacitor Q16. When ϕ_{1x} switches high once again, Q17 discharges node 6 to ground and Q20 pulls ϕ_{1D} to ground completing the cycle.

Since ϕ_1 and ϕ_2 are complementary, their duty cycle can be measured by comparing the average dc level of both waveforms using an integrator and differential amplifier as shown in Fig. 7. A more detailed schematic diagram of the clock phase comparator circuit is shown in Fig. 10. The inputs to the comparator, ϕ_1 and ϕ_2 , are integrated by an MOS R - C network and the resultant average dc levels are compared by the differential input pair Q65 and Q66. Since ϕ_2 is the complement of ϕ_1 , the average dc value of these waveforms is only equal when both ϕ_1 and ϕ_2 have a 50% duty cycle. Also the dc value $V_{\phi_1} - V_{\phi_2}$ is a monotonically increasing function of the "ON" duty cycle of ϕ_1 , which is important for

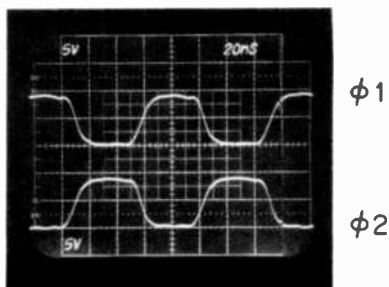


Fig. 11—Measured CCD clock waveforms.

the overall loop stability. The output of the differential stage (Q65-Q68) drives a dc level shifter (Q72-Q75) into the final inverting amplifier stage (Q76, Q77). The overall open loop gain of this system, including the clock driver section, is about 44 dB for a 10.7 MHz input reference level of 2 V peak-to-peak. The stability of the closed loop is insured by using an external frequency compensation capacitor along with an on-chip MOS resistor to provide a dominant breakpoint at 300 Hz.

The measured clock waveforms for the CCD comb filter IC are shown in Fig. 11.

3.5 Input Circuit Techniques

3.5.1 CCD Input Stage

Before discussing the design of the CCD input stage, some basic concepts regarding a buried channel CCD (BCCD) will be reviewed.⁷ Fig. 12 shows

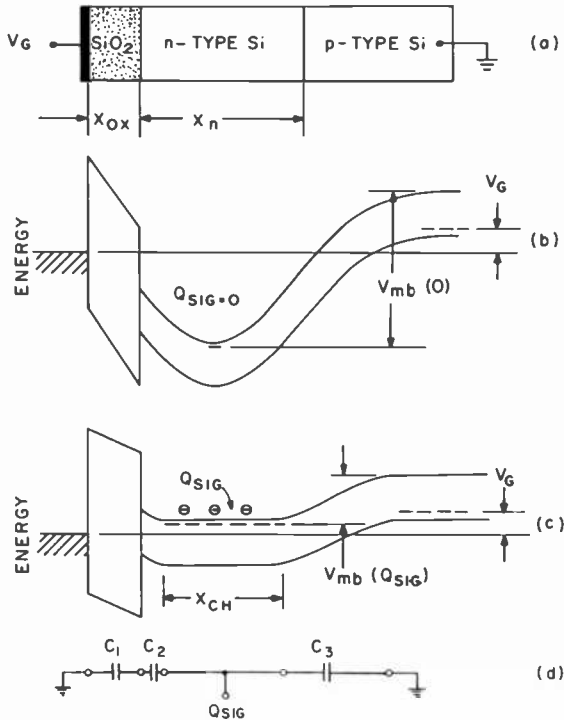


Fig. 12—Buried n-channel CCD device: (a) cross-section showing gate oxide, n-type Si buried layer, and p-type Si substrate; (b) band diagram for the empty well condition (V_{mb} is potential difference between conduction band at the minimum and conduction band in the bulk); (c) band diagram with signal charge Q_{SIG} present; and (d) equivalent circuit for small signals.

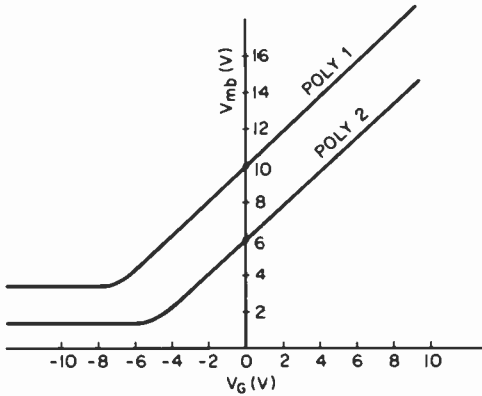


Fig. 13—Empty-well V_{mb} potentials as a function of gate voltage V_g .

a cross-section of a buried n-channel CCD device and the resultant electron energy potential diagram under a single gate when the CCD is operating. If no charge is introduced at the input of the BCCD, all of the mobile electrons in the n-type Si layer are transferred by the action of the CCD clock phases to the output drain which is connected to a positive potential. The fixed positive donor ions which remain in the channel region give rise to a parabolic energy band profile (shown in Fig. 12b) with a minimum energy located about $0.5 \mu\text{m}$ below the SiO_2 -Si interface. The positive donor ion charge to the right of this minimum is imaged by negative fixed acceptor ions in the depletion region which extends into the p-type Si substrate. The positive donor ion charge to the left of the minimum is imaged by negative charge on the CCD gate electrode.

The V_{mb} potential is defined as the channel potential at the minimum with respect to the bulk p-type Si substrate potential. Since electrons that are stored in the CCD channel tend to move toward the minimum electron energy (maximum channel potential), the V_{mb} potentials in a BCCD are useful in predicting the direction of charge flow and storage capacity of a CCD well. In general the V_{mb} potential and position of the energy minimum are functions of the applied gate voltage and charge stored in the CCD well.

The typical empty well V_{mb} potentials for the BCCD used in the comb filter IC are shown in Fig. 13. Note that the V_{mb} potential under the second level polysilicon gate (POLY 2) is about 4 V lower than the V_{mb} potential under the first level polysilicon gate (POLY 1). This is a result of the self-aligned boron barrier implantation described in Sec. 3.2.

Fig. 14 shows a cross-sectional view of the CCD input. The technique used here is a modification of the well-known fill-and-spill method.⁸ This

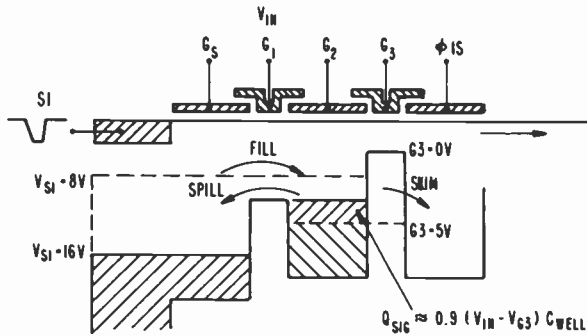


Fig. 14—CCD input stage operation.

modification offers improved linearity in a buried channel CCD as well as a variable-gain capability. In operation, a negative going charge-preset pulse is applied to the source diffusion S1 which fills the well under gate G2 to a level determined by the transfer barrier under the signal gate G1. Next, a "skimming" pulse is applied to G3 which transfer the signal charge Q_{SIG} into the next stage (ϕ_{1S}), leaving behind a large fixed bias charge under G2. This fixed bias charge improves the linearity because the CCD well capacitance ($C_{WELL} = \partial Q / \partial V_{mb}$) is more linear at high charge levels. As shown in Fig. 12c, C_{WELL} is made up from the series combination of C_1 (the oxide capacitance) and C_2 (the surface depletion capacitance) in parallel with C_3 (the bulk depletion capacitance). Therefore, $C_{WELL} = [C_1 C_2 / (C_1 + C_2)] + C_3$. However, C_3 is generally much smaller than C_1 or C_2 so that it can be neglected. Thus, at high charge levels the non-linear depletion capacitance C_2 is large since the charge resides near the SiO_2 -Si interface, and the well capacitance approaches the value of the fixed oxide capacitance C_1 . The gain of this

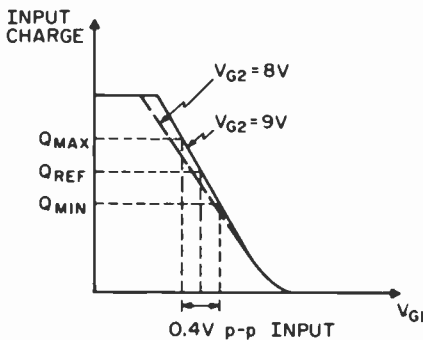


Fig. 15—CCD input stage transfer function.

input stage can be adjusted slightly ($\pm 10\%$) by varying the dc voltage applied to G2 which changes the value of C_{WELL} by modulating the surface depletion capacitance C_2 . This variable gain feature is used in adjusting the gain of the short CCD line inputs via a dc control voltage (Y_{ADJ} or C_{ADJ}) in order to match the long line CCD input stage gain to obtain maximum combing magnitude.⁹

The CCD input stage transfer function is plotted in Fig. 15. The maximum video input level is 0.4 V p-p, which modulates the input charge level from Q_{MIN} to Q_{MAX} . The bias charge level Q_{REF} , which is transferred down the 1-H delay line when there is no video input signal modulation, is maintained at about 50% of a full well in the 1-H delay line by an automatic input bias circuit described in Sec. 3.5.2. Fig. 15 illustrates the effect on the input transconductance obtained by changing the dc voltage on G2 from 9 to 8 V.

3.5.2 Automatic Input Bias Circuit

The automatic input bias circuit shown in Fig. 16 utilizes two charge reference registers, A and B, in conjunction with a negative feedback amplifier to set the input bias charge in the CCD signal register to 50% of a full well level independent of device parameter variations.¹⁰ The 50%

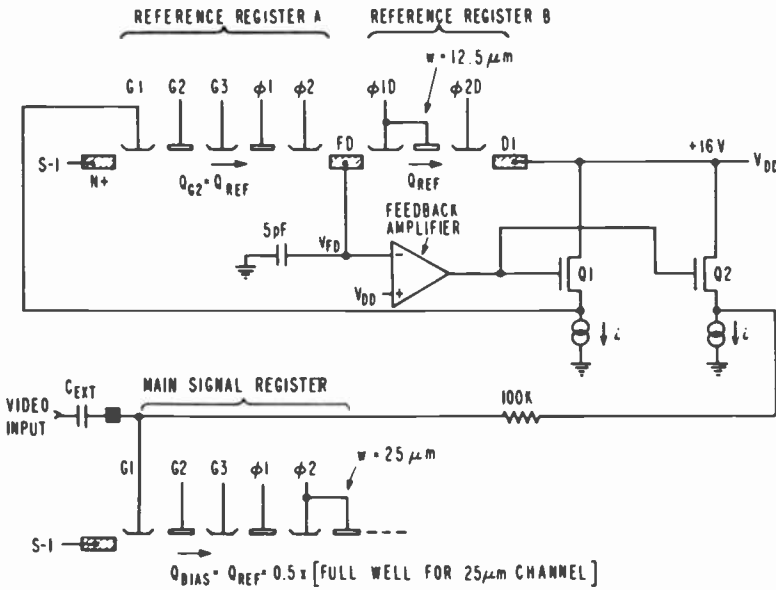


Fig. 16—Automatic input bias circuit used to set the bias charge level in the 1-H delay line.

level was chosen to maximize the dynamic range of the signal charge in the 1-H delay line. Register A is identical to the main signal register, except that its input gate G1 is connected to a reference voltage coming from the source follower Q1. The zero signal dc voltage on the signal register gate G1 is also equal to this reference voltage because the source follower Q2 matches Q1. Therefore, the bias charge Q_{BIAS} in the main signal register is equal to the charge in Register A.

The charge in Register A is transferred to a floating diffusion (FD) which is connected to an integrating capacitor (5 pF) and the inverting input of the feedback amplifier. Register B removes a fixed amount of reference charge (Q_{REF}) from the floating diffusion during each clock cycle. This is done by the gate pair connected to ϕ_{ID} which scoops out a full well of charge using a fill-and-spill technique. However, since Register B is only half as wide as the main signal register, Q_{REF} is 50% of a full well in the signal register. The negative feedback in this circuit

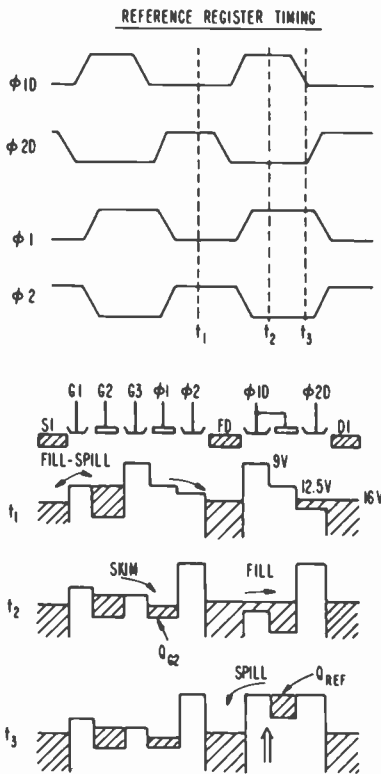


Fig. 17—CCD reference register timing diagram and V_{mb} potentials during operation.

forces the charge in Register A to be exactly equal to the reference charge in Register B. Therefore, the bias charge in the signal register is maintained at 50% of a full well since it tracks the charge level in Register A.

The operation of reference registers A and B is further illustrated in Fig. 17 which shows the channel V_{mb} potentials at various times during the clock cycle. During t_1 , the charge on Register A (Q_{RA}) is transferred to the floating diffusion, and the charge Q_{REF} in Register B is removed to the drain D1. During t_2 , a new charge Q_{RA} is generated in Register A under ϕ_1 by a "skim" pulse applied to G3. Also, in Register B, the well under the ϕ_{1D} storage gate is filled by charge from the floating diffusion (i.e., the floating diffusion acts as a *source* for Register B and a *drain* for Register A). At time t_3 , the excess charge under ϕ_{1D} spills back into the floating diffusion leaving a full well of charge Q_{REF} under ϕ_{1D} .

3.6 Output Circuit Techniques

The outputs from the CCD are buffered using sample-and-hold circuitry and linear NMOS amplifiers. This is done to reduce the 10.7-MHz clock noise and provide a low (300 ohm) output impedance capable of driving external L - C filters.

The luminance output amplifier shown in Fig. 18 senses charge with a standard floating diffusion (FD) that is reset to V_{DD} by the ϕ_{1D} timing pulse. The capacitance at the floating diffusion was reduced to about 80 femtofarads by using two source followers. These source followers also shift the dc level of the signal from V_{DD} to about 4 V which is compatible with the following video amplifiers. The signal voltage developed on the floating diffusion is about 0.5 V p-p for a 0.4 V p-p video input level.

The sample-and-hold circuit reduces the clock noise to prevent the following video amplifiers from saturating. The sampling pulse (SH) is generated from the clock waveforms using logic gates and has a 25-ns

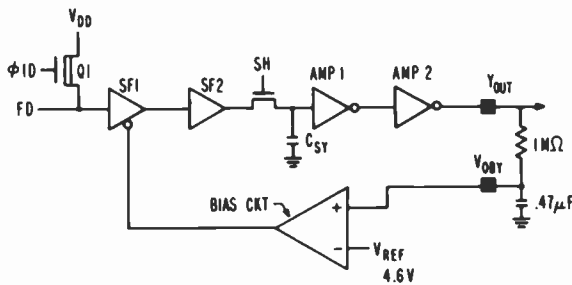


Fig. 18—Luminance output amplifier block diagram.

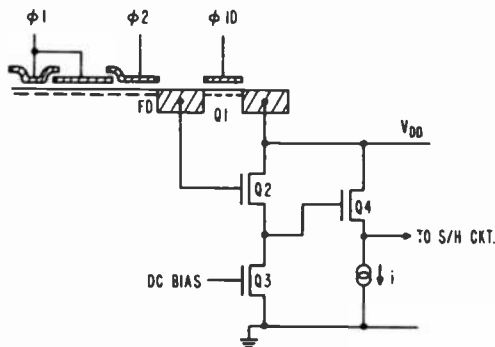


Fig. 19—CCD output stage showing low-capacitance floating diffusion and dual-source-follower.

pulse width. It is timed to occur immediately after the signal charge is transferred to the floating diffusion from the last stage in the CCD register. The inverting video amplifiers that follow the sample-and-hold circuit provide a voltage gain of 12.8 dB. However, since each source follower has a loss of about 1.4 dB, the overall gain of the amplifier from FD to Y_{OUT} is 10 dB.

The dc biasing for this amplifier is set by a feedback circuit that compares the dc output level at Y_{OUT} with an internal 4.6 V reference derived from V_{cc} .

The CCD output stage source followers are shown in more detail in Fig. 19. The source follower Q2 was designed for minimum input gate capacitance in order to obtain the maximum possible signal voltage swing on the floating diffusion. Q3 is used as an adjustable current source load for Q2 so that the dc level at the output of the second source follower Q4 is determined by the bias voltage Y_{OBG} which comes from the bias circuit shown in Fig. 18.

Fig. 20 is a schematic of the first video amplifier (AMP 1) following

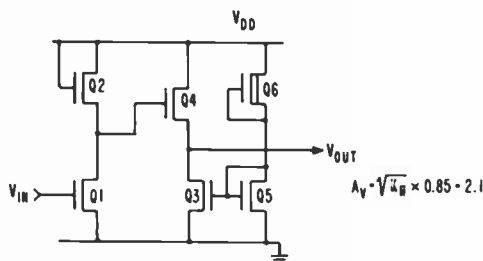


Fig. 20—Video amplifier schematic diagram.

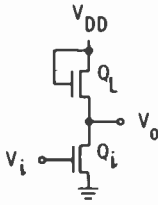


Fig. 21—Circuit of linear NMOS inverter.

the sample-and-hold circuit in the luminance output amplifier. The voltage gain of this circuit is 6.4 dB, the bandwidth is 30 MHz, and the total harmonic distortion is better than -50 dB at 2 MHz. Transistors Q1 and Q2 form a linear inverting amplifier which has a gain $A_v = -\sqrt{K_R}$ where K_R is the K ratio of the inverter Q1 to the load Q2. A derivation for the gain in this inverter when both Q1 and Q2 are operating in their saturation region is as follows (see Fig. 21). For Q_i ,

$$I_{DS} = K' \frac{W_i}{L_i} (V_i - V_T)^2. \tag{1}$$

For Q_L ,

$$I_{DS} = K' \frac{W_L}{L_L} (V_{DD} - V_o - V_T)^2. \tag{2}$$

where W_i , W_L are the widths of the inverter and load transistors and L_i , L_L are their lengths. Equating Eqs. [1] and [2],

$$V_o = -\sqrt{K_R} (V_i - V_T) + V_{DD} - V_T \tag{3}$$

where

$$K_R = \frac{W_i/L_i}{W_L/L_L}.$$

By differentiating Eq. (3),

$$A_v = \frac{\partial V_o}{\partial V_i} = -\sqrt{K_R}.$$

The K_R of 6 used in this design results in an inverter voltage gain of $A_v = \sqrt{6}$ or 7.8 dB. The output of the inverter is buffered with a source follower, Q4, which has a constant current source load Q3. This circuit is designed for maximum linearity when $V_{OUT} = V_{IN}$, so that similar video amplifiers can be dc coupled.

4. Performance of the CCD Comb Filter IC

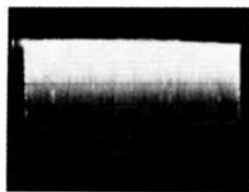
Typical specifications for the CCD comb filter IC are as follows:

- Power supplies: 9 V, 16 V, -5 V (650 mW total)
- Standard 22-pin DIP plastic package
- Video input: 0.4 V_{p-p}, $R_{IN} = 100$ kilohms
- Video output: 1.5 V_{p-p}, $R_0 = 300$ ohms
- Frequency response: -2.5 dB at 3.58 MHz
- Linearity: -40 dB THD
- Dynamic range: 65 dB
- Combing magnitude: >30 dB, 0-4 MHz

The standard video input level is 0.4 V p-p into an input impedance of 100 kilohms. At the peaks in the comb response, the overall gain to the luminance output is 11.5 dB and to the chrominance output is 16 dB. These outputs have a typical output impedance of 300 ohms which is designed to drive external LC filters.

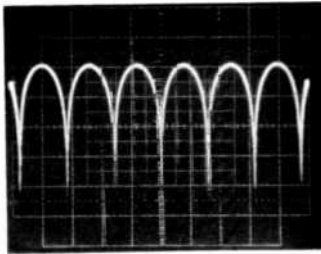
The luminance output frequency response from 0-5 MHz measured with a network analyzer is illustrated in Fig. 22. Although the individual comb nulls can not be seen at this scale, the lower envelope in the curves indicates the response at the null frequencies. Therefore, the combing magnitude at any frequency is calculated by the difference in dB of the upper envelope (comb peaks) and the lower envelope (comb nulls). An expanded view of the luminance and chrominance output frequency response around 3.58 MHz is shown in Fig. 23. The measured combing magnitude at this point is about 40 dB. Note that the nulls in the luminance output response occur at the peaks in the chrominance output response and vice versa.

The frequency response (measured at the peaks in the comb) for both the luminance and chrominance outputs is down 2.5 dB at 3.58 MHz. Of this 2.5 dB roll-off, 1.6 dB is due to the $\sin(\pi f/f_c)/(\pi f/f_c)$ response

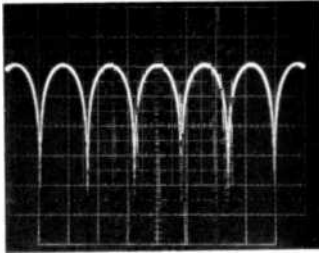


Vert: 10 dB / div.
Hor: 0 - 5 MHz

Fig. 22—Luminance output frequency response from 0-5 MHz.



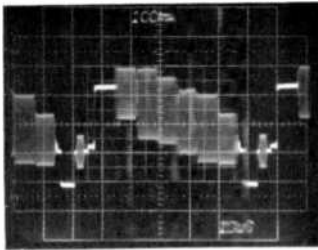
LUMINANCE OUTPUT COMB
(EXPANDED SCALE)
VERT: 10 dB/DIV
HORIZ: 10 kHz/DIV
CENTER FREQ.: 3.58 MHz



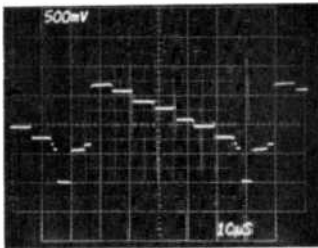
CHROMA OUTPUT COMB
(EXPANDED SCALE)
VERT: 10 dB/DIV
HORIZ: 10 kHz/DIV
CENTER FREQ.: 3.58 MHz

Fig. 23—Luminance and chrominance output frequency response near 3.58 MHz.

of the sample-and-hold circuitry in the output amplifiers which has its first zero at the clock frequency. The remaining 0.9 dB loss is due to charge transfer inefficiency in the CCD delay line and roll-off in the video amplifiers.

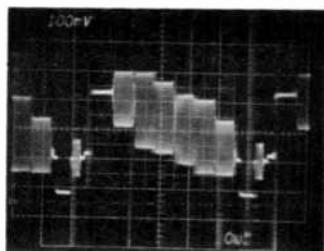


VIDEO INPUT:
NTSC COLOR BAR
TEST PATTERN

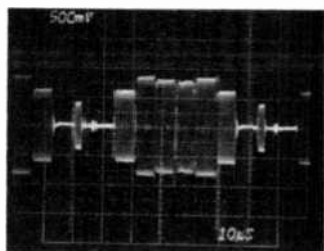


COMBED LUMINANCE
OUTPUT AFTER LPF

Fig. 24—Luminance output signal for a standard NTSC color bar input.

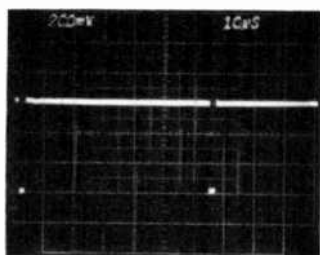


VIDEO INPUT:
NTSC COLOR BAR
TEST PATTERN

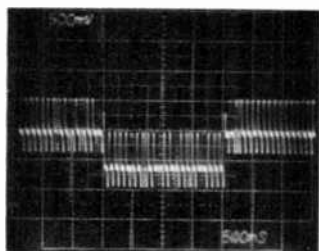


COMBED CHROMA
OUTPUT AFTER LPF

Fig. 25—Chrominance output signal for a standard NTSC color bar input.



(a)



(b)

Fig. 26—Luminance output pulse response for a single $0.2-V_{p-p}$ $2-\mu s$ input pulse (a) after a LPF to remove clock noise and (b) expanded view of 1-H delayed pulse before the LPF.

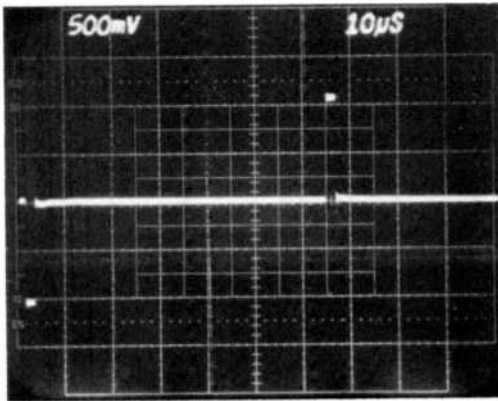


Fig. 27—Chrominance output pulse response for single $0.2\text{-}V_{p-p}$ $2\text{-}\mu\text{s}$ input pulse.

The luminance output signal for a standard NTSC color bar input test signal is shown in Fig. 24. Here, the luminance output is shown following a 4.0 MHz low-pass filter which removes the residual 10.7 MHz clock components. Note that the combing process has removed the 3.58 MHz chroma components, leaving only the sync pulse and luminance staircase. The corresponding chrominance output signal for the same NTSC color bar input is shown in Fig. 25. Here, the combing has removed the sync pulse and luminance staircase leaving only the 3.58 MHz chroma components.

The pulse response for the luminance and chrominance outputs are illustrated in Figs. 26 and 27, respectively. For these tests, the video input signal is a single 0.2-V p-p $2\text{-}\mu\text{s}$ pulse. The luminance output response to such a pulse, shown in Fig. 26(a), consists of two similar pulses that

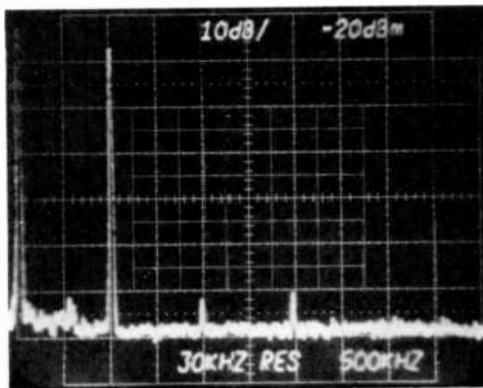


Fig. 28—Luminance output spectrum for a 1-MHz $0.4\text{-}V_{p-p}$ input sine wave.

are spaced apart by exactly 1-H (63.555 μ s). The first pulse is the result of the input pulse delayed through the short (1-stage) CCD delay line, and the second pulse is the result of the input pulse delayed through the long (683.5-stage) CCD delay line. An expanded view of the 1-H delayed pulse at the luminance output pin (before the external 4.0 MHz low-pass filter removes the 10.7 MHz clock components) is shown in Fig. 26(b).

The chrominance output pulse response is shown in Fig. 27. In this case the two output pulses are opposite in polarity because of the unity gain inverter which is located at the chroma short line input (see Fig. 5).

The CCD comb filter IC exhibits a total harmonic distortion of about -40 dB, and a dynamic range of 65 dB (measured as the peak signal to rms noise for a 4 MHz bandwidth). The linearity of this device is illustrated in Fig. 28 which shows a spectrum analysis of the luminance output for a 1 MHz 0.4 V p-p input sine wave.

5. Analysis of the Comb Filter Response

The effect of charge transfer inefficiency on the response of the comb filter for a sine wave input signal is considered in this section. The definitions listed below will be used in the discussion which follows:

$A_c(\omega)$ = chrominance output amplitude response

$A_y(\omega)$ = luminance output amplitude response

ϵ = charge transfer inefficiency per transfer

f = input signal frequency

f_c = clock frequency

f_H = $1/\tau_D$ = horizontal line frequency

n = number of charge transfers

N = number of CCD stages

$R(\omega)$ = CCD delay line amplitude response

T_c = $1/f_c$ = clock period

$\tau_D(\omega)$ = net CCD delay time

ω = $2\pi f$ = input signal angular frequency

In a CCD that is used to delay analog signals, the charge transfer inefficiency ϵ causes two effects: (1) amplitude response roll-off and (2) an additional time delay $\Delta\tau_D$.³ The amplitude response for the CCD delay line is given by

$$R(\omega) = \exp[-n\epsilon(1 - \cos\omega T_c)]. \quad [4]$$

The phase shift $\Delta\phi$ due to the additional time delay $\Delta\tau_D$ is given by

$$\Delta\phi = \omega\Delta\tau_D = n\epsilon \sin\omega T_c. \quad [5]$$

The total delay time for the CCD delay line is

$$\tau_D(\omega) = \frac{N}{f_c} + \Delta\tau_D = \frac{N}{f_c} + \frac{n\epsilon}{\omega} \sin\omega T_c \tag{6}$$

As we discussed in Sec. 2, the amplitude response roll-off at higher frequencies due to ϵ means that a perfect null can only be achieved at one frequency in the pass-band of the comb filter where the gains in the undelayed and 1-H delayed paths are exactly equal. Also, because of the additional time delay, $\Delta\tau_D$, the null frequencies where maximum rejection is obtained are slightly lower than the desired null frequencies, because they are spaced at frequency intervals of $f'_H = (\tau_D + \Delta\tau_D)^{-1}$ instead of the intervals of $f_H = \tau_D^{-1}$. Both of these effects tend to degrade the comb filter performance, so it is important to minimize the charge transfer inefficiency.

5.1 Comb Filter Transfer Functions

Fig. 29 is a generalized block diagram showing how the luminance and chrominance outputs are obtained. The transfer function $Y(j\omega)$ for the luminance output, shown in Fig. 29(a), is

$$Y(j\omega) = 1 + R(\omega)e^{-j\omega\tau_D(\omega)}. \tag{7}$$

The magnitude and phase for the luminance transfer function are

$$|Y(j\omega)| = [1 + R^2(\omega) + 2R(\omega) \cos\omega\tau_D(\omega)]^{1/2} \tag{8}$$

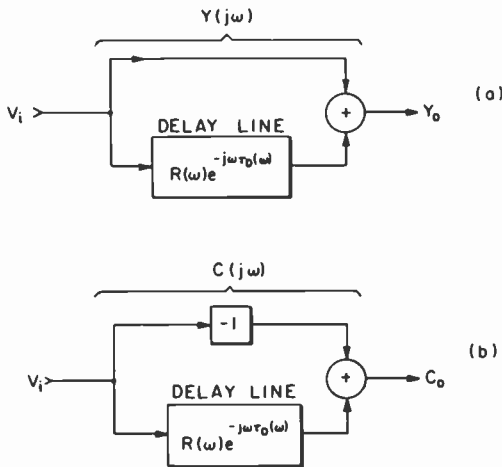


Fig. 29—Block diagram showing transfer functions (a) for the combed luminance output and (b) for the chrominance output.

$$\phi_y = \arctan \left[\frac{-R(\omega) \sin \omega \tau_D(\omega)}{1 + R(\omega) \cos \omega \tau_D(\omega)} \right]. \quad [9]$$

For the ideal case where $\epsilon = 0$ and $R(\omega) = 1$, the normalized luminance amplitude response is

$$A_y(\omega) \equiv \frac{|Y(j\omega)|}{2} = \frac{1}{\sqrt{2}} (1 + \cos \omega \tau_D)^{1/2}. \quad [10]$$

Using the identity $\cos \theta = 1 - 2\sin^2(\theta/2)$, $A_y(\omega)$ may also be expressed in the alternative forms:

$$A_y(\omega) = \left| \cos \frac{\omega \tau_D}{2} \right| = \left| \cos \frac{\pi f}{f_H} \right|. \quad [11]$$

The transfer function $C(j\omega)$ for the chrominance output, shown in Fig. 29(b) is

$$C(j\omega) = -1 + R(\omega)e^{-j\omega \tau_D(\omega)}. \quad [12]$$

The magnitude and phase for the chrominance transfer function are

$$|C(j\omega)| = [1 + R^2(\omega) - 2R(\omega) \cos \omega \tau_D(\omega)]^{1/2} \quad [13]$$

$$\phi_c = \arctan \left[\frac{R(\omega) \sin \omega \tau_D(\omega)}{1 - R(\omega) \cos \omega \tau_D(\omega)} \right]. \quad [14]$$

For the ideal case where $\epsilon = 0$ and $R(\omega) = 1$, the normalized chrominance amplitude response is

$$A_c(\omega) \equiv \frac{|C(j\omega)|}{2} = \frac{1}{\sqrt{2}} (1 - \cos \omega \tau_D)^{1/2} \quad [15]$$

This may also be expressed as

$$A_c(\omega) = \left| \sin \frac{\omega \tau_D}{2} \right| = \left| \sin \frac{\pi f}{f_H} \right|. \quad [16]$$

5.2 Sensitivity Analysis for Variations in $\omega \tau_D$ Near Comb Null Frequencies

As indicated by the comb filter output amplitude responses plotted in Fig. 1, the maximum slopes in the amplitude response occur at the null frequencies. At these frequencies, the slope is

$$\frac{\partial A}{\partial(\omega \tau_D)} = \pm \frac{1}{2} \quad [17]$$

Eq. [17] may be derived by differentiating Eq. [10] or Eq. [15] with respect to $\omega\tau_D$. The change ΔA in the amplitude response at the null frequencies due to a change $\Delta(\omega\tau_D)$ is

$$\Delta A = \frac{\partial A}{\partial(\omega\tau_D)} \Delta(\omega\tau_D) = \pm \frac{1}{2} (\omega\Delta\tau_D + \tau_D\Delta\omega). \quad [18]$$

For example, the effect of a 5-ns error in the delay time τ_D on the combing magnitude at a desired null frequency near 3.58 MHz may be estimated by using Eq. [18] with $\omega = 2\pi \times 3.58$ MHz, $\Delta\omega = 0$, and $\Delta\tau_D = 5$ ns. This results in a $\Delta A = 5.6 \times 10^{-2}$, or a combing magnitude of $20 \log (\Delta A)^{-1} = 25$ dB.

6. Conclusions

A self-contained CCD comb filter IC has been developed for use in NTSC color TV receivers that separates the luminance and chrominance information much more effectively than the conventional filtering techniques previously used. All of the support circuitry needed to operate the CCD delay line, including the clock drivers and video amplifiers, has been integrated on the chip. The operation of the CCD is self-adjusting using feedback controls so that the only external adjustments are for the comb null depths.

The relatively low cost of this comb filter makes it suitable for consumer electronics, and, in fact, it is presently in production in the Limited Edition series of 1980 RCA ColorTrak TV receivers.

Acknowledgments

The CCD comb filter IC described in this article is the culmination of over five years of research and development at RCA Laboratories. During this period many people have made outstanding contributions to the success of this project. The author especially wishes to acknowledge the contributions of W. F. Kosonocky and F. V. Shallcross for CCD process development, R. Miller and L. Bijaczyk for device fabrication, J. E. Carnes for CCD designs, P. A. Levine and J. V. Groppe for innovative CCD testing and characterization, S. N. Shen and R. H. Dawson for circuit simulation and reliability studies, G. M. Meray and D. Allesandrini for layout and digitizing, and D. H. Pritchard for the system design.

References:

- ¹ W. A. Lagoni, D. H. Pritchard, and J. S. Fuhrer, "A Base-band Comb Filter for Consumer Television Receivers," Chicago Fall Conference on Consumer Electronics, Nov. 13, 1979.
- ² D. H. Pritchard, "A CCD Comb Filter for Color TV Receiver Picture Enhancement," *RCA Review*, **41**, p. 3, March 1980 (this issue).
- ³ C. H. Sequin, M. F. Tompsett, *Charge Transfer Devices*, pp. 70-76, Academic Press, New York, 1975.
- ⁴ M. G. Kovac, "CCD Electrode and Channel Structure for 180° Turn," U.S. Patent 4,160,262, July 3, 1979.
- ⁵ See Ref. [3], pp. 15-18 and 91-97.
- ⁶ D. H. Pritchard, "Electronic Signal Processing Apparatus," U.S. Patent 4,096,516, June 20, 1978.
- ⁷ W. F. Kosonocky, J. E. Carnes, "Basic Concepts of Charge-Coupled Devices," *RCA Review*, **36**, No. 3, p. 572, Sept. 1975.
- ⁸ W. F. Kosonocky, "Introducing Signal At Low Noise Level to Charge-Coupled Circuit," U.S. Patent 3,986,198, Feb. 10, 1976.
- ⁹ P. A. Levine, "CCD Comb Filters," U.S. Patent 4,158,209, June 12, 1979.
- ¹⁰ D. J. Sauer, "CCD Input Circuits," U.S. Patent 4,139,784, Feb. 13, 1979.

Introduction to Luminescent Glasses

Tatsuo Takahashi

RCA Research Laboratories, Inc., Machida City, Tokyo, Japan

The following papers in this issue of the RCA Review discuss luminescent glasses of complex metaphosphate composition whose constituents include alkali metals, alkaline earth metals, yttrium, and/or rare earths. They describe studies carried out at the RCA Research Laboratories in Machida, Japan.

Unlike the crystalline luminescent materials, which appear ubiquitously in our daily life as phosphors in fluorescent lamps and TV kinescope tubes, luminescent glasses and their uses are not commonly known. A brief overview is necessary, therefore, to place these papers in perspective. Moreover, it is desirable to explain why luminescent glasses should be studied in view of a prevailing belief that their luminescent performance is much inferior to that of crystalline solids such as phosphors.

I will first present a brief description of glass and its constituents, followed by a brief history of studies of luminescent glass and discussion of various applications. Finally, a brief introduction to the papers on luminescent metaphosphate glasses that follow is given. With respect to the history on luminescent glasses, the reader is cautioned that coverage is far from complete, being mostly limited to works that serve to show the general trend of luminescent glass research at this time. More detailed discussions can be found in the excellent review articles referred to in the bibliography.

A definition for glass in the *ASTM Standards for Glass* states, "Glass is an inorganic product of fusion which has been cooled to a rigid condition without crystallization". This definition is accepted by most glass technologists, but there are some scientists¹ who also include glassy materials prepared by techniques that do not require cooling from the liquid state, such as those deposited from vapor or liquid solutions or glass prepared by chemical reactions. The ASTM definition seems more convenient, however, since it distinguishes glass from other noncryst-

talline materials prepared by vacuum evaporation, sputtering, and chemical vapor deposition, i.e., those non-crystalline materials often referred to by physicists and electronic engineers as amorphous materials. In this paper, the ASTM definition is implied whenever the word "glass" is used.

The structure of glass consists of a continuous random network of glass-forming oxides in which long range order is missing. The reason why certain oxides form glass was first proposed by Zachariasen² and, later, Sun classified various oxides in terms of bonding strength.³ Glass forming oxides such as SiO_2 , GeO_2 , B_2O_3 , and P_2O_5 have the strongest bonding strength among oxides. Such oxides are called "glass network formers". There are also nonoxidic glass formers^{4,5} such as As_2S_3 and BeF_2 . Oxides with small bonding strength, such as oxides of alkali, alkaline earth, and rare earths cannot form a glass network and are called "modifiers" or "network modifiers". Oxides having an intermediate bonding strength, such as Al_2O_3 , TiO_2 , ZrO_2 , ZnO , and CdO can form a glass network under certain circumstances. For example, most of these oxides can be made into glass by the "splat" cooling technique. These oxides are called "intermediates". Some fluorides, such as AlF_3 and ZrF_4 , are also intermediates.⁶

Weyl classified luminescent glasses into three groups according to the role of the glass phase in producing the fluorescence:⁷

- (1) Glasses containing crystalline fluorescence centers,
- (2) Glasses containing energy isolated atoms or molecules, and
- (3) Glasses containing fluorescent ions.

Weyl thoroughly reviewed work done up to 1950 on the luminescent glasses of each category. The luminescent glasses of Class (1) include those containing manganese-activated Zn_2SiO_4 ,⁸ manganese-activated metallic sulfide, and selenide crystallites.⁹ More recently, reports have been published on the preparation of glasses containing manganese-activated μ -cordierite, $2\text{MgO}\cdot 2\text{Al}_2\text{O}_3\cdot 5\text{SiO}_2$ crystalline phosphors.¹⁰

Examples of luminescent glasses of Class (2) are silver- and CdS -containing glasses.⁷ In the former, the neutral silver atoms, prepared by reducing the silver ion contained in silicate glass, produce fluorescence of a yellowish white color. The cadmium sulfide glass can be prepared by heat treatment of CdS -containing silicate glass. The fluorescence from CdS is observed only when the aggregates of CdS do not reach the size of crystals. The luminescent glasses of Classes (1) and (2) are inherently unstable and seem to have limited practical importance.

In luminescent glasses of Class (3), fluorescence originates from one of the glass-forming constituents. These glasses contain no crystalline phase and so are truly glassy phosphors. The remainder of this introduction and the papers that follow deal only with luminescent glasses of this class.

In the early 1940's, numerous luminescent glasses were developed for use in photoluminescent devices, for example, for the envelopes of gas discharge lamps filled with rare gas or mercury vapor. Various glass compositions were reported for this purpose, such as Tl-activated silicates,^{11,12} Mn-Ce coactivated phosphates,¹³ Mn, Ag, Tl, Sn, or Pb-activated alkali and alkaline earth metaborates, and metaphosphates.^{14,15} Weyl discussed the glasses activated with U, V, and rare earths in the 1940's.⁷ However, no practical application of these luminescent glasses in fluorescent lamps was reported, probably because the fluorescence intensity and efficiency of these glassy phosphors was impracticably lower than those of crystalline phosphors. Work on luminescent glasses up to 1964 was reviewed by Rindone.¹⁶ Relatively small progress appears to have been made during the decade 1950 to 1960.

The low efficiency of these early glassy phosphors is not unexpected. Glass is highly insulative, and fluorescent ions, i.e. activators, are located in nonequivalent sites of lower symmetry than in crystalline solids due to the lack of long range order in the glass. Hence, the effective energy transfer of absorbed photons from the glassy host to the activator centers cannot be expected. To improve the efficiency of glassy phosphors one has to advantageously utilize the intrinsic nature of the glassy matrix. This might be accomplished (1) by increasing the activator concentration and (2) by choosing an activator that is not sensitive to the surroundings and has less self-concentration quenching tendency. Higher activator concentration is possible because glasses are good solvents of metallic ions, which ensures increased direct absorption of exciting photons by the activator itself. Self-concentration quenching is the phenomenon whereby luminescence intensity decreases with increasing activator concentration. The activators that satisfy condition (2) are the rare earths. Although the fluorescence of rare earths in glass was first observed in the 1880's,⁷ its importance was not fully recognized until the laser was discovered in 1960.¹⁷ Successful glass laser operation was first reported in 1961.¹⁸

Optical transitions typical of rare-earth ions are due to transitions in the inner shielded $4f$ shell. For this reason the fluorescence of rare-earth ions is influenced to a much smaller degree by the surrounding crystalline field than is the fluorescence of other activators having transitions in outer electron shells. Therefore, the fluorescence of rare-earth ions in glass is expected to be quite similar to that in crystals. Indeed, extensive investigations were made by Reisfeld and her group¹⁹ of absorption, fluorescence, and energy transfer in rare earths in various inorganic glasses, such as silicate, germanate, borate, and phosphates. A remarkable similarity was found to phenomena in crystals. The principal difference between the fluorescence of rare earths in glasses and that in

crystals is the inhomogeneous broadening due to the presence of multiple activator sites having a slightly different symmetry.

From a practical standpoint, the discovery of lasing phenomenon in barium crown glass¹⁸ gave a strong thrust to the development of improved rare-earth-activated luminescent glass. For the first time in the history of luminescent glass research, systematic investigations were carried out on the fluorescence of rare earths in glasses, particularly that of Nd, the best of the lasing rare earths, which include Yb, Ho, Er and Tm. In the early 1960's, most laser glasses were Nd-activated silicate glasses. The compositions and properties of these silicate laser glasses have been reviewed by Young²⁰ and Snitzer.²¹ Hirayama and Lewis²² investigated the Nd³⁺ fluorescent decay time in alkali silicate glasses and found that it increased with increasing ionic radius of the alkali metal modifier in the glass. Harper²³ measured the absorption, fluorescence, fluorescent decay time, and quantum efficiency of various glasses doped with different amounts of Nd³⁺ and discussed the results in terms of laser operation. Young²⁰ cited the following characteristics to distinguish laser glasses from crystalline laser materials:

- (1) The properties of glass are isotropic.
- (2) Glass can be doped uniformly at high concentrations.
- (3) Glass has considerable flexibility as to shape and size.
- (4) Glass has flexibility in its physical constants, such as refractive index, hardness, and thermal expansion, by virtue of good solubility for the various constituents.
- (5) Production cost is relatively low.
- (6) Various techniques, such as drilling, drawing, fusion and cladding, can be used during fabrication.
- (7) The inhomogeneous broadened emission line of fluorescence in glass is advantageous for pulse and *Q*-switched laser applications.

These characteristics of glass, except for the last one, apparently are equally advantageous for photoluminescent devices and other applications to be discussed later.

Beginning in the late 1960's, laser glasses based on phosphate systems began to appear in the patent literature.²⁴⁻²⁸ Laser phosphate glasses were developed to overcome inherent disadvantages of silicate systems, such as large inhomogeneous broadening and only moderately high quantum efficiency. More recently, the high-power glass laser has begun to be used for plasma production.²⁹ High-power laser operation requires glass with a reduced nonlinear refractive coefficient n_2 to avoid the damaging self-focussing effect. The n_2 value is known to be lowest in fluoroberyllate glasses.⁶ However, the use of these glasses has so far been impractical because of the toxicity of Be and, also, a strong tendency for crystallization. Recently, fluorozirconate glasses with n_2 values^{31,32} of

$0.8-0.9 \times 10^{-13}$ that contain no BeF_2 have been prepared and are reported to have a much reduced tendency for crystallization. A nonlinear refractive index can also be reduced by replacing part of the oxygen by fluorine in the phosphate glass.³⁰ Some fluorophosphate laser glass compositions have been disclosed recently.³³ In one fluorophosphate glass of undisclosed composition, the Nd^{3+} fluorescent decay time was reported to be about 20% longer than that of the base phosphate glass.³⁰ Unfortunately, very little has been reported on the fluorescence of rare earths in these new glasses.

Cathodoluminescent glasses that luminesce when bombarded by high energy electrons offer other interesting applications. Such glasses would be particularly suitable for the production of transparent face plates, screens for cathode ray tubes, or other applications where image contrast and image resolution are of vital importance. Several cathodoluminescent glass compositions based on silicate and aluminosilicate^{35,36} glass systems have been reported. However, the cathodoluminescent power efficiency of these glassy phosphors is at most 2%, compared with 10 ~ 20% for practical crystalline phosphors. The lower efficiency of glassy phosphors can be partially compensated by the inherent characteristics of glass, i.e., its transparency and freedom from scattering inclusions and grain boundaries. In any case, the preparation of much improved cathodoluminescent glass seems highly desirable. For this purpose, a high activator concentration might not be as effective as for other applications, because most activator centers could become nonradiative centers upon irradiation from a high energy electron beam. The effect of nonoxidic glass formers on cathodoluminescence seems to be one of the most interesting areas remaining to be explored.

Quite different behavior of luminescent glasses might be expected with low-energy electron excitation. Low-energy electrons such as those found in a gas discharge plasma have energy comparable to that of uv or vacuum uv photons, so that they have far less tendency to react with glass constituents, including the activator ions. Indeed, we have recently found that some of our Tb-activated metaphosphate glasses could be excited effectively by the low-energy electrons in argon and nitrogen gas discharges.³⁷ However, the highly insulative nature of these glasses has so far made difficult the quantitative assessment of this interesting phenomenon.

Glass scintillators for the detection of high energy x-ray and γ -ray radiation is another interesting application possibility for luminescent glasses.

Some Ag-doped glasses have been used in dosimeters for x-ray and γ -ray exposure.³⁸ Exposure to high-energy radiation causes new fluorescent centers to form, and the intensity of fluorescence from these

newly-formed centers under uv excitation gives a measure of the radiation dose. However, it is more desirable to use the fluorescence that is generated directly by the x-ray or γ -ray excitation. High activator concentration in the glass for such an application seems to be highly advantageous as pointed out later.³⁹ Moreover, the parallelism between cathodoluminescent and x-ray efficiency that seems to exist in the crystalline phosphors with a low activator concentration⁴⁰ might not be valid in glassy phosphors with a high activator concentration. The reason for this is the difference in activator ion behavior with a charged particle beam (i.e., electron beam) compared to that with electromagnetic radiation (x-ray and γ -ray).

To our knowledge, no work on x-ray or γ -ray glassy phosphors has been reported. Since x-ray or γ -ray scintillators are of great importance in the field of medical diagnosis and industrial testing, further exploration of this area is of interest.

In summary, the study of luminescent glasses has regained its momentum with the practical application of laser glasses. For the first time, effective utilization has been made of the inherent nature of glass as a host for fluorescent ions. Nonoxidic glasses, such as the fluoride and fluorophosphate, which had been used only in a small volume as special purpose optical glasses, have been recognized as important glassy hosts in luminescent glasses. However, viewing the present status of luminescent glass research, one notices the presence of two different approaches having little mutual interaction. On the one hand are those, mostly glass technologists, who are interested in the empirical development of luminescent glasses of practical importance, and on the other hand, there are those, physicists and chemists, who are interested in fluorescence in glasses mostly in relation to that in crystals. To improve the understanding of fluorescence in glass and to prepare better luminescent glasses for various applications, these seemingly uncoupled research efforts must eventually be brought into harmony. This is one objective of our current studies.

This brief introduction to luminescent glass concludes with a brief description of the papers to follow. The first paper, "Fluorescent Properties of Alkali and Alkaline Earth Metaphosphate Glass Phosphors," deals with fluorescent and optical properties of various activators in the metaphosphate glass. The effect of glass composition on the fluorescence of some activators is reported. For certain activators, i.e., Tl, Sm, Eu, and Tb, concentration quenching effects are described. The behavior of concentration quenching of Eu and Tb in the metaphosphate glass host is found to be considerably different from that in usual crystalline hosts such as Y_2O_3 and Y_2O_2S . It is suggested that a different quenching mechanism may be needed to explain this observation.

The second paper, "Concentration Quenching of Luminescence in a Disordered System with Dipolar Interaction," deals with a new quenching model that is proposed to explain concentration quenching in the sodium yttrium terbium metaphosphate glass. The model is of special interest as the first application of Anderson's migration model in amorphous materials to concentration quenching in glass.

The third paper, "Luminescence of Certain Terbium Metaphosphate Glasses under X-Ray Excitation," presents results of an application-oriented investigation of these glasses as x-ray scintillators. The results clearly demonstrate the advantages of a high activator concentration. The paper also discusses possible use of these glasses in fiber form for x-ray intensifier screens.

The fourth and last paper, "Thermal Properties of New Metaphosphate Glasses", presents results from thermal measurements. It is demonstrated that such parameters as the glass transition temperature and the thermal expansion coefficient can be changed considerably with glass composition. This serves as a good example of the flexibility of a glassy host.

Acknowledgment

The author wishes to thank E. O. Johnson for continuous encouragement and guidance during the preparation of the manuscript. He is also grateful to F. Okamoto for critical reading of the manuscript.

References

- ¹See, for example, (a) J. D. Mackenzie, "General Aspects of the Vitreous State," in *Modern Aspects of the Vitreous States*, ed. J. D. Mackenzie, Vol. 1 p. 1, Butterworths, London (1964) and (b) R. H. Doremus, *Glass Science*, p. 1, John Wiley & Sons, (1973).
- ²W. H. Zachariasen, "Atomic Arrangement in Glass," *J. Amer. Chem. Soc.*, **54**, (10), p 3841 (1932).
- ³K. H. Sun, "Fundamental Condition of Glass Formation," *J. Amer. Ceram. Soc.*, **30**, p. 277 (1947).
- ⁴A. D. Pearson, "Sulphide, Selenide and Telluride Glasses," in *Modern Aspects of the Vitreous State*, ed. J. D. Mackenzie, **3**, p. 29, Butterworths, London (1964).
- ⁵J. D. Mackenzie, "Structure of Glass Forming Halides I. Liquid Beryllium Fluoride," *J. Chem. Phys.*, **32**, p. 1150 (1960).
- ⁶K. H. Sun, "Fluoride Glasses," *Glass Tech.*, **20** (1), p. 36 (1979).
- ⁷W. A. Weyl, "The Fluorescence of Glasses," in *Coloured Glasses*, pp. 439-94, Society of Glass Technology, Sheffield, England (1951).
- ⁸W. Hänlein, *Luminescent Glass*, U.S. Patent 2,219,895 (Apr. 19, 1939).
- ⁹H. Fischer, *Luminescent Glass and Method of Making Same*, U.S. Patent 2,049,765 (June 24, 1933).
- ¹⁰R. F. Reade, *Transparent, Crystalline, Cathodoluminescent Materials*, U.S. Patent 3,926,838 (Dec. 16, 1975).
- ¹¹H. P. Hood, *Fluorescent Glass*, U.S. Patent 2,215,040 (Sept. 17, 1940).
- ¹²G. Aschermann, *Luminescent Material*, U.S. Patent 2,257,667 (Sept. 30, 1941).
- ¹³M. Hüniger and H. Panke, *Luminescent Glass*, U.S. Patent 2,284,055 (May 17, 1939).
- ¹⁴M. Hüniger, *Luminescent Material*, U.S. Patent 2,241,950 (May 13, 1941).
- ¹⁵M. Hüniger and H. Panke, *Luminescent Material*, U.S. Patent 2,270,124 (June 13, 1942).

- ¹⁶G. E. Rindone, "Luminescence in the Glassy State," in *Luminescence of Inorganic Solids*, ed. P. Goldberg, pp. 419-64, Academic Press, New York (1966).
- ¹⁷T. H. Maiman, "Stimulated Optical Radiation in Ruby," *Nature*, **187**, p. 493 (1960).
- ¹⁸E. Snitzer, "Optical Maser Action of Nd³⁺ in a Barium Crown Glass," *Phys. Rev. Lett.*, **7**, p. 444 (1961).
- ¹⁹R. Reisfeld, "Spectra and Energy Transfer of Rare Earths in Inorganic Glasses," *Structure and Bonding*, **13**, p. 53, Springer-Verlag, Berlin (1973).
- ²⁰C. G. Young, "Glass Lasers," *Proc. IEEE*, **57**, p. 1267 (1969).
- ²¹E. Snitzer, "Lasers and Glass Technology," *Ceramic Bull.* **52**, p. 516 (1973).
- ²²C. Hirayama and D. W. Lewis, "The Effect of Neodymium Environment on its Absorption and Emission Characteristics in Glass," *Phys. Chem. Glasses*, **5**, p. 44 (1964).
- ²³D. W. Harper, "Assessment of Neodymium Optical Maser Glass," *Phys. Chem. Glasses*, **5**, p. 11 (1964).
- ²⁴C. Hirayama and N. T. Melamed, *Laser Phosphate Glass Compositions*, U.S. Patent 3,549,554 (Oct. 17, 1965).
- ²⁵I. M. Buzhinsky, et al., *Nd and Yb Containing Phosphate Glasses for Laser Use*, U.S. Patent 3,846,142 (Sept. 18, 1972).
- ²⁶N. E. Alexeev, et al., *Phosphate Glass for Laser Use*, U.S. Patent 3,979,322 (Apr. 9, 1973).
- ²⁷J. D. Meyers and C. S. Vollers, *Laser Phosphate Glass Compositions*, U.S. Patent 4,075,120 (Feb. 21, 1978).
- ²⁸C. F. Rapp, *Glasses Suitable for Laser Application, Glass Lasers, and Method for Making Same*, U.S. Patent 4,076,541 (Feb. 28, 1978).
- ²⁹G. Dubé, "Glass for Fusion Research," *Optical Spectra*, **12** (5), p. 40 (1978).
- ³⁰O. Deutschbein, M. Faulstich, W. Jahn, G. Krolla, and N. Neuroth, "Glasses with a Large Laser Effect; Nd-Phosphate and Nd-Fluorophosphate," *Appl. Optics*, **17**, p. 2228 (1978).
- ³¹M. Poulain, M. Chanthanasinh and J. Lucas, "New Fluoride Glasses," *Mat. Res. Bull.*, **12**, p. 151 (1977) (In French).
- ³²J. Lucas, M. Chanthanasinh, M. Poulain, and P. Brun, "Preparation and Optical Properties of Neodymium Fluorozirconate Glasses," *J. Non-Cryst. Solids*, **27**, p. 273 (1978).
- ³³T. Izumitani and M. Tsutome, *Fluorophosphate-base Laser Glasses*, U.S. Patent 4,120,814 (Oct. 17, 1978).
- ³⁴S. W. Borber and W. F. Nelson, *Luminescent Device, Process, Composition, and Article*, U.S. Patent 3,855,144 (Dec. 17, 1974).
- ³⁵R. F. Reade, *Cathodoluminescent Glasses Activated by Manganese*, U.S. Patent 3,962,117 (June 8, 1976).
- ³⁶M. S. Mizzoni and R. F. Reade, *Cathodoluminescent and Photoluminescent Glasses*, U.S. Patent 4,102,805 (July 25, 1978).
- ³⁷T. Takahashi, H. Fujita, and O. Yamada, "Luminescence of Terbium-Activated Alkali Metaphosphate Glasses," *Proc. 176th Symp. Phosphor Res.*, p. 7, July 13, 1979 (In Japanese).
- ³⁸R. Yokota and H. Imagawa, "Radiophotoluminescent Centers in Silver-Activated Phosphate Glass," *J. Phys. Soc. Japan*, **23**, p. 1038 (1966).
- ³⁹T. Takahashi and O. Yamada, "Luminescence of Certain Terbium Metaphosphate Glasses under X-Ray Excitation," *RCA Review*, **41**, p. 110, March 1980 (this issue).
- ⁴⁰J. A. de Poorter and A. Brill, "Absolute X-ray Efficiencies of Some Phosphors," *J. Electrochem. Soc.*, **122**, p. 1086 (1975).

Fluorescent Properties of Alkali and Alkaline Earth Rare Earth Metaphosphate Glass Phosphors

T. Takahashi and O. Yamada

RCA Research Laboratories, Inc., Machida City, Tokyo, Japan

Abstract—The fluorescence of various activators was investigated in alkali or alkaline earth rare earth metaphosphate glasses having the composition $nM_2O \cdot R_2O_3 \cdot (n + 3)P_2O_5$ or $nM'O \cdot R_2O_3 \cdot (n + 3)P_2O_5$, where $n \geq 0$, M = alkali, M' = alkaline earth, and R = yttrium or rare earth. Absorption, excitation, and emission spectra of Ag, Tl, Ce, Sm, Eu, Gd, and Tb or Tm were measured. The effect of activator concentration on fluorescence was also investigated in Tl, Sm, Eu and Tb-activated glasses. The suppressed concentration quenching in these glasses indicates that the activator ions are well insulated by the network of PO_4 tetrahedra as in crystalline alkali rare earth or rare earth meta- and pentaphosphate phosphors.

1. Introduction

Several rare earth meta- and pentaphosphates^{1,2} and alkali rare earth phosphates^{3,4} containing a stoichiometric and high concentration of Nd have been reported to be efficient laser materials. More recently, lithium rare earth phosphates $LiY_{1-x}R_xP_4O_{12}$ and rare earth metaphosphates $Y_{1-x}R_xP_3O_9$, R = Tb or Eu, have also been found to show strong emissions at high Tb or Eu concentrations.⁵ The crystal structures of these phosphates have been determined, and the suppressed concentration quenching of fluorescence was attributed to the reduced interactions of activator rare earths in the continuous PO_4 tetrahedra network in the phosphates.^{2,4,6-8} In metaphosphates with O/P = 3, all PO_4 tetrahedra share corners to form a continuous one-dimensional chain. For an O/P ratio of less than 3, as in pentaphosphates (O/P = 2.8), the network is

cross-linked. The same network structure of PO_4 tetrahedra is also known to exist in alkali phosphate glasses.⁹ At the critical ratio, $\text{O/P} = 3$, the network is again continuous, though long-range order is missing. A series of alkaline earth metaphosphates $\text{M}'(\text{PO}_3)_2$, $\text{M}' = \text{Mg, Ca, Sr, or Ba}$, is also known to form a glass with a probable PO_4 linear chain structure.¹⁰ One can therefore expect that an alkali or alkaline earth rare earth metaphosphate glass, if it exists in stable form, also has a continuous PO_4 tetrahedra network. In such a glass, the atomic arrangement around activator ions should not be much different from that in its crystalline counterparts, so that suppressed concentration quenching should equally be expected. We have found that a series of glasses having the composition, $n\text{M}_2\text{O}\cdot\text{R}_2\text{O}_3\cdot(n+3)\text{P}_2\text{O}_5$ or $n\text{M}'\text{O}\cdot\text{R}_2\text{O}_3\cdot(n+3)\text{P}_2\text{O}_5$, where $n \geq 0$, $\text{M} = \text{alkali}$, $\text{M}' = \text{alkaline earth}$, and $\text{R} = \text{yttrium or rare earth}$, can be prepared easily and that such glasses can be made to fluoresce effectively when a suitable activator is incorporated. Fluorescent and optical properties of some of these glasses will be reported in the following sections.

2. Experimental Procedure

2.1 Sample Preparation

Stoichiometric quantities of M_2HPO_4 or M_2CO_3 , or $\text{M}'\text{HPO}_4$ or $\text{M}'\text{O}$, $(\text{NH}_4)_2\text{HPO}_4$, R_2O_3 , and an activator (AgCl , TlCl , CeO_2 , Sm_2O_3 , Eu_2O_3 , Tb_4O_7 or Tm_2O_3) were thoroughly mixed in a ball mill. The rare earth oxides were of 99.9% grade. All other reagents were of c.p. grade. The mixture was placed in a high alumina crucible with a lid and slowly ($15 - 30^\circ\text{C/hr}$) heated to above 600°C . After completion of gas evolution, the mixture was rapidly heated to $1000-1400^\circ\text{C}$. The glassy melt was kept at the casting temperature for 2 to 3 hours and then poured into a cylindrical graphite die 20 mm in diameter. After annealing in an electric furnace at a temperature between $300-550^\circ\text{C}$ to remove thermal stress, the melt was slowly cooled to room temperature. A glass plate a few mm thick was cut from the annealed glass block with a Buehler Isomet® low-speed diamond saw. The glass plate was ground and polished for the various measurements.

2.2 Measurements

Excitation, emission and transmission spectra were measured with a Hitachi MPF-4 fluorescence spectrophotometer equipped with an on-line data processor. In the excitation and emission spectra measurements, the emission from the glass surface ground with 4000-mesh

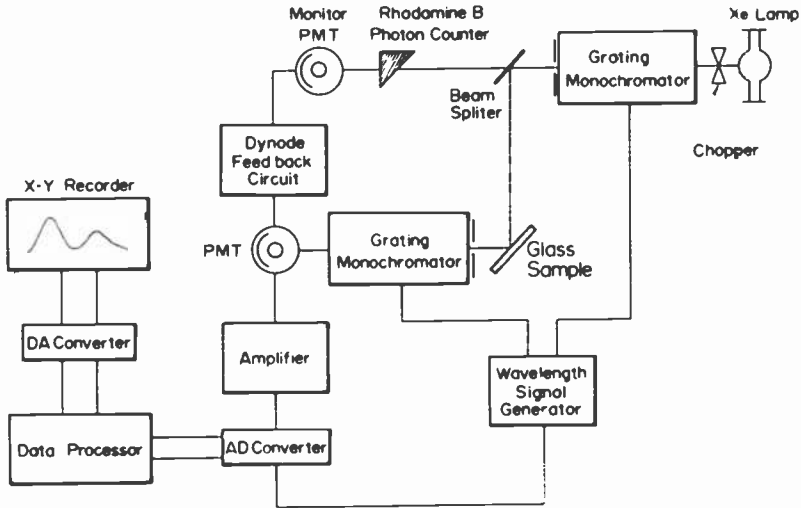


Fig. 1—Block diagram of experimental setup for fluorescence measurement.

abrasive was detected at right angles to the exciting light in the reflection mode. The transmission spectra were measured on the glass samples polished with a $1\text{-}\mu\text{m}$ diamond paste. The excitation spectra were corrected for the spectral sensitivity of the instrument assuming constant quantum efficiency of a rhodamine B solution (Wako Chemicals). Emission spectra were obtained under constant excitation intensity conditions using the same Rhodamine B quantum counter, but were not corrected for the wavelength-dependent sensitivity of the HTV* R446F photomultiplier tube detector. All measurements were made at room temperature. Fig. 1 shows a block diagram of the experimental setup for fluorescence measurement.

3. Results and Discussion

3.1 Ag-Activated Glass

A series of glasses having the composition $6(1-x)\text{Na}_2\text{O}\cdot 6x\text{Ag}_2\text{O}\cdot \text{Y}_2\text{O}_3\cdot 9\text{P}_2\text{O}_5$ were investigated. No appreciable concentration quenching was observed up to $x = 0.05$. At $x = 0.1$ the glass became opaque indicating that complete dissolution of Ag was impossible at this concentration.

* Hamamatsu TV Co., Inc.

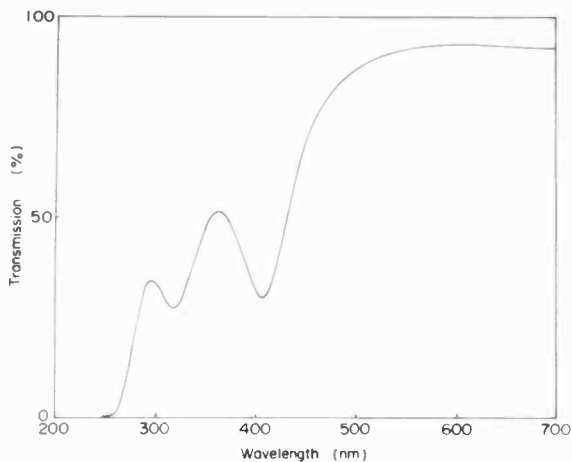


Fig. 2—Transmission spectrum of $5.88\text{Na}_2\text{O}\cdot 0.12\text{Ag}_2\text{O}\cdot \text{Y}_2\text{O}_3\cdot 9\text{P}_2\text{O}_5$ glass 3.8 mm thick.

At lower Ag concentrations, a transparent melt was obtained but precipitation of colloidal silver occurred during casting, and the glass was tinted an amber color.¹¹ The transmission spectrum of such a tinted glass ($x = 0.02$) is shown in Fig. 2. At $\lambda \approx 405$ nm there is a strong absorption band caused by colloidal silver precipitation. There is another absorption band at about 320 nm most probably due to neutral Ag atom centers. The emission spectra of the same glass excited at two different wavelengths are shown in Fig. 3. As can be seen, there exist three different emission

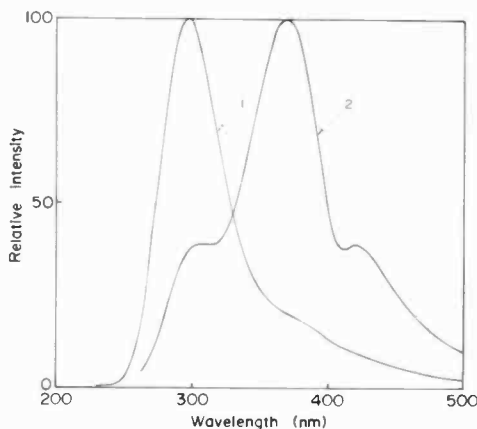


Fig. 3—Emission spectra of $5.88\text{Na}_2\text{O}\cdot 0.12\text{Ag}_2\text{O}\cdot \text{Y}_2\text{O}_3\cdot 9\text{P}_2\text{O}_5$ glass with exciting wavelengths: (1) 220 nm and (2) 250 nm.

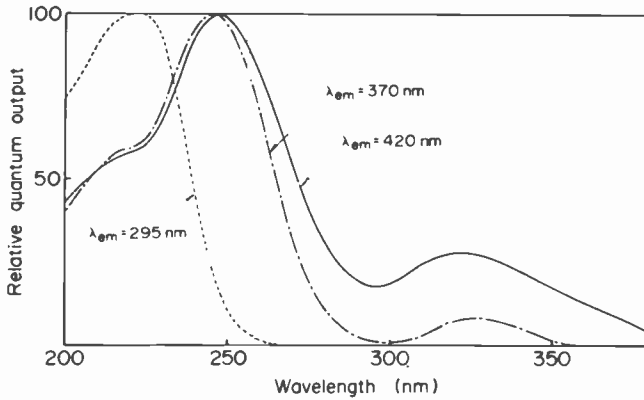


Fig. 4—Excitation spectra for 295-nm, 370-nm, and 420-nm emission bands in $5.88\text{Na}_2\text{O}\cdot 0.12\text{Ag}_2\text{O}\cdot \text{Y}_2\text{O}_3\cdot 9\text{P}_2\text{O}_5$ glass.

bands with peak maximum wavelengths, $\lambda_{pk} = 295$ nm, 370 nm, and 420 nm. The excitation spectra for the three emission bands are shown in Fig. 4. The energy levels associated with the 295-nm band are obviously different from those of the other two bands. A weak excitation band at 320 ± 10 nm for the 370- and 420-nm emission bands coincides with the absorption band observed at the same wavelength in Fig. 1. It has been reported that when Ag atoms are completely ionized to Ag^+ ions in the glass, no visible emission results.¹¹ Accordingly, the 295-nm band may be due to the $4d^{10} \rightarrow 4d^94s$ transition of the Ag^+ ions. The longer wavelength bands are due to the transitions between energy levels of a neutral Ag atom. To confirm this assignment, it is necessary to control the Ag^+ ion and Ag atom concentrations. The effect of network modifiers other than Na and Y on the Ag emission is yet to be investigated.

3.2 Tl-Activated Glass

Various Tl-activated glasses were investigated having compositions $n(1 - y)\text{M}_2\text{O}\cdot n\text{y}\text{Ti}_2\text{O}\cdot \text{R}_2\text{O}_3\cdot (n + 3)\text{P}_2\text{O}_5$ and $n\text{M}'\text{O}\cdot m\text{Ti}_2\text{O}\cdot \text{R}_2\text{O}_3\cdot (n + m + 3)\text{P}_2\text{O}_5$, where M = alkali, M' = alkaline earth, and R = Y or La. All these glasses were fairly transparent in the visible region. Typical transmission spectra are shown in Fig. 5. The absorption edge was found to shift to longer wavelengths with increasing Tl content. However the effect of other network modifiers, M, M', or R, on the transmission spectrum was negligible. The uv absorption and emission bands of Tl in the glass are known to be due to the $^1\text{S}_0 \rightleftharpoons ^3\text{P}_1$ transition of the Tl^+ ion.¹²⁻¹⁴ However, no detailed investigation on the effect of Tl concentration was reported. Our investigations revealed that the peak maximum wavelength λ_{pk} of

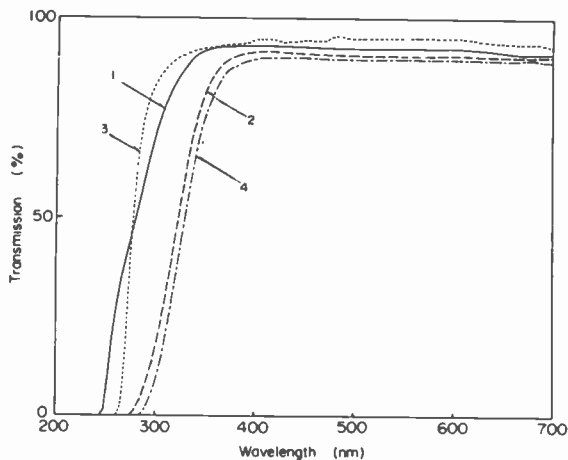


Fig. 5 — Transmission spectra of Tl-activated glasses:

Glass composition	Tl ₂ O mol %	Thickness (mm)
1. 1.95Na ₂ O·0.05Ti ₂ O·Y ₂ O·5P ₂ O ₅	0.6	5.00
2. Na ₂ O·Ti ₂ O·Y ₂ O ₃ ·5P ₂ O ₅	12.5	3.35
3. 8BaO·0.5Ti ₂ O·La ₂ O ₃ ·11.5P ₂ O ₅	2.5	2.65
4. 4BaO·1.5Ti ₂ O·Y ₂ O ₃ ·8.5P ₂ O ₅	10.0	5.40

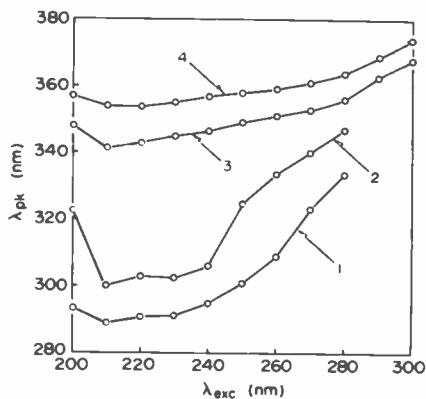


Fig. 6 — Dependence of peak maximum wavelength λ_{pk} of Tl emission band on exciting wavelength λ_{exc} in barium thallium yttrium glasses: (1) 8BaO·0.1Ti₂O·Y₂O₃·11.1P₂O₅; (2) 8BaO·0.5Ti₂O·Y₂O₃·11.5P₂O₅; (3) 8BaO·Ti₂O·Y₂O₃·11P₂O₅; and (4) 8BaO·1.5Ti₂O·Y₂O₃·12.5P₂O₅.

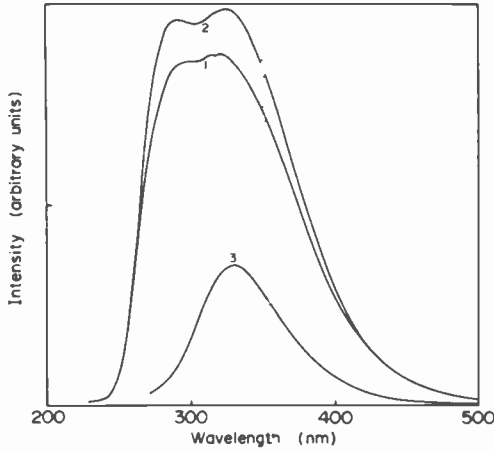


Fig. 7—Emission spectra of Ti^{+} in $1.6Li_2O-0.4Ti_2O-Y_2O_3-5P_2O_5$ glass excited at different wavelengths; (1) 215 nm, (2) 230 nm, and (3) 260 nm.

the Ti^{+} emission band shifts towards longer wavelengths with increasing Ti content in all the glasses. This wavelength λ_{pk} also changed with exciting wavelength. A typical example of such data in Ba-Ti-Y glasses is shown in Fig. 6. Moreover, in Li and Mg-Ti-R glasses the emission band was resolved into two bands with $\lambda_{pk} = 280 \pm 10$ nm and 340 ± 10 nm, respectively. It was also found that the intensity of the low-energy emission band increases and that of the high-energy band decreases with

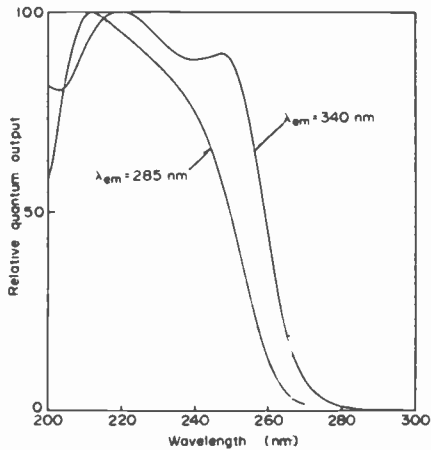


Fig. 8—Excitation spectra of Ti^{+} emission in $1.6Li_2O-0.4Ti_2O-Y_2O_3-5P_2O_5$ glass monitored at 285 nm and 340 nm.

increasing Tl content. Therefore, the observed change in λ_{pk} with Tl content must arise from the change of intensity of the two emission bands. From these results, the high-energy band can be attributed to Tl^+ monomer centers, and the low-energy band to the Tl^+-Tl^+ dimer and/or Tl^+ aggregate centers. The appearance of the two emission bands can be seen in the emission spectra of Tl^+ in $1.6Li_2O-0.4Tl_2O-Y_2O_3-5P_2O_5$ glass under excitation at three different wavelengths as shown in Fig. 7. The excitation spectra for the two emission bands in the same glass are shown in Fig. 8. More detailed discussion of these and other results for alkali thallium yttrium metaphosphate glasses can be found elsewhere.¹⁵

In both alkali and alkaline earth -Tl-R glasses the emission band became unresolvable with the increase of the atomic number of alkali or alkaline earth. This is probably due to overlapping of energy levels responsible for the high- and low-energy emission bands. Conceivably, as the ionic radius of network modifier increases, the interaction between Tl^+ and the modifier ions increases to perturb the energy levels of Tl^+ . Fig. 9 shows the emission spectra of Tl^+ in a Mg-Tl-La glass and four Ba-Tl-R glasses. The emission spectrum of the Mg-Tl-Y glass clearly indicates the presence of two emission bands. On the other hand, the emission spectra of the Ba-Tl-R glasses appear to consist of an unsplit broad emission band with a λ_{pk} shifting to longer wavelengths with Tl concentration. It is also obvious that changes in R (R = Y or La) cause

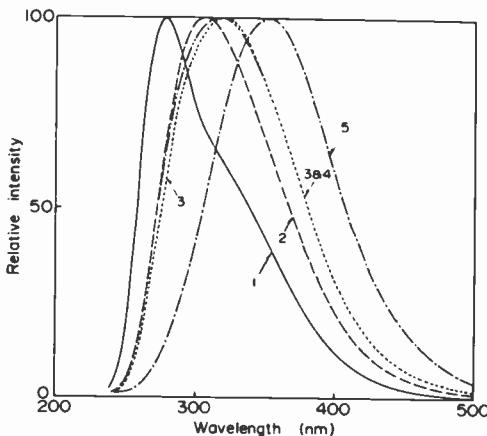


Fig. 9—Emission spectra of Tl^+ in alkaline earth thallium yttrium or lanthanum glasses excited at 230 nm: (1) $8MgO-0.5Tl_2O-La_2O_3-11.5P_2O_5$; (2) $8BaO-0.5Tl_2O-La_2O_3-11.5P_2O_5$; (3) $4BaO-0.5Tl_2O-La_2O_3-7.5P_2O_5$; (4) $4BaO-0.5Tl_2O-Y_2O_3-7.5P_2O_5$; and (5) $4BaO-1.5Tl_2O-Y_2O_3-7.5P_2O_5$.

little change in the emission spectrum of Ba-Tl-R glasses. This is also true for other alkali or alkaline earth Tl glasses. In all the glass systems, concentration quenching of the low-energy emission band accelerated at higher Tl concentrations in excess of 10 mol% Tl_2O , indicating enhanced quenching interactions in higher aggregates of Tl^+ .

3.3 Gd and Gd-Tl Activated Glasses

The element Gd in glasses is known to have an emission band at 312 ± 1 nm corresponding to the ${}^6P_{7/2} \rightarrow {}^8S_{7/2}$ transition of the Gd^{3+} ion.¹⁶ However, this fluorescence is weak due to the weak absorption of the excited levels of Gd^{3+} . Reisfeld and Morag¹⁷ found that the 312-nm band could be sensitized by Tl coactivation (0.01% Tl) in sodium borate and phosphate glasses containing 3% Gd. We also found that the sensitization of Gd^{3+} emission occurs in various glasses with a higher Gd and/or Tl content, such as in $n(1-x)MO \cdot nxTl_2O \cdot Gd_2O_3 \cdot (n+3)P_2O_5$. Fig. 10 shows the emission spectra of $2(1-x)Na_2O \cdot 2nxTl_2O \cdot Gd_2O_3 \cdot 5P_2O_5$ glasses, with $x = 0, 0.05,$ and 0.1 under 250 nm excitation, as well as the excitation spectra of Gd^{3+} emission in the same glasses monitored at 311 nm. In the Tl-containing glasses, the Gd emission at 311 nm was enhanced, but the Tl emission was suppressed almost completely. It should also be noted that the excitation spectra for Gd^{3+} emission in the Tl-

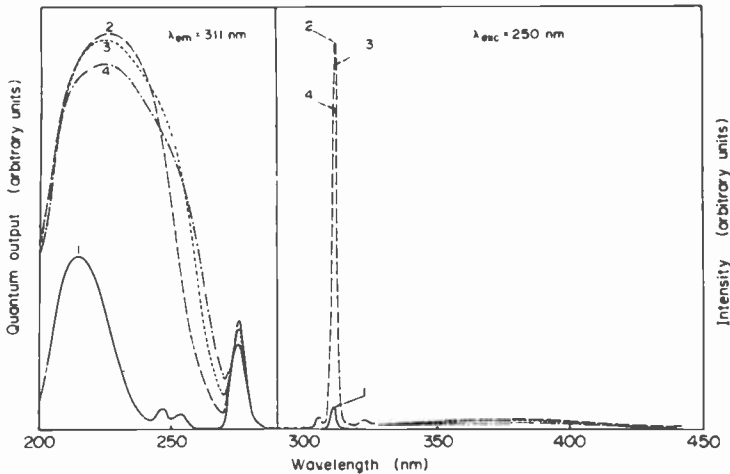


Fig. 10—Emission spectra of Gd^{3+} and Tl^+ excited at 250 nm, and excitation spectra of Gd^{3+} emission monitored at 311 nm in sodium gadolinium and sodium thallium gadolinium glasses: (1) $2Na_2O \cdot Gd_2O_3 \cdot 5P_2O_5$; (2) $1.8Na_2O \cdot 0.2Tl_2O \cdot Gd_2O_3 \cdot 5P_2O_5$; (3) $1.6Na_2O \cdot 0.4Tl_2O \cdot Gd_2O_3 \cdot 5P_2O_5$; and (4) $1.4Na_2O \cdot 0.6Tl_2O \cdot Gd_2O_3 \cdot 5P_2O_5$

coactivated glasses are almost identical to those of Tl^+ emission in a Li-Tl-Y glass (Fig. 8) except for the excitation band at about 275 nm due to the ${}^6S_{7/2} \rightarrow {}^6I$ transition of Gd^{3+} .

From these observations it can be concluded, as suggested before,¹⁷ that the enhancement of Gd^{3+} emission is brought about by the energy transfer from the 3P_1 state of Tl^+ to the ${}^6P_{7/2}$ state of Gd^{3+} . No such enhancement of Gd^{3+} emission was observed in non-alkali containing glasses, $nTi_2O \cdot (1-x)Y_2O_3 \cdot xGd_2O_3 \cdot (n+3)P_2O_5$. Presumably, the quenching of excitation in Tl^+ higher aggregates prevents the energy transfer to the ${}^6P_{7/2}$ level of Gd^{3+} in these glasses.

3.4 Tm-Activated Glass

Glasses were investigated having compositions $2Na_2O \cdot (1-x)Y_2O_3 \cdot xTm_2O_3 \cdot 5P_2O_5$ ($x = 0.05, 0.1, \text{ and } 0.3$), $nK_2O \cdot 0.9Y_2O_3 \cdot 0.1Tm_2O_3 \cdot (n+3)P_2O_5$ ($n = 1, 2$), and $4BaO \cdot 0.7Y_2O_3 \cdot 0.3Tm_2O_3 \cdot 7P_2O_5$. The transmission spectra of one of the Na-Y-Tm glasses and the Ba-Y-Tm glass are shown in Fig. 11. The absorption bands appeared at wavelengths almost identical to those in sodium phosphate glass containing 3 wt% Tm.¹⁸ These bands can be attributed to the transitions from the 3H_6 ground state of Tm^{3+} to higher multiplets. The absorption intensities were proportional to Tm concentration as expected. The absorption band positions were little influenced by the network modifier (Na, K, or Ba). The emission

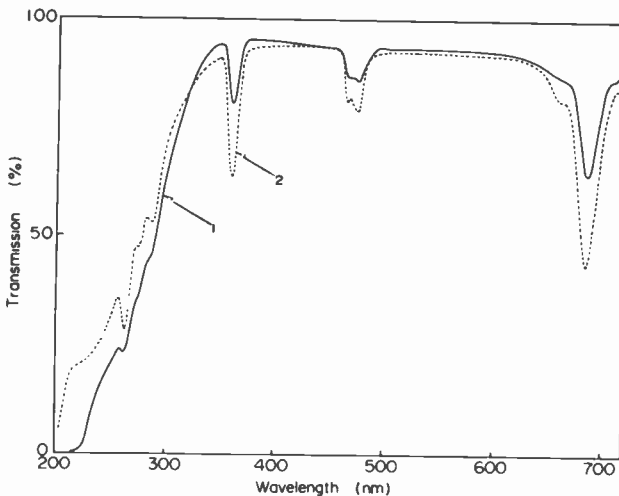


Fig. 11—Transmission spectra of $2Na_2O \cdot 0.9Y_2O_3 \cdot 0.1Tm_2O_3 \cdot 5P_2O_5$ glass (curve 1, thickness 3.4 mm) and $4BaO \cdot 0.7La_2O_3 \cdot 0.3Tm_2O_3 \cdot 7P_2O_5$ glass (curve 2, thickness 2.9 mm).

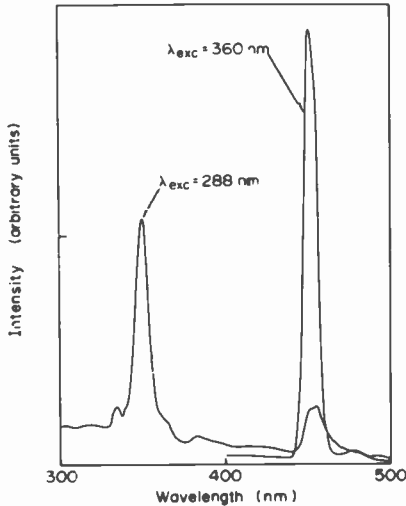


Fig. 12—Emission spectra of Tm^{3+} in $2Na_2O-0.9Y_2O_3-0.1Tm_2O_3-5P_2O_5$ glass excited at 288 nm and 360 nm.

spectra of Tm in these glasses changed with exciting wavelength as in the case of sodium phosphate glass.¹⁸ The emission spectra are shown in Fig. 12 for Tm^{3+} in $2Na_2O-0.9Y_2O_3-0.1Tm_2O_3-5P_2O_5$ glass for two different exciting wavelengths, 288 nm (${}^3H_6 - {}^3P_0$), and 360 nm (${}^3H_6 - {}^1D_2$). For 288-nm excitation, emission bands are observed from transitions ${}^1I_6 \rightarrow {}^3H_4$ (350 nm), ${}^1I_6 \rightarrow {}^3H_5$ (383 nm), and ${}^1D_2 \rightarrow {}^3H_4$ (456 nm). For 360-nm excitation, the emission bands are observed due to transitions ${}^1D_2 \rightarrow {}^3H_4$ (452 nm) and ${}^1G_4 \rightarrow {}^3H_6$ (478 nm). Unlike with sodium phosphate glass, however, the emission band from the ${}^1G_4 \rightarrow {}^3H_4$ transition could not be observed in either case. In all glasses studied, the half bandwidth $\Delta\lambda$ of the ${}^1D_2 \rightarrow {}^3H_4$ band at 452 nm under 360 nm excitation was 10.0 ± 0.5 nm. This is $1/6-1/8$ of the $\Delta\lambda$ value reported for sodium phosphate glass.¹⁸ This difference seems to mean that the number of slightly different Tm^{3+} sites is much smaller in alkali or alkaline earth rare earth metaphosphate glasses than in sodium phosphate glass. On the other hand, concentration quenching was considerable and the emission intensity in $2Na_2O-0.7Y_2O_3-0.3Tm_2O_3-5P_2O_5$ glass was lower by more than a factor of two than in $2Na_2O-0.9Y_2O_3-0.1Tm_2O_3-5P_2O_5$ glass. The excitation spectra are shown in Fig. 13 for the 350-nm and 452-nm emission bands in $2Na_2O-0.9Y_2O_3-0.1Tm_2O_3-5P_2O_5$ glass. These are quite similar to each other. The strong band at 200–210 nm is probably due to the charge transfer states of Tm^{3+} . Since the charge transfer band has been found to appear at a lower energy than the f-d transition

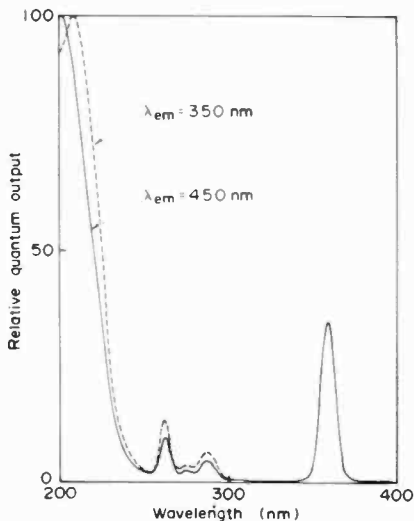


Fig. 13—Excitation spectrum of Tm^{3+} emission in $2\text{Na}_2\text{O}\cdot 0.9\text{Y}_2\text{O}_3\cdot 0.1\text{Tm}_2\text{O}_2\cdot 5\text{P}_2\text{O}_5$ glass monitored at 350 nm and 450 nm.

band for Tm^{3+} in rare earth orthophosphate crystals (RPO_4),¹⁹ we can expect the same in the metaphosphate glass.

3.5 Ce-Activated Glass

Glasses were investigated having the compositions $2\text{Na}_2\text{O}\cdot 0.8\text{Y}_2\text{O}_3\cdot 0.2\text{Ce}_2\text{O}_3\cdot 5\text{P}_2\text{O}_5$, $8\text{BaO}\cdot 0.95\text{La}_2\text{O}_3\cdot 0.05\text{Ce}_2\text{O}_3\cdot 11\text{P}_2\text{O}_5$, and $n\text{MgO}\cdot (1-x)\text{La}_2\text{O}_3\cdot x\text{Ce}_2\text{O}_3\cdot (n+3)\text{P}_2\text{O}_5$, with $n = 1-6$ and $0.05 \leq x \leq 0.35$. The transmission spectrum of a Ce-containing glass showed strong absorption in the uv region but had no fine structure in the visible region. Absorption spectra of Ce^{3+} in sodium borate and phosphate glasses were investigated by Reisfeld.²⁰ In these glasses, five absorption band peaks were observed in the uv region and were attributed to the splitting of the 5d orbitals of Ce^{3+} arising from nonsymmetrical crystal field terms. The emission spectrum of Ce^{3+} in $8\text{BaO}\cdot 0.95\text{La}_2\text{O}_3\cdot 0.05\text{Ce}_2\text{O}_3\cdot 3\text{P}_2\text{O}_5$ glass is shown in Fig. 14. The broad emission band with $\lambda_{\text{pk}} = 340$ nm is due to transitions from the lowest 5d state to the $4f\ ^2\text{H}_{7/2}$ and $^2\text{H}_{5/2}$ states of Ce^{3+} . No significant change in peak position and shape was observed in other glasses containing different network modifiers. Fig. 15 shows the excitation spectra of Ce^{3+} emission in three metaphosphate glasses containing different network modifiers, i.e. Na, Mg or Ba. In $2\text{Na}_2\text{O}\cdot 0.8\text{Y}_2\text{O}_3\cdot 0.2\text{Ce}_2\text{O}_3\cdot 5\text{P}_2\text{O}_5$ glass, four peaks are clearly identified as indicated in the figure. The excitation-band energies are comparable to the

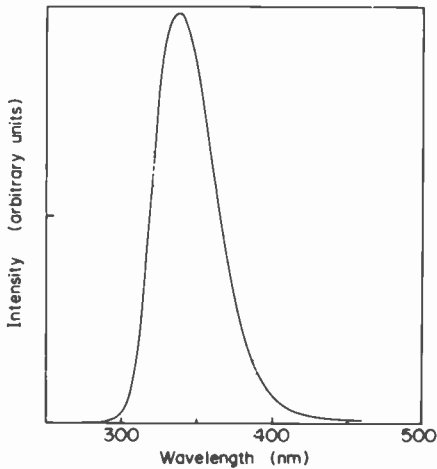


Fig. 14—Emission spectrum of Ce^{3+} in $8\text{BaO}\cdot 0.95\text{La}_2\text{O}_3\cdot 0.05\text{Ce}_2\text{O}_3\cdot 11\text{P}_2\text{O}_5$ glass excited at 220 nm.

absorption-band energies reported for sodium phosphate glass.²⁰ The highest energy 5d band should be in the vacuum uv region ($\lambda < 200$ nm). The excitation-band energies in the other two glasses are almost the same as those in the Na-Y-Ce glass, but the intensities of the excitation bands change considerably. In other words, the network modifier (Na, Ba, or Mg) does not affect the excitation-band energy, but can influence the

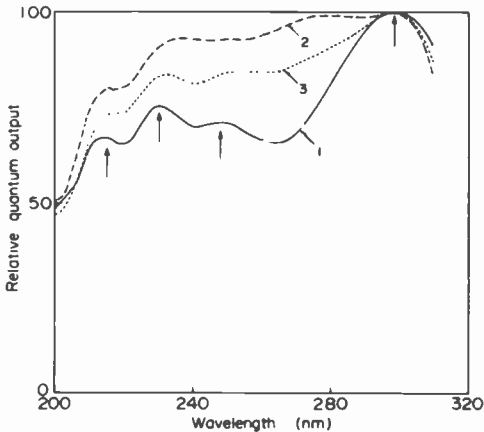


Fig. 15—Excitation spectra of Ce^{3+} emission monitored at λ_{em} : (1) $2\text{Na}_2\text{O}\cdot 0.8\text{Y}_2\text{O}_3\cdot 0.2\text{Ce}_2\text{O}_3\cdot 5\text{P}_2\text{O}_5$, ($\lambda_{\text{em}} = 340$ nm); (2) $6\text{MgO}\cdot 0.95\text{La}_2\text{O}_3\cdot 0.05\text{Ce}_2\text{O}_3\cdot 9\text{P}_2\text{O}_5$, ($\lambda_{\text{em}} = 331$ nm); and (3) $8\text{BaO}\cdot 0.95\text{La}_2\text{O}_3\cdot 0.05\text{Ce}_2\text{O}_3\cdot 11\text{P}_2\text{O}_5$, ($\lambda_{\text{em}} = 338$ nm).

intensity of each excitation band. Concentration quenching of Ce^{3+} emission was considerable and the maximum emission intensity was observed at a concentration below 2 mol% Ce_2O_3 in the Mg-La-Ce MP glasses.

3.6 Sm-Activated Glass

Glasses were investigated having compositions $2\text{Li}_2\text{O}\cdot(1-x)\text{Y}_2\text{O}_3\cdot x\text{Sm}_2\text{O}_3\cdot 5\text{P}_2\text{O}_5$, ($x = 0.05-0.5$), $2\text{Na}_2\text{O}\cdot(1-x)\text{Y}_2\text{O}_3\cdot x\text{Sm}_2\text{O}_3\cdot 5\text{P}_2\text{O}_5$ ($x = 0.05, 0.2$), and $4\text{BaO}\cdot 0.9\text{La}_2\text{O}_3\cdot 0.05\text{Sm}_2\text{O}_3\cdot 7\text{P}_2\text{O}_5$. The transmission spectra of $2\text{Li}_2\text{O}\cdot(1-x)\text{Y}_2\text{O}_3\cdot x\text{Sm}_2\text{O}_3\cdot 5\text{P}_2\text{O}_5$ glasses with $x = 0.02, 0.1$, and 0.5 are shown in Fig. 16. The observed absorption bands are due to 4f-4f transitions from the $^6\text{H}_{5/2}$ ground state to higher multiplets of Sm^{3+} .²¹ The absorption intensities are proportional to Sm concentration. The excitation and emission spectra of Sm^{3+} in $2\text{Na}_2\text{O}\cdot 0.8\text{Y}_2\text{O}_3\cdot 0.2\text{Sm}_2\text{O}_3\cdot 5\text{P}_2\text{O}_5$ glass are shown in Fig. 17. Emission bands are observed due to the transitions $^4\text{G}_{5/2} \rightarrow ^6\text{H}_{5/2}$ (561 nm), $^4\text{G}_{5/2} \rightarrow ^6\text{H}_{7/2}$ (596 nm), $^4\text{G}_{5/2} \rightarrow ^6\text{H}_{9/2}$ (644 nm), and $^4\text{G}_{5/2} \rightarrow ^6\text{H}_{11/2}$ (705 nm). The excitation spectrum was taken on the 596-nm emission. The excitation bands observed in the wavelength range from 300 to 500 nm are due to the 4f-4f transitions of Sm^{3+} , and their peak wavelengths coincide with those of the absorption bands. A strong band at about 200 nm is due to the charge

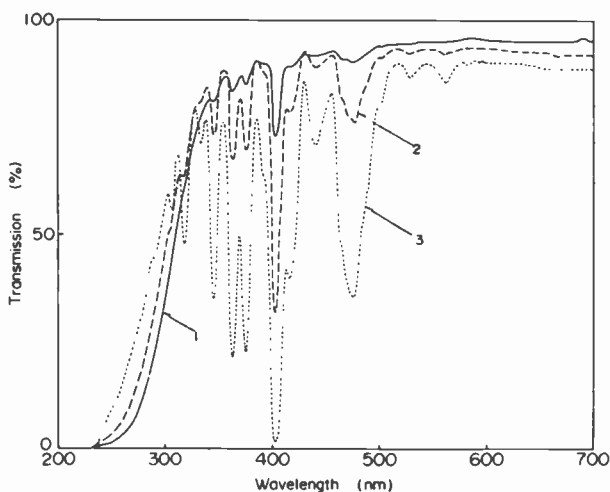


Fig. 16—Transmission spectra of $2\text{Li}_2\text{O}\cdot(1-x)\text{Y}_2\text{O}_3\cdot x\text{Sm}_2\text{O}_3\cdot 5\text{P}_2\text{O}_5$ glasses: (1) $x = 0.02$, thickness 5.4 mm; (2) $x = 0.1$, thickness 5.1 mm; and (3) $x = 0.5$, thickness 5.0 mm

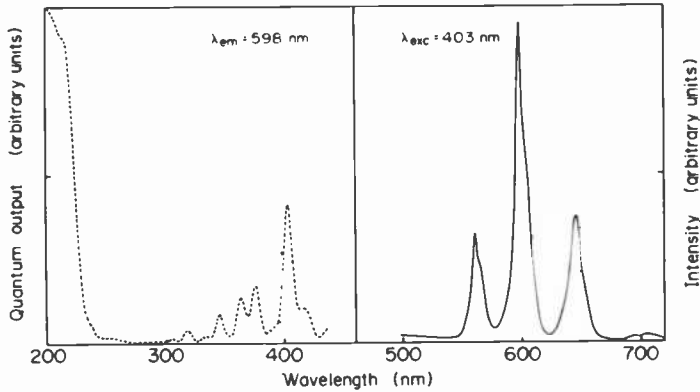


Fig. 17—Emission spectrum of Sm^{3+} excited at 403 nm, and excitation spectrum of Sm^{3+} emission monitored at 598 nm in $2\text{Na}_2\text{O}\cdot 0.8\text{Y}_2\text{O}_3\cdot 0.2\text{Ce}_2\text{O}_3\cdot 5\text{P}_2\text{O}_5$ glass.

transfer transition of Sm^{3+} . These characteristics were almost identical in all the glasses investigated.

Dependence of Sm^{3+} emission intensity on Sm concentration was investigated in $2\text{Li}_2\text{O}\cdot(1-x)\text{Y}_2\text{O}_3\cdot x\text{Sm}_2\text{O}_3\cdot 5\text{P}_2\text{O}_5$ glasses. Results are shown in Fig. 18. Logarithmic plots of the normalized intensity I/x versus x under excitation of the charge transfer band ($\lambda_{exc} = 200$ nm), and the 4f excited bands ($\lambda_{exc} = 362$ and 402 nm), exhibit a similar tendency. This indicates that the same quenching mechanism is operative for the three different exciting radiations.

According to Ozawa,²² normalized intensity with respect to activator concentration, I/C , must be proportional to the radiative transition probability function $f(C)$ when the volume of phosphor on which the intensity of fluorescence is measured is kept constant. The constant effective volume condition was empirically confirmed for the weakly absorbed exciting radiation. Since our spectrophotometer is the same as the one used by Ozawa, this condition is also thought to be satisfied in our measurements. On the other hand, for the exciting radiation whose wavelength is shorter than the absorption edge of the metaphosphate glass, i.e., for the charge-transfer-band excitation, the penetration depth is determined by the reciprocal of the host absorption coefficient. Thus the penetration depth must be independent of activator concentration. Therefore, the constant effective volume condition should also be satisfied in this case, and

$$I/C = K \cdot f(C),$$

where K is a constant and $f(C)$ is a function of activator concentration that is determined by the quenching interaction involved. For quenching

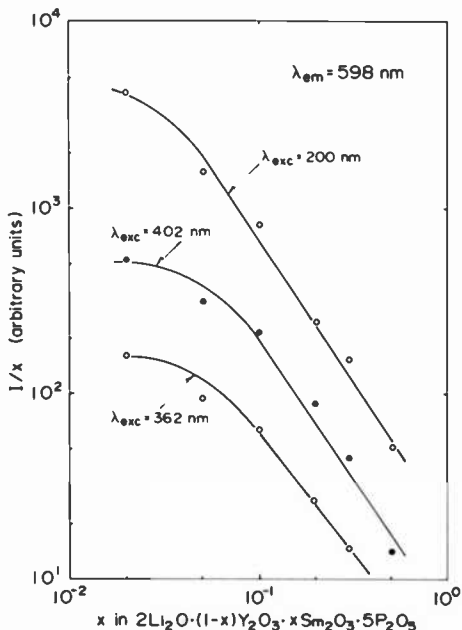


Fig. 18—Concentration dependence curves of normalized intensity of Sm^{3+} emission at 598 nm under excitation at 200 nm (charge transfer), 362 nm (4f), and 402 nm (4f) in $2\text{Li}_2\text{O}\cdot(1-x)\text{Y}_2\text{O}_3\cdot x\text{Sm}_2\text{O}_3\cdot 5\text{P}_2\text{O}_5$ glasses.

arising from magnetic dipole interactions between neighboring activators,

$$f(C) = (1 - C)^Z,$$

where Z is the number of neighboring activator atoms that interact with the central activator atom.^{23,24} For quenching arising from electrostatic multipolar interactions,

$$f(C) = [1 + \beta'(C)^{\theta/3}]^{-1},$$

where $\theta = 6, 8, 10$ for dipole-dipole, dipole-quadrupole, quadrupole-quadrupole interaction, respectively, and β' is a constant for a given host.²⁵

From the straight-line portion of $\log I/x$ vs $\log x$ plots, a dipole-dipole interaction ($\theta \sim 6$) seems to be the most probable quenching mechanism for Sm^{3+} emission in the metaphosphate glass. In comparison with this result, the concentration quenching of Sm^{3+} emission in a crystal host, e.g., $\text{Y}_2\text{O}_3:\text{Sm}$, was found to be much more drastic, and a quadrupole-quadrupole interaction ($\theta \sim 10$) was inferred as a possible mechanism.²²

3.7 Eu-Activated Glass

Glasses were investigated having compositions $nM_2O \cdot (1 - x)Y_2O_3 \cdot xEu_2O_3 \cdot (n + 3)P_2O_5$ and $nBaO \cdot (1 - x)La_2O_3 \cdot xEu_2O_3 \cdot (n + 3)P_2O_5$, with $M = Li$ and Na or K . As in the case of Sm -activated glasses, fluorescent and optical properties of Eu^{3+} were influenced little by the network modifier (alkali, Ba , Y or La) in the glass. The transmission spectra of $2Na_2O \cdot (1 - x)Y_2O_3 \cdot xEu_2O_3 \cdot 5P_2O_5$ glasses, with $x = 0.05, 0.2$, and 0.5 , are shown in Fig. 19. The observed absorption bands are due to the $4f-4f$ transitions from the 4F_0 and 4F_1 states of Eu^{3+} to higher multiplets, and their peak positions are again identical to those observed in sodium phosphate glass.^{26,27}

The excitation and emission spectra of Eu^{3+} in $6Na_2O \cdot 0.5Y_2O_3 \cdot 0.5Eu_2O_3 \cdot 9P_2O_5$ glass are shown in Fig. 20. Observed emission bands are due to the transitions $^5D_0 \rightarrow ^7F_0$ (578 nm), $^5D_0 \rightarrow ^7F_1$ (592 nm), $^5D_0 \rightarrow ^7F_2$ (612 nm), $^5D_0 \rightarrow ^7F_3$ (653 nm), and $^5D_0 \rightarrow ^7F_4$ (700.5 nm). The excitation spectrum monitored on the 612-nm emission consists of sharp narrow bands due to the $4f-4f$ transitions, and a broad band due to the charge transfer transition of Eu^{3+} at about 220 nm.

Dependence of Eu^{3+} emission intensity on Eu concentration was investigated in $2Na_2O \cdot (1 - x)Y_2O_3 \cdot xEu_2O_3 \cdot 5P_2O_5$ glasses. The results are shown in Fig. 21. Unlike the case of Sm^{3+} emission, the quenching be-

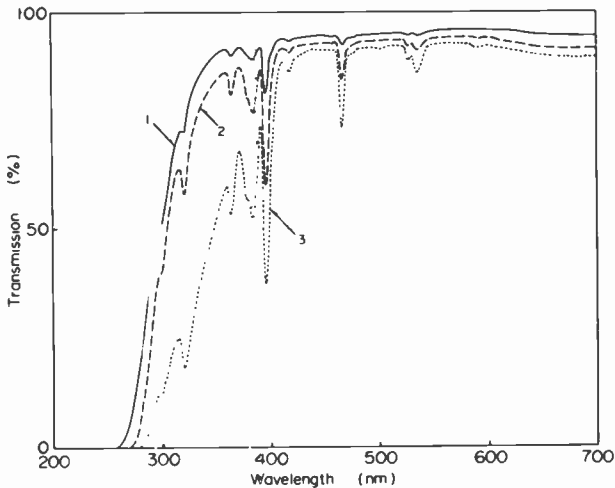


Fig. 19—Transmission spectra of $2Na_2O \cdot (1 - x)Y_2O_3 \cdot xEu_2O_3 \cdot 5P_2O_5$ glasses: (1) $x = 0.05$, thickness 3.2 mm; (2) $x = 0.2$, thickness 3.0 mm; and (3) $x = 0.5$, thickness 3.2 mm.

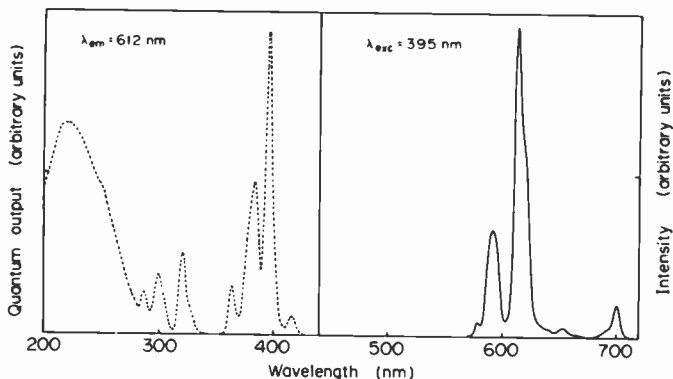


Fig. 20—Emission spectrum of Eu^{3+} excited at 395 nm, and excitation spectrum of Eu^{3+} emission monitored at 612 nm in $6\text{Na}_2\text{O}\cdot 0.5\text{Y}_2\text{O}_3\cdot 0.5\text{Eu}_2\text{O}_3\cdot 9\text{P}_2\text{O}_5$ glass.

behavior of Eu^{3+} emission strongly depends upon the exciting wavelength. Generally, the normalized intensity follows the relation,

$$I/x = K/x^n,$$

where K is a constant that is different for different exciting wavelengths. The exponent n is about unity when excitation involves the charge-transfer band whose molar absorption coefficient is estimated to be of the order of $10^2 - 10^3$.²⁸ However, n approaches zero when the excitation involves radiation of smaller molar absorption coefficients ($k = 10^{-1} \sim 1$ for the 4f-4f bands). This particular quenching behavior cannot be explained by either magnetic dipolar or electrostatic multipolar interactions. The dependence of quenching on the absorption of exciting radiation suggests a mechanism related to nonradiative interactions of activator ions near the surface. That is, for the charge-transfer-band excitation, the emission is generated only from the thin layer near the surface, whereas the emission due to the weakly absorbed 4f-4f band excitation mostly comes from the much deeper region into the sample. Accordingly, if activator ions on the surface are assumed to act as nonradiative centers, one expects stronger quenching for the strongly absorbed exciting radiation than for the weakly absorbed one.

Indeed, such a surface quenching mechanism has recently been proposed to explain concentration quenching of the Nd^{3+} emission in $\text{Y}_{1-x}\text{Nd}_x\text{P}_5\text{O}_{14}$ crystals.²⁹ In this mixed crystal system, relatively stronger quenching of Nd^{3+} emission occurred when excitation took place via the 800-nm band of a high absorption coefficient than when it happened via the 580-nm band of a smaller absorption coefficient.

A similar quenching behavior was also found in the Tb-activated glass,

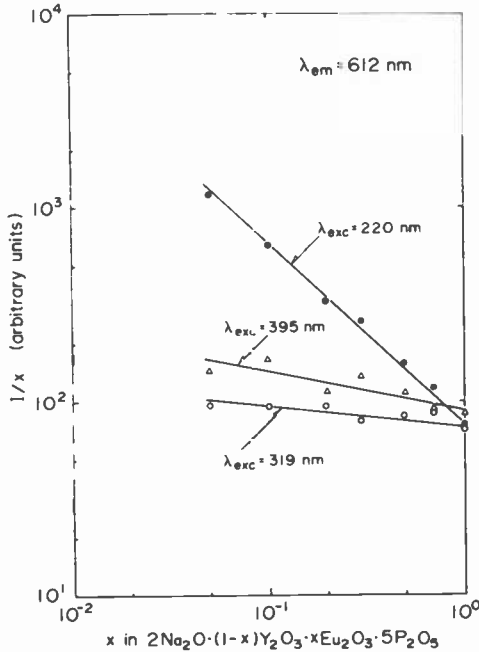


Fig. 21—Concentration dependence curves of normalized intensity of Eu^{3+} emission at 612 nm under excitation of 220 nm (charge transfer), 319 nm (4f), and 395 nm (4f) in $2\text{Na}_2\text{O}\cdot(1-x)\text{Y}_2\text{O}_3\cdot x\text{Eu}_2\text{O}_3\cdot 5\text{P}_2\text{O}_5$ glasses.

as we shall discuss later. However, we have not yet formulated a complete model that explains the observed results quantitatively.

3.8 Tb-Activated Glass

Glasses were investigated having compositions $n\text{M}_2\text{O}\cdot(1-x)\text{Y}_2\text{O}_3\cdot x\text{Tb}_2\text{O}_3\cdot(n+3)\text{P}_2\text{O}_5$ ($n = 2, 4, \text{ or } 6$, $\text{M} = \text{Li, Na, or K}$) and $n\text{M}'\text{O}(1-x)\text{La}_2\text{O}_3\cdot x\text{Tb}_2\text{O}_3\cdot(n+3)\text{P}_2\text{O}_5$ ($n = 2-16$, $\text{M}' = \text{Mg, Ca, Sr, Ba or Pb}$). The results for the alkali yttrium terbium metaphosphate glasses have been reported elsewhere^{30,31} and will not be repeated here. We are mainly concerned with the fluorescent and optical properties of alkaline earth and lead rare earth terbium glasses in this section. The transmission spectra of $4\text{M}'\text{O}\cdot\text{Tb}_2\text{O}_3\cdot 7\text{P}_2\text{O}_5$ glasses with $\text{M}' = \text{Mg, Sr, Ba, and Pb}$ are shown in Fig. 22. These glasses were prepared from high purity Tb_4O_7 raw material that contains less than 20 ppm Ce to avoid Ce sensitization.^{30,31} In the figure, the absorption bands due to the 4f-4f transitions of Tb^{3+} are observed and their position is unchanged with divalent cation species. The absorption edge of the Mg-Tb glass lies at about 265 nm,

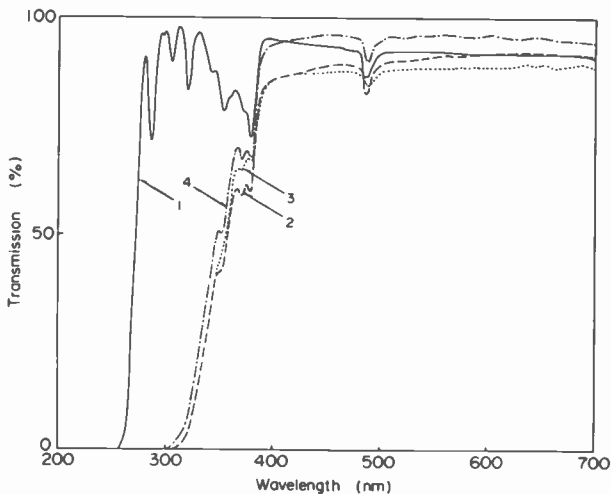


Fig. 22—Transmission spectra of $4M'O\cdot Tb_2O_3\cdot 7P_2O_5$ glasses: (1) $M' = Mg$; (2) $M' = Sr$; (3) $M' = Ba$; and (4) $M' = Pb$.

50–55 nm shorter than those of the other three glasses. This accords with the shortest absorption edge reported for the magnesium metaphosphate glass in a series of metaphosphate glasses, $M'O\cdot P_2O_5$, with $M' = Pb, Ba, Sr, Ca$ or Mg .³² Fig. 23 shows the emission spectrum of Tb^{3+} in $4MgO\cdot Tb_2O_3\cdot 7P_2O_5$ glass. Emission bands due to the transitions ${}^5D_4 \rightarrow {}^7F_n$ are observed. In the glasses containing 10 mol% or lower Tb_2O_3 , the emission bands due to the ${}^5D_3 \rightarrow {}^7F_n$ transitions were also observed. The shape

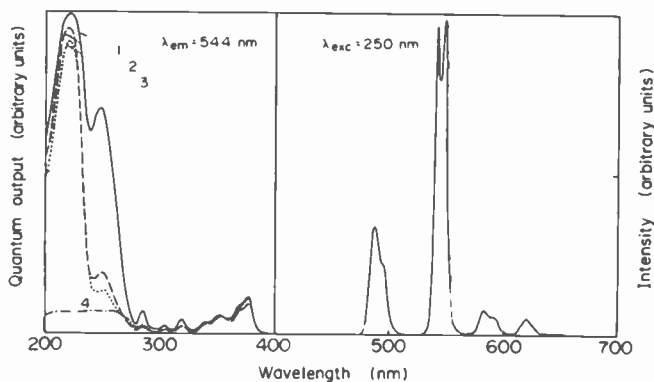


Fig. 23—Emission spectrum of Tb^{3+} in $4MgO\cdot Tb_2O_3\cdot 7P_2O_5$ glass excited at 250 nm, and excitation spectra of Tb^{3+} emission monitored at 544 nm in $4M'O\cdot Tb_2O_3\cdot 7P_2O_5$ glasses: (1) $M' = Mg$; (2) $M' = Sr$; (3) $M' = Ba$; and (4) $M' = Pb$.

and position of these emission bands changed little in other alkaline earth or lead-containing glasses. Unlike the case of alkali terbium glass, in which the emission band half-bandwidth $\Delta\lambda$ changed appreciably with the alkali and its content, $\Delta\lambda$ changed little with alkaline earth and its concentration in the alkaline earth terbium glass. For example, in the wide concentration range of $M'O$ ($n = 4-16$) the $\Delta\lambda$'s of the ${}^5D_4 \rightarrow {}^7F_5$ emission band in $nM'O \cdot Tb_2O_3 \cdot (n+3)P_2O_5$ glasses were 10.8 ± 0.2 nm, 10.2 ± 0.1 nm, 10.2 ± 0.1 nm and 10.0 ± 0.2 nm for $M' = Mg, Ca, Sr,$ and Ba , respectively. Fig. 23 also shows the excitation spectra for Tb^{3+} emission monitored at 544 nm in the $4M'O \cdot Tb_2O_3 \cdot 7P_2O_5$ glasses of Fig. 22. As in the case of alkali yttrium terbium glass, the excitation spectrum consists of the narrow 4f-4f bands in the wavelength range from 280 nm to 400 nm, and the broad bands due to the 4f-5d transition at shorter wavelengths. The strongest band at 220 ± 2 nm is due to the ${}^7F \rightarrow {}^7D$ spin-allowed transition; a weaker band at 250 ± 3 nm is due to the ${}^7F \rightarrow {}^9D$ spin-forbidden band.^{33,34} In $4PbO \cdot Tb_2O_3 \cdot 7P_2O_5$ glass, the ${}^7F \rightarrow {}^7D$ band is anomalously weak and appears to form a single broad band combining with the ${}^7F \rightarrow {}^9D$ band.

It is interesting to note that the intensity of the 4f-5d bands changes considerably with alkaline earth species. Particularly, the enhancement of the ${}^7F \rightarrow {}^9D$ band in the Mg-Tb glass is most prominent. The observed enhancement effect is in an opposite direction with respect to the alka-

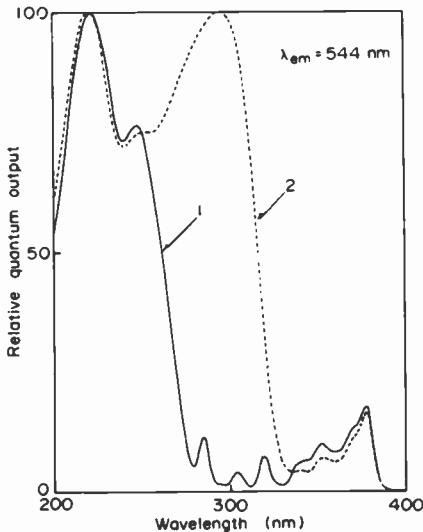


Fig. 24—Excitation spectra of Tb^{3+} emission monitored at 544 nm in (1) $MgO \cdot Tb_2O_3 \cdot 4P_2O_5$ and (2) $MgO \cdot 0.95Tb_2O_3 \cdot 0.05Ce_2O_3 \cdot 4P_2O_5$ glasses.

line earth ionic radius compared to the case of alkali terbium glass.^{30,31} Specifically, in the alkali terbium glass the intensity of the 4f-5d bands increased with the increasing radius of alkali ion, whereas in the alkaline earth terbium glass it increases with decreasing ionic radius of the alkaline earth ion. However, when the data are compared with the structure-sensitive glass transition temperature T_g , one finds that the increase in the intensity of the 4f-5d bands coincides with the increase in T_g in both cases. That is, T_g increases in the order Li, Na, and K in the alkali terbium glass and in the order Ba, Sr, Ca, and Mg in the alkaline earth terbium glass.³⁵ Since the rearrangement of the glass structure is accelerated above T_g , some breaking of cross-linked bondings should occur at T_g . A higher T_g implies stronger network modifier-oxygen bondings. Therefore, the intensity of 4f-5d bands, particularly that of the spin-forbidden $^7F \rightarrow ^9D$ band, must be closely related to the bonding strength of M-O or M'-O, and consequently to that of the Tb-O bonds in the glass.

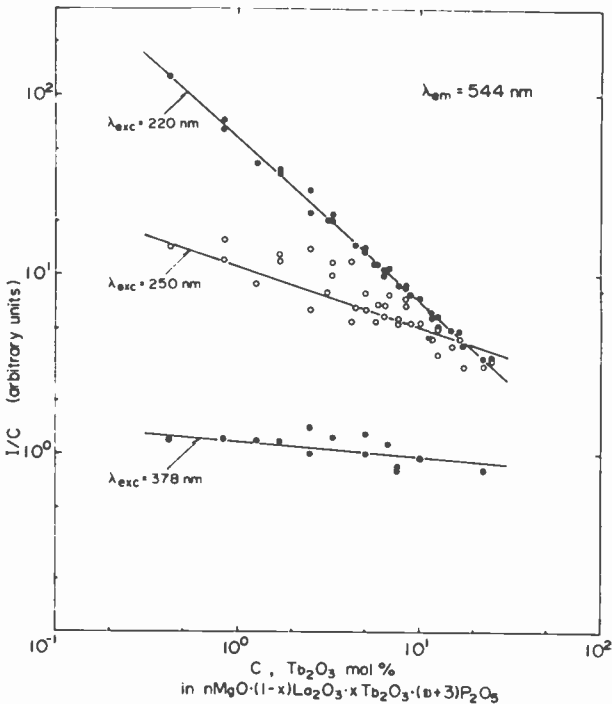


Fig. 25—Concentration dependence curves of normalized intensity of Tb^{3+} emission at 544 nm under excitation at 220 nm (5d), 250 nm (5d), and 378 nm (4f) in $nMgO \cdot (1-x)La_2O_3 \cdot xTb_2O_3 \cdot (n+3)P_2O_5$ glasses.

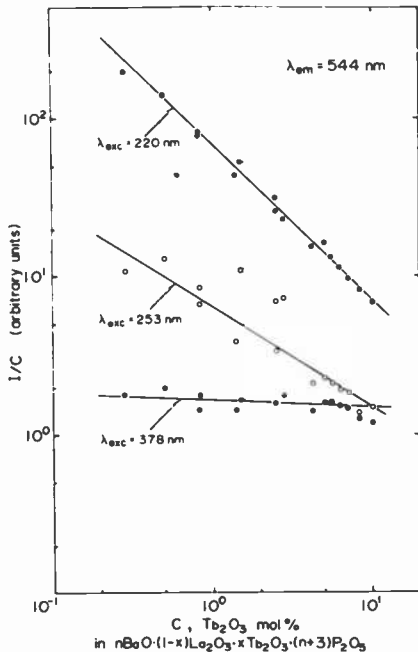


Fig. 26—Concentration dependence curves of normalized intensity of Tb^{3+} emission at 544 nm under excitation at 220 nm (5d), 253 nm (5d), and 378 nm (4f) in $n\text{BaO} \cdot (1-x)\text{La}_2\text{O}_3 \cdot x\text{Tb}_2\text{O}_3 \cdot (n+3)\text{P}_2\text{O}_5$ glasses.

Ce-coactivation resulted in sensitization of Tb^{3+} emission in the alkaline earth terbium glass as in other glasses.^{30,31,36} Fig. 24 shows the excitation spectra for Tb^{3+} emission in $\text{MgO} \cdot \text{Tb}_2\text{O}_3 \cdot 4\text{P}_2\text{O}_5$ and $\text{MgO} \cdot 0.95\text{Tb}_2\text{O}_3 \cdot 0.05\text{Ce}_2\text{O}_3 \cdot 4\text{P}_2\text{O}_5$ glasses. The enhancement of Tb^{3+} emission due to the energy transfer from the Ce^{3+} 5d states to the $^5\text{D}_4$ state of Tb^{3+} is evident.

Concentration dependence of Tb^{3+} emission was investigated in $n\text{MgO} \cdot (1-x)\text{La}_2\text{O}_3 \cdot x\text{Tb}_2\text{O}_3 \cdot (n+3)\text{P}_2\text{O}_5$ and $n\text{BaO} \cdot (1-x)\text{La}_2\text{O}_3 \cdot x\text{Tb}_2\text{O}_3 \cdot (n+3)\text{P}_2\text{O}_5$ glasses. Logarithmic plots of normalized intensity, I/C versus C , where C is mol% Tb_2O_3 , are shown in Figs. 25 and 26. As in the case of Eu-activated glasses, I/C follows the relation

$$I/C = K/C^n,$$

where the exponent n becomes smaller as the absorption of exciting radiation becomes smaller. This exponent ranges from $n \sim 1$ for the $^7\text{F} \rightarrow ^7\text{D}$ excitation to $n \sim 0$ for the 4f-4f excitation at 378 nm. Molar absorption coefficients are estimated to be $10^2 \sim 10^3$ for the spin-allowed transition $^7\text{F} \rightarrow ^7\text{D}$, $1 \sim 10^2$ for the spin-forbidden transition $^7\text{F} \rightarrow ^9\text{D}$,

and $10^{-1} \sim 1$ for the 4f-4f transitions.^{33,37} Despite the difference in the optical transitions involved, concentration quenching of Tb^{3+} emission is quite similar to that of Eu^{3+} emission in the metaphosphate glass. As was pointed out in the preceding section, a model that takes into account quenching interactions of activators at the surface seems to be needed to interpret the present results.

However, one could also say that considerable concentration quenching exists for the 5d-band excitation, whereas no quenching exists for the 4f band excitation. If the data of Figs. 25 and 26 are interpreted in this way, then a model that assumes the existence of concentration-dependent quenching interactions at the 5d states might explain the results. Details of such a quenching model are presented elsewhere.³⁸

It should also be pointed out that the absorption coefficient might change with the Tb concentration due to overlapping of the 4f and 5d electron wave functions of neighboring Tb^{3+} ions.³⁹ However, it was recently demonstrated that such a change was negligible for the Nd^{3+} transitions in $\text{Nd}_x\text{La}_{1-x}\text{P}_5\text{O}_{14}$.⁴⁰ Moreover, the effect of change in absorption coefficient on emission intensity should be larger for the exciting radiation of a smaller absorption coefficient. This prediction is inconsistent with our experimental results.

4. Summary

Fluorescent and optical properties of alkali and alkaline earth rare-earth metaphosphate glasses activated with Ag, Tl, Ce, Sm, Eu, Gd, Tb or Tm were reported and discussed.

In the Ag-activated glass, three emission bands were observed in the wavelength range from 250 to 450 nm. In interpreting this observation, the presence of Ag^+ ions and Ag neutral atom centers was inferred.

The Tl^+ emission band shifted to longer wavelengths with increasing Tl concentration in the Tl-activated glass. The Tl^+ emission band was resolved into two bands with peaks near 280 ± 5 nm and 340 ± 5 nm in Li-Tl-Y and Mg-Tl-Y glasses. The intensity of the high energy band decreased and that of the low energy band increased with increasing Tl concentration in these glasses. From these results, the high energy band was attributed to Tl^+ monomer centers, and the low energy band to Tl^+ - Tl^+ dimer and Tl^+ aggregate centers. Concentration dependence of Tl^+ emission in other glasses was explained similarly by assuming the presence of two overlapped emission bands.

Strong enhancement of Gd^{3+} emission was observed in the Tl-Gd coactivated glass. The energy transfer from the $^3\text{P}_1$ state of Tl^+ to the $^6\text{P}_{7/2}$ state of Gd^{3+} was responsible for the enhancement. In Tl-Y-Gd

glasses, however, the energy transfer was completely suppressed, presumably due to quenching interactions in Tl^+ higher aggregates.

Fluorescent properties of the Tm-activated glass were quite similar to those of Tm-doped sodium phosphate glass and were little influenced by the network modifier in the glass. The half-bandwidth of the $^1D_4 \rightarrow ^3H_4$ emission at 452 nm was about 1/6 of that reported for the sodium phosphate glass.

The excitation spectrum of Ce-activated glass showed four peaks in the wavelength range from 200 to 400 nm. These peaks arose from the splitting of the 5d orbitals of Ce^{3+} and their positions coincided with those of the Ce^{3+} absorption bands in sodium phosphate glass. The intensities of these bands were appreciably changed by the network modifier in the glass.

Considerable concentration quenching was observed in the Sm-activated glass. The quenching behavior of Sm^{3+} emission was unchanged with exciting wavelength. From logarithmic plots of normalized intensities versus concentration, dipole-dipole interaction was deduced as a possible quenching mechanism.

On the other hand, much weaker concentration quenching was observed in the Eu and Tb-activated glasses. Concentration dependence of Eu^{3+} or Tb^{3+} emission was approximated by the relation, $I/C = K/C^n$, where C is the activator concentration and K is a constant. The exponent n changed with the exciting wavelength and became smaller for the radiation of a smaller absorption coefficient. That is, quenching was more pronounced for the exciting radiation of a large absorption coefficient, e.g., larger for the charge transfer band for Eu^{3+} and the f-d transition bands for Tb^{3+} than for the 4f-4f transition bands. It has been suggested that a model that takes into account quenching interactions of activators at the surface might be necessary to explain the observed results.

The intensity of f-d bands, particularly that of the spin forbidden band, of Tb^{3+} emission was considerably influenced by the network modifier in the glass. Potassium and magnesium have the highest intensity in alkali and alkaline earth terbium glasses, respectively. A correlation was found between the f-d band intensity and the glass transition temperature T_g of these glasses.

Acknowledgments

The authors wish to thank E. O. Johnson for continuous encouragement and useful suggestions throughout the course of this work. They also wish to thank F. Okamoto for critical reading of the manuscript.

References:

- ¹H. G. Danielmeyer and H. P. Weber, "Fluorescence in Neodymium Ultraphosphate," *IEEE J. Quantum Electron.*, **QE-8**, p. 805 (1972).
- ²H. Y-P. Hong, "The Crystal Structure of Ytterbium Metaphosphate, YbP_3O_9 ," *Acta Cryst.*, **B30**, p. 1857 (1974).
- ³T. Yamada, K. Otsuka, and J. Nakano, "Fluorescence in Lithium Neodymium Ultraphosphate Single Crystals," *J. Appl. Phys.*, **45**, p. 5096 (1974).
- ⁴H. Y-P. Hong, "Crystal Structure of Potassium Neodymium Metaphosphate, $\text{KNdP}_4\text{O}_{12}$, a New Acentric Laser Material," *Mat. Res. Bull.*, **10**, p. 1105 (1975).
- ⁵T. Tsujimoto, Y. Fukuda and M. Fukai, "Preparation and Fluorescent Properties of Lithium Rare Earth Phosphate Phosphors," *J. Electrochem. Soc.*, **124**, p. 553 (1977).
- ⁶K. R. Albrand, R. Attig, J. Fenner, J. P. Jeser and D. Mootz, "Crystal Structure of the Laser Material $\text{NdP}_5\text{O}_{14}$," *Mat. Res. Bull.*, **9**, p. 129 (1974).
- ⁷H. Y-P. Hong and J. W. Pierce, "Crystal Structure of Ytterbium Ultraphosphate, $\text{YbP}_5\text{O}_{14}$," *Mat. Res. Bull.*, **9**, p. 179 (1974).
- ⁸H. Y-P. Hong, "Crystal Structures of Neodymium Metaphosphate (NdP_3O_9) and Ultraphosphate ($\text{NdP}_5\text{O}_{14}$)," *Acta Cryst.*, **B30**, p. 468 (1974).
- ⁹A. E. R. Westman, "Constitution of Phosphate Glasses," in *Modern Aspects of the Vitreous State*, ed. by J. D. Mackenzie, Vol. 1, pp. 63-91, Butterworths, London (1960).
- ¹⁰Y. Abe, "Kinetic Studies on Crystallization of Calcium Metaphosphate Glass," *Yogyo Kyokai Shi*, **81**, p. 471 (1973).
- ¹¹W. A. Weyl, *Coloured Glasses*, pp. 459-462, Society of Glass Technology, Sheffield, G. B. (1951).
- ¹²A. K. Ghosh, "Optical Spectra of Thallium in Glasses as Related to Crystals and Solutions," *J. Chem. Phys.*, **44**, p. 535 (1966).
- ¹³J. A. Duffy and M. D. Ingram, "Establishment of an Optical Scale for Lewis Basicity in Inorganic Oxyacids, Molten Salts, and Glasses," *J. Amer. Chem. Soc.*, **93**, p. 6448 (1971).
- ¹⁴S. Parke and R. S. Webb, "The Optical Properties of Thallium, Lead and Bismuth in Oxide Glasses," *J. Phys. Chem. Solids*, **34**, p. 85 (1973).
- ¹⁵T. Takahashi, "Concentration Dependent Luminescence of Tl^+ in Alkali Yttrium Metaphosphate Glasses," *J. Phys. Chem. Glasses* (to be published).
- ¹⁶R. Reisfeld, E. Greenberg, R. Velapold and B. Barnett, "Luminescence of Quantum Efficiency of Gd and Tb in Borate Glasses and the Mechanism of Energy Transfer Between Them," *J. Chem. Phys.*, **56**, p. 1698 (1972).
- ¹⁷R. Reisfeld and Sh. Morag, "Energy Transfer from Tl^+ to Gd^{3+} in Inorganic Glasses," *Appl. Phys. Lett.*, **21**, p. 57 (1972).
- ¹⁸R. Reisfeld and Y. Eckstein, "Absorption and Emission Spectra of Thulium and Erbium in Borate and Phosphate Glasses," *J. Solid State Chem.*, **5**, p. 174 (1972).
- ¹⁹E. Nakazawa, "4f-5d and Charge Transfer Transitions in Rare Earth Orthophosphate Phosphors," *Proc. 167th Symp. Phosphor Res.*, pp. 19-26 July 15, 1977 (in Japanese).
- ²⁰R. Reisfeld, "Spectra and Energy Transfer of Rare Earths in Inorganic Glasses," *Structure and Bonding*, Vol. 13, pp. 53-98, Springer-Verlag, Berlin/Heidelberg/New York (1973).
- ²¹R. Reisfeld and L. Boehm, "Energy Transfer between Samarium and Europium in Phosphate Glasses," *J. Solid State Chem.*, **4**, p. 417 (1972).
- ²²L. Ozawa, "Determination of Self-Concentration Quenching Mechanisms of Rare Earth Luminescence from Intensity Measurements on Powdered Phosphor Screens," *J. Electrochem. Soc.*, **126**, p. 106 (1979).
- ²³L. G. Van Uitert, *Luminescence of Inorganic Solids*, ed., P. Goldberg, pp. 489-96, Academic Press, New York (1966).
- ²⁴L. G. Van Uitert and S. Iida, "Quenching Interactions between Rare Earth Ions," *J. Chem. Phys.*, **37**, p. 986 (1962).
- ²⁵L. G. Van Uitert, "Characterization of Energy Transfer Interactions between Rare Earth Ions," *J. Electrochem. Soc.*, **114**, p. 1048 (1967).
- ²⁶R. Reisfeld, R. A. Velapoldi, L. Boehm, and M. Ish-Shalom, "Transition Probabilities of Europium in Phosphate Glasses," *J. Phys. Chem.*, **75**, p. 3980 (1971).
- ²⁷R. Reisfeld, R. A. Velapoldi, and L. Boehm, "Quantum Efficiencies and Radiationless Transitions of Europium (III) in Phosphate Glasses," *J. Phys. Chem.*, **76**, p. 1293 (1972).
- ²⁸A. Lempicki, H. Samelson, and C. Brecher, "Europium Chelates as Laser Materials," *Proc. 4th Conf. Rare Earth Res.*, ed., L. Eyring, pp. 351-61, Gordon and Breach, New York (1965).

- ²⁹J. M. Flaherty and R. C. Powell, "Concentration Quenching in $\text{Nd}_x\text{Y}_{1-x}\text{P}_5\text{O}_{14}$ Crystals," *Phys. Rev. B*, **19**, p. 32 (1979).
- ³⁰T. Takahashi and O. Yamada, "Luminescence of Terbium-Activated Alkali Rare Earth Metaphosphate Glasses," *J. Electrochem. Soc.*, in press.
- ³¹T. Takahashi, H. Fujita and O. Yamada, "Luminescence of Terbium-Activated Alkali Metaphosphate Glasses," *Proc. 176th Symp. Phosphor Res.*, pp. 7-16, July 13, 1979 (in Japanese).
- ³²E. Kordes and R. Nieder, "Die Ultraviolett-Durchlässigkeit binärer Phosphatgläser," *Glastech. Ber.*, **2**, p. 41 (1968).
- ³³J. L. Ryan and C. K. Jørgensen, "Absorption Spectra of Octahedral Lanthanide Hexahalides," *J. Phys. Chem.*, **70**, p. 2845 (1966).
- ³⁴T. Hoshina, "4f-5d Excitation Energy of Tb^{3+} in Solids," *J. Chem. Phys.*, **50**, p. 5158 (1969).
- ³⁵T. Takahashi and O. Yamada, "Thermal Properties of New Metaphosphate Glasses," *RCA Review*, **41**, p. 120, March 1980 (this issue).
- ³⁶S. Shionoya and E. Nakazawa, "Sensitization of Tb^{3+} Luminescence by Ce^{3+} and Cu^+ in Glasses," *Appl. Phys. Letters*, **6**, p. 118 (1965).
- ³⁷W. T. Carnall, P. R. Fields, and K. Rajnak, "Electronic Energy Levels of the Trivalent Lanthanide Aquo Ions. III. Tb^{3+} ," *J. Chem. Phys.*, **49**, p. 4447 (1968).
- ³⁸H. Fujita and M. Inoue, "Concentration Quenching of Luminescence in a Disordered System With Dipolar Interaction," *RCA Review*, **41**, p. 92, March 1980 (this issue).
- ³⁹H. G. Danielmeyer, "Efficiency and Fluorescence Quenching of Stoichiometric Rare Earth Laser Materials," *J. Luminescence*, **12/13**, p. 179 (1976).
- ⁴⁰F. Auzel, "Oscillator Strengths of Nd^{3+} in $\text{Nd}_x\text{La}_{1-x}\text{P}_5\text{O}_{14}$ and Concentration Quenching in Stoichiometric Rare-Earth Laser Materials," *IEEE J. Quantum Electron.*, **QE-12**, p. 258 (1976).

Concentration Quenching of Luminescence in a Disordered System with Dipolar Interaction

H. Fujita and M. Inoue

RCA Research Laboratories, Inc., Machida City, Tokyo, Japan

Abstract—In Part I, experimental results are presented for photoluminescence of terbium-activated sodium rare-earth metaphosphate glass. Photoluminescence yield and decay time of Tb-activated sodium rare-earth metaphosphate glass were measured over the wide range of terbium concentrations, 10^{19} to 10^{21} ions/cc. Over this range we observed a large change, a hundredfold, in the uv-excited photoluminescent yield. The luminescence decay curve was of the simple exponential type. This suggests a single ion process during decay. The decay time constant, typically 2.5×10^{-3} seconds, was relatively independent of the terbium concentration.

In Part II, concentration quenching due to migration decay in a dipole-coupled random system was studied using Anderson's probabilistic approach. Migration decay time was evaluated in terms of the dipolar coupling constant, the inhomogeneous level width of donors, and the concentrations of the donors and acceptors. The effect of the inhomogeneous width is shown to be much more significant in reducing the migration decay in the Anderson model than in the phenomenological diffusion model. The result is applied to explain the observed anomalous concentration quenching of 2550 Å excitation of Tb^{3+} in a phosphate glass.

Part I. Experiment

1.1 Introduction

Rare earth compounds are an important subject of study in luminescence physics.¹ Applications interest is often concerned with obtaining materials having high luminescence yield. As is well known, these yields increase with increasing rare-earth concentration up to about 10^{19} cm⁻³.

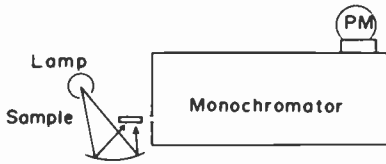


Fig. 1—Schematic layout of instruments for measurement of uv-excited photoluminescence.

Beyond this concentration region, the luminescent efficiency decreases because of concentration quenching. The results reported in this paper are accordingly of particular interest, since they show that, with Tb-metaphosphate glass, concentration quenching does not occur until the terbium concentration reaches 10^{21} cm^{-3} .

The molecular formula of the glass is $2(\text{Na}_2\text{O}\cdot\text{P}_2\text{O}_5)(1-x)\text{Y}_2\text{O}_3\cdot x\text{Tb}_2\text{O}_3\cdot 3\text{P}_2\text{O}_5$. The variable x represents the Tb-concentration. The molecular formula is abridged as $\text{Na}_2\text{Tb}_x\text{Y}_{1-x}\text{P}$. In our studies the variable x has the values 0.02, 0.1, 0.3, 0.5, 0.7, and 1.0 corresponding to Tb concentrations of 6.8×10^{19} , 3.4×10^{20} , 9.8×10^{20} , 1.6×10^{21} , 2.2×10^{21} , and $3.0 \times 10^{21} \text{ cm}^{-3}$, respectively.

1.2 Experimental Procedure

The luminescence spectrum is measured with a JASCO-100 monochromator having a deuterium lamp uv light source as shown schematically in Fig. 1. Photon counting is used to detect the luminescence. The excitation spectrum for a specific wavelength emission (typically for ${}^5\text{D}_4 - {}^7\text{F}_j$ emission at 5430 \AA) is measured by using two monochromators as shown in Fig. 2. In Fig. 2, the wavelength dial of the small monochromator is fixed at the detection wavelength, while the other monochromator (JASCO-100) is used to scan the excitation wavelength.

Decay time measurements are performed with a pulse-operated deuterium lamp and a small monochromator. The lamp is pulse-operated

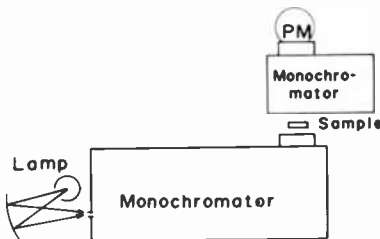


Fig. 2—Schematic layout of instruments for measurement of the excitation spectrum of the photoluminescence.

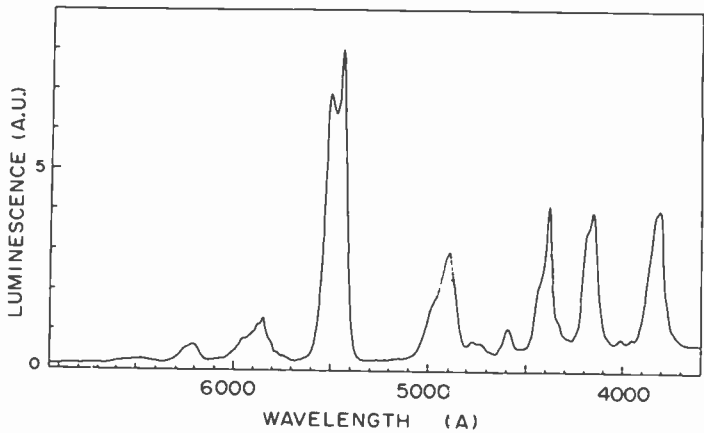


Fig. 3—Luminescence spectrum of a $6.8 \times 10^{19} \text{ cm}^{-3}$ Tb-concentration sample.

once per second, and the decay signals are averaged over 1024 signal samples with a transient converter and a signal averager.

1.3 Experimental Results and Discussion

Fig. 3 shows the luminescence spectrum obtained from a $6.8 \times 10^{19} \text{ cm}^{-3}$ Tb-concentration sample excited by uv light. The spectrum consists of two series of emissions; a ${}^5\text{D}_3 - {}^7\text{F}_j$ series covering 3600 to 4500 Å, and a ${}^5\text{D}_4 - {}^7\text{F}_j$ series covering 4800 to 6300 Å. The luminescence spectrum shows a strong Tb concentration dependence, and the blue emission component in the 3600 to 4500 Å region disappears when the Tb-concentration is increased from $6.8 \times 10^{19} \text{ cm}^{-3}$ to $9.8 \times 10^{20} \text{ cm}^{-3}$.

Fig. 4 shows the excitation spectra for 5430 Å emission (${}^5\text{D}_4 - {}^7\text{F}_j$ transition) for different Tb-concentrations. In Fig. 4, there is a structure

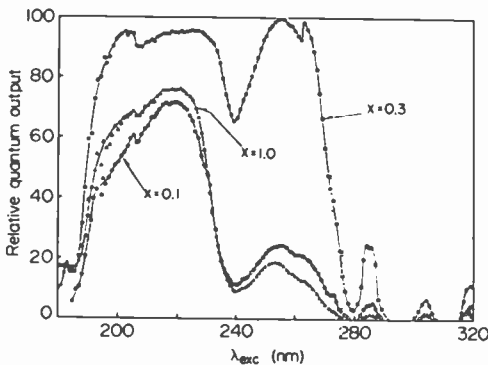


Fig. 4—Excitation spectra for ${}^5\text{D}_4 - {}^7\text{F}_j$ (5430 Å) luminescence.

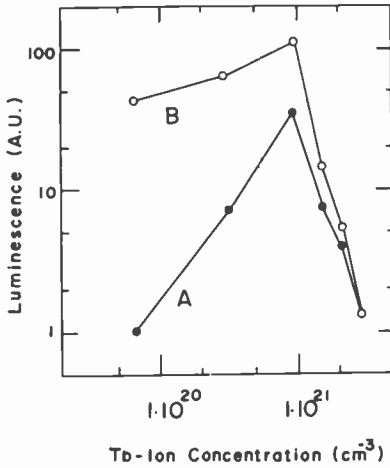


Fig. 5—Tb-concentration dependence of photoluminescence yield. Curve A shows the luminescence intensity and curve B the luminescence yield per Tb ion.

at 2550 Å that depends strongly on the Tb concentration. The structure near 2550 Å is thought to be due to the f-d transition of Tb ions.

Fig. 5 shows the Tb concentration dependence of 5430 Å luminescence ($^5D_4 - ^7F_J$ transition) excited by 2550 Å uv light. The luminescence intensity shows strong Tb concentration dependence as shown by curve A. Curve B in Fig. 5 is the luminescence yield per ion. One possible explanation for the strong Tb concentration dependence involves the possibility of having Tb-ion pairs in the octahedral sites for Tb ions.² Another possibility involves Anderson's energy migration theory.³

Fig. 6 shows a typical decay curve of the luminescence measured by

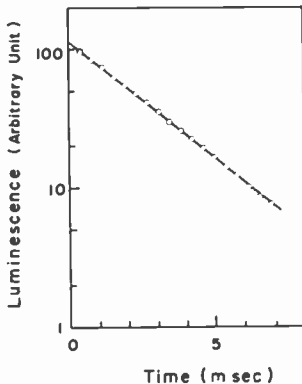


Fig. 6—Decay curve of the photoluminescence excited by a pulsed uv light.

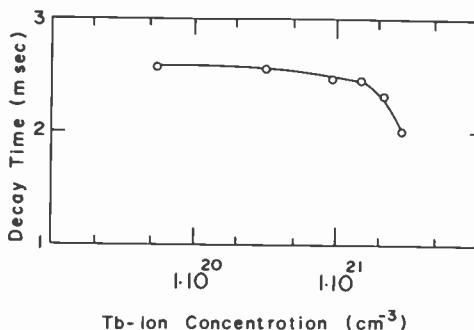


Fig. 7—Tb-concentration dependence of the photoluminescence decay time.

using the pulsed light source. The decay curves are purely exponential and no deviation from the exponential decay is observed. The possibility of a bimolecular decay process is thereby excluded; the decay process is taking place solely within the excited ion.

Fig. 7 shows the Tb concentration dependence of the decay time. As can be seen, the concentration dependence is small. The decay time constant is typically about 2.5×10^{-3} sec. The reason for the decrease of the luminescence yield shown in Fig. 5 cannot be due to the luminescence decay phenomena, since the Tb concentration dependence of the decay time is so small. On the other hand, the luminescence yield decreases about a hundred-fold from the $9.8 \times 10^{20} \text{ cm}^{-3}$ sample to the $3.0 \times 10^{21} \text{ cm}^{-3}$ sample.

Acknowledgments

The author expresses his sincere thanks to Dr. T. Takahashi for providing the Tb-glass samples, and to Mr. E. O. Johnson for editing the manuscript.

References:

- ¹ M. Bancie-Grillot, Proc. 1975 International Conf. on Luminescence, Tokyo, p. 681.
- ² L. G. Van Uitert and L. F. Johnson, "Energy Transfer Between Rare-Earth Ions," *J. Chem. Phys.*, **44**, p. 3514, 1 May 1966.
- ³ M. Inoue, private communication.

Part II. Theory

2.1 Introduction

The reduction of luminescence yield with the increase of donor concentration is called concentration quenching. This is an important

problem in the development of efficient phosphors or laser materials. Quenching results from the nonradiative decay of the donor excitation either by direct transfer or by migration among the donors to energy sinks.¹ The migration mechanism is dominant in a system having a donor concentration sufficiently larger than that of the energy sinks. Concentration quenching is experimentally observed in materials that have some degree of disorder. A theoretical model explaining the experiment results in terms of exciton diffusion must take account of the disorder nature of the system characterized by random distributions of such quantities as donor sites, site energies, and the transfer integral.

Anderson used the probabilistic approach to develop a theory of diffusion in the random system.² His treatment centers on the question of localization, which has been treated extensively in the context of metal-nonmetal transitions.³ The approach was originally aimed to describe migration decay in the dipolar coupled spin system considered by Portis.⁴ However, it has not been widely applied to the problem of migration decay in actual systems, except for the exchange-coupled system of ruby where particular attention was given to the critical concentration and the mobility edge.⁵

The present paper shows that Anderson's theory gives a reasonable explanation of concentration quenching in a dipolar-coupled system with random distributions of site and site energies. Anderson's argument on the diffusion rate is summarized in Sec. 2.2. The average migration life time of an exciton in our system is estimated (Sec. 2.3) using a model based on Anderson's arguments and the result of random walks in a system with traps. The results are applicable in explaining observed anomalous behavior of concentration quenching of Tb^{3+} in a phosphate glass^{6,7} (Sec. 2.4).

According to Anderson's argument, the migration of an exciton always occurs in a disordered system having a transfer integral that decreases inversely as the third power of distance, or slower. Concentration quenching in such a system is important in the range of concentration for which the average migration life time becomes comparable with, or shorter than, the intrinsic life time of the single donor excitation. The case of the $f \rightarrow d$ transition of Tb^{3+} at 2550 Å in a phosphate glass is shown in the present paper to be a unique example. Here the quenching effect appears at fairly high concentrations of donors because of the large dipolar coupling, the large inhomogeneous width of the excitation energy, and the short intrinsic life time of Tb^{3+} . The results on this obtained with Anderson's theory are compared in Sec. 2.5 with those predicted from simple second order perturbation theory.

2.2 Summary of Anderson's Theory

This section summarizes Anderson's arguments used in calculating the transport rate of a particle or an exciton in a random system.^{2,8}

A Frenkel exciton in the random lattice is described by the one-particle Hamiltonian H . Assuming one level for each atom, the diagonal and the off-diagonal elements of H are given in the tight-binding representation

$$\langle j|H|l\rangle = \epsilon_j \delta_{jl} + V_{jl}, \quad [1]$$

where $|l\rangle$ is the localized state matrix at the l th site, ϵ_j is the excitation energy, and V_{jl} is the transfer matrix element between the j th and l th sites. Consider the case in which ϵ_j and V_{jl} are stochastic variables reflecting the structural disorder of the system. The excitation energy ϵ_j is inhomogeneously broadened with the distribution $P(\epsilon)$, because the local field varies from site to site. The transfer integral V_{jl} is random because V_{jl} depends on the distance between the two sites which are distributed randomly in space. The inhomogeneous distribution of the coupling constant in V_{jl} is neglected for simplicity.

The Schrödinger equation can be written

$$i\dot{a}_j(t) = \epsilon_j a_j(t) + \sum_{l \neq j} V_{jl} a_l(t), \quad [2]$$

where $a_j(t)$ is the probability amplitude that an exciton is on the j th site at time t . Eq. [2] is solved with the initial conditions $a_0(0) = 1$ and $a_j(0) = 0$, for $j \neq 0$, that is, an exciton is considered to be created initially on the 0th site. Now introduce the Laplace transform of $a_j(t)$,

$$f_j(s) = \int_0^\infty a_j(t) e^{-st} dt. \quad [3]$$

Eq. [2] then becomes

$$isf_j - \epsilon_j f_j - \sum_{l \neq j} V_{jl} f_l = i\delta_{j0}. \quad [4]$$

The solution for $f_0(s)$ is

$$f_0(s) = \frac{i}{is - \epsilon_0 - \Delta_0(s)}, \quad [5]$$

where

$$\Delta_0(s) = \sum_j' \left[\frac{V_{0j} V_{j0}}{is - \epsilon_j} + \sum_k' \frac{V_{0j} V_{jk} V_{k0}}{(is - \epsilon_j)(is - \epsilon_k)} + \dots \right], \quad [6]$$

and Σ' denotes the exclusion of the diagonal term in the summation.

The Laplace transform $f_j(s)$ for $s = \sigma - iE$ is equivalent with the one-particle Green function

$$G_{j0}(E + i\sigma) = \langle j | (E + i\sigma - H)^{-1} | 0 \rangle = -if_j(\sigma - iE). \quad [7]$$

Correspondingly, $\Delta_0(\sigma - iE)$ is the self energy of the site diagonal Green function $G_{00}(E + i\sigma)$. From the definition of the time-dependent Green function, $|G_{j0}(t)|^2$ is the probability that the particle initially at the 0th site is found at the j th site after the time interval t . The transport properties of the particle therefore are to be obtained by examining $|G_{j0}(t)|^2$. Instead of $G_{j0}(t)$, Anderson considered the diagonal Green function $G_{00}(t)$ which is equivalent to $\Delta_0(\sigma - iE)$. Since the self energy contains the stochastic variables ϵ_j and V_{jl} , $\Delta_0(s)$ itself is a stochastic variable that must be studied in a probabilistic manner. According to Anderson, the eigen function is localized if the imaginary part of the self energy $\text{Im}\Delta_0(s)$ is zero with unity probability in the limit where the real part of s , $\text{Re}s$, approaches zero. Instead, if $\text{Im}\Delta_0(s)$ is finite in the limit of $\text{Re}s \rightarrow 0$ with unity probability, the wave function is so extended that the exciton (or the particle) can migrate through the lattice. It is in this sense that the random system, with interaction decaying with distance as r^{-3} , or slower, always gives rise to exciton transport.

Next consider how the rate of exciton transport can be estimated for a system having the extended states. Restrict attention to the amplitudes of an exciton at the 0th site $a_0(t, E)$ for a particular value of energy,

$$\bar{E}_0 = -\text{Im}s = \epsilon_0 + \text{Re}\Delta_0(\sigma - i\bar{E}_0), \quad [8]$$

which holds in the probabilistic sense as previously noted. The Laplace transform is

$$\begin{aligned} f_0(\sigma, \bar{E}_0) &= \frac{i}{i\sigma - i\text{Im}\Delta_0(\sigma, \bar{E}_0)} \\ &= \int_0^\infty a_0(t, \bar{E}_0) e^{-\sigma t} dt, \end{aligned} \quad [9]$$

with a positive real number σ . The last quantity is equal to $\sigma^{-1} \langle a_0(\sigma^{-1} \bar{E}_0) \rangle_{av}$, where $\langle a_0(\sigma^{-1} \bar{E}_0) \rangle_{av}$ is the average of $a_0(t, \bar{E}_0)$ over the time interval σ^{-1} . If the exciton is initially on the 0th site with $a_0(0, \bar{E}_0) = 1$, the decay time of this state is defined by the time interval after which the amplitude is decreased by a factor u . This is given by the roots of the equation,

$$\langle a_0(\tau_d, \bar{E}_0) \rangle_{av} = \tau_d^{-1} f_0(\tau_d^{-1}, \bar{E}_0) = u^{-1}. \quad [10]$$

Here u is a numerical constant of order unity. For example, τ_d is the half decay time for $u = 2$, and is the e^{-1} -decay time for $u = e$. Relation [10], containing the stochastic variable Δ_0 , must be treated in the probabilistic

sense. Anderson approximately solved Rel. [10] by finding the probability distribution of $\text{Im } \Delta_0$ and then replacing $\text{Im } \Delta_0$ with the most probable value.

2.3 Migration Life Time

Consider the migration life time of a Frenkel exciton in a dipolar-coupled random lattice that contains energy sinks. A rigorous treatment of this problem is done in terms of the Green function of such a system. However, instead of trying to solve such a complicated problem, consider a model based on Anderson's arguments combined with a random walk system containing sinks. It is assumed that the energy sinks exist at a very small fraction of the donor sites, and that the exciton energy is quenched very efficiently once it reaches the sink. It is also assumed that the intrinsic life time of a Frenkel exciton is enough longer than a single step time that the exciton can visit many sites before being trapped by a sink. Under the above conditions the average migration life time of an exciton is defined by

$$\tau_m = \bar{t} s_r^{-1}, \quad [11]$$

where \bar{t} is the average number of exciton hop steps starting from an arbitrary site of the lattice, and s_r is the hopping rate of a single step.

Montroll made a rigorous calculation of the average number of steps for the random walks having nearest neighbor steps in a finite periodic lattice containing energy traps. For a 3-D lattice, his result is expressed by the leading term

$$\bar{t} = k_3/n_a, \quad [12]$$

where n_a is the number ratio of the traps to the donors, and k_3 is a numerical factor of order unity which depends upon the lattice structure. Similar calculations were made for the case with very long steps having equal probability regardless of step length. The average step number is given by¹⁰

$$\bar{t} = 1/n_a. \quad [13]$$

Although there is no interpolation formula for a case between the above two extremes it is not unreasonable to assume that the average step number is approximately equal to n_a^{-1} for the present case of dipolar interaction.

The single jump rate s_r in Eq. [11] is approximated by the one for the random system we obtain using Anderson's theory for a system having no energy sinks. For the case of dipolar interaction, the single jump rate is calculated by retaining the first term of the perturbation in $\Delta_0(s)$ (Eq. [6]) and by assuming specific distribution functions for site and site

energy. The transfer integral is

$$V_{jl} = \frac{A}{r_{jl}^3}, \quad (14)$$

where A is the coupling constant, either electric or magnetic dipole-dipole as the case may be, and r_{jl} is the distance between the j th and l th sites. The imaginary part of the first term of $\Delta_0(s)$ is

$$\text{Im}\Delta_0(\sigma - iE) = -\sigma \sum_l' \frac{A^2}{r_{0l}^6[(E - \epsilon_l)^2 + \sigma^2]} \equiv -\sigma X. \quad (15)$$

The probability distribution $\psi(X)$ of X is calculated by the Markoff-Holtzmark method.¹¹ The Fourier transform of $\psi(X)$ is given by

$$\psi(X) = \frac{1}{2\pi} \int_{-\infty}^{\infty} \phi(k) e^{-ikX} dk, \quad (16)$$

with

$$\phi(k) = \left[\int P(\epsilon) d\epsilon \int R(\mathbf{r}) d\mathbf{r} \exp \left\{ \frac{ikA^2}{r^6[(E - \epsilon)^2 + \sigma^2]} \right\} \right]^N, \quad (17)$$

where N is the total number of lattice sites, $P(\epsilon)$ is the distribution function of the site energy, and $R(\mathbf{r})$ is the distribution function of \mathbf{r} . The distribution of A is neglected for simplicity. Assume a perfectly random distribution for \mathbf{r} , i.e., $R(\mathbf{r})d\mathbf{r} = 3d\mathbf{r}/(4\pi R^3)$. In the limit of $R \rightarrow \infty$ and $N \rightarrow \infty$, such that the number density $n = 3N/(4\pi R^3)$ is finite, Eq. [17] is calculated to be

$$\phi(k) = \exp \left[-Q \left(\frac{k}{i} \right)^{1/2} \right], \quad (18)$$

where

$$Q = \frac{4\pi^{3/2}An}{3} \int \frac{P(\epsilon)d\epsilon}{[(E - \epsilon)^2 + \sigma^2]^{1/2}}. \quad (19)$$

Eq. [16] gives, in turn,

$$\psi(X) = \frac{1}{2} \pi^{-1/2} Q X^{-3/2} \exp \left[- \left(\frac{Q}{2} \right)^2 \frac{1}{X} \right]. \quad (20)$$

The most probable value of X becomes

$$X_{mpv} = (Q^2/6). \quad (21)$$

The transport rate is approximately given by the roots of Eq. [10] when

$\text{Im}\Delta_0(\sigma - iE)$ is replaced with the most probable value $-\sigma X_{mpv}$ at $E = \bar{E}_0$ (Eqn. [8]).

Consider two cases of the site energy distribution function for which the center is taken to be \bar{E}_0 . The first case (i) is for the rectangular distribution:

$$P(\epsilon) = 1/W, \text{ for } \bar{E}_0 - W/2 \leq \epsilon \leq \bar{E}_0 + W/2 \quad [22]$$

$$= 0, \text{ otherwise.}$$

This gives

$$X_{mpv}(\bar{E}_0) = (c_1 An/W)^2 [\sinh^{-1}(W/2\sigma)]^2, \quad [23]$$

and, in turn, the inverse of the half decay time

$$s_r = \tau_d^{-1} = \sigma/\hbar = W/[2\hbar \sinh(W/c_1 An)], \quad [24]$$

with

$$c_1 = (32\pi^3/27)^{1/2}. \quad [25]$$

The second case (ii) is for the Lorentzian distribution:

$$P(\epsilon) = \frac{1}{\pi} \frac{\gamma}{(\bar{E}_0 - \epsilon)^2 + \gamma^2}. \quad [26]$$

This gives

$$X_{mpv}(\bar{E}_0) = (c_2 An/\gamma)^2$$

$$\times \left\{ \cosh^{-1}(\gamma/\sigma) / \sqrt{1 - (\sigma/\gamma)^2} \right\}^2, \quad [27]$$

and the decay rate s_r as a root $s_r = \sigma/\hbar$ of

$$\gamma = \sigma \cosh[(\gamma/c_2 An) \sqrt{1 - (\sigma/\gamma)^2}], \quad [28]$$

with

$$c_2 = 8\pi/3\sqrt{6}. \quad [29]$$

Finally, the average migration life time of an exciton is, from Eqs. [11] and [13],

$$\tau_m = (n_a s_r)^{-1}, \quad [30]$$

where s_r is given by Eqs. [24] and [28] for the rectangular or the Lorentzian distributions of site energy, respectively.

The application of Anderson's model shows that the inhomogeneous width W of the excitation energy plays an important role in determining exciton transport behavior. The migration life time increases rapidly as the inhomogeneous width increases. For instance, τ_m varies with W

as $\exp(W/c_1An)$ for case (i), and with γ as $\exp(\gamma/c_2An)$ for case (ii). In the other extreme of $W = 0$, or $\gamma = 0$, Eqs. [24] and [28] are reduced to a constant,

$$\tau_m = 2h/(n_a c_i An), \quad i = 1, 2. \quad [31]$$

These conclusions are rather insensitive to the distribution function $P(\epsilon)$ because X_{mpv} is evaluated for the energy at the center of the distribution band, that is, taken equal to \bar{E}_v . However, if the energy falls in the tail of the distribution, there will be a quantitative difference in the migration life time depending upon the type of distribution. The approximations used in deriving Eqs. [24] or [28] should be noted. In calculating the single jump rate, only the first term of the perturbation series in the self-energy Δ_0 is retained. In this approximation, we considered only the contribution of the direct transfer between the two sites with the same energy. But there is also a contribution from the indirect transfer between the two sites that occurs through the sequence of virtual transfers among the remaining sites with different energies. This, the tunneling effect,² is completely neglected in our approximation assuming that the direct transfer gives the most important contribution for our system. This indirect contribution can be eliminated by solving the self-energy in a self consistent way using renormalization perturbation theory.¹²

2.4 Application to $\text{Na}_2\text{Tb}_x\text{Y}_{1-x}\text{P}_4\text{O}_{12}$ Glass

The Tb^{3+} ion in a phosphate glass with composition $\text{Na}_2\text{Tb}_x\text{Y}_{1-x}\text{P}_4\text{O}_{12}$ shows a bright green emission centered at about 5500 Å. This arises from ${}^5\text{D}_4 \rightarrow {}^7\text{F}_j$ transitions within the 4f electronic configurations as sketched in Fig. 8. It has been observed experimentally that the green (5420 Å) emission intensity shows strong dependence upon Tb^{3+} concentration when it is excited by ultraviolet (2550 Å) light.^{6,7} On the other hand, the observed life time of the ${}^5\text{D}_4$ levels varies little with the Tb^{3+} concentration, independent of the excitation frequencies.⁷ The 2550 Å level is assigned to the $4f^75d$ level of Tb^{3+} .¹³ The relevant levels of Tb^{3+} in glass can be represented by the three-level system consisting of the ground (${}^7\text{F}_6$), the emitting (${}^5\text{D}_4$), and the excited ($4f^75d$) levels. The population of the three levels are denoted by N_0 , N_1 and N_2 , respectively from the lowest levels (Fig. 8). The rate equations under weak ultraviolet excitation of the system can be written as

$$\begin{aligned} \dot{N}_1 &= W_{12}N_2 - \frac{1}{\tau_1} N_1 \\ \dot{N}_2 &= N_0\sigma_u\Phi - \frac{1}{\tau_2} N_2. \end{aligned} \quad [32]$$

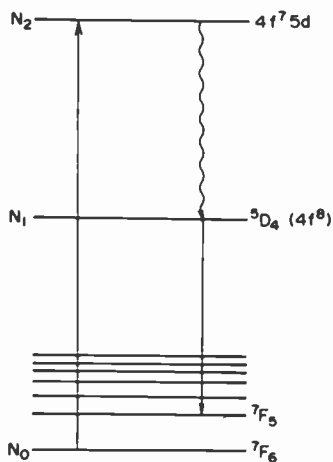


Fig. 8—The three energy levels of Tb³⁺ consisting of the ground (⁷F₆), the emitting (⁵D₄), and the uv excited (4f⁷5d) levels.

Up-conversion from the lower to the upper levels is neglected and, also, cross-relaxation between the two Tb³⁺ ions, which is negligible because of the large energy mismatch among the relevant levels of Tb³⁺. The emission intensity is given by

$$I = \tau_1 \tau_2 W_{12} N_0 W_1 \sigma_u \Phi, \quad [33]$$

where τ_i is the life time of the i th level, W_{ij} is the nonradiative transition rate from the j th to i th levels, W_1 is the radiative decay rate from level 1, σ_u is the uv absorption coefficient, and Φ is the flux of uv light. Concentration dependence of the emission intensity, in Eq. [33] arises from N_0 , the Tb³⁺ concentration, and from the migration decay time of level 2 for the following reasons. In Na₂Tb_xY_{1-x}P₄O₁₂, each Tb³⁺ ion is considered to be surrounded by six oxygen ions to form an isolated octahedron.¹⁴ In the crystalline state, the nearest Tb³⁺ ions are separated by 5–6 Å. This makes the coupling between Tb³⁺ ions generally too weak to hinder migration decay of the excited levels of Tb³⁺ within 4f⁸ configurations. However, for the case of the f → d electric dipole transition the large dipole transfer integral gives an appreciable contribution to the migration decay of the 4f⁷5d level. Thus the life time of level 2, τ_2 , is

$$\tau_2^{-1} = \tau_0^{-1} + \tau_m^{-1}, \quad [34]$$

where τ_0 is the intrinsic life time of the 4f⁷5d level of the single Tb³⁺ ion, and τ_m is the decay time due to exciton migration to energy sinks given by Eq. [30].

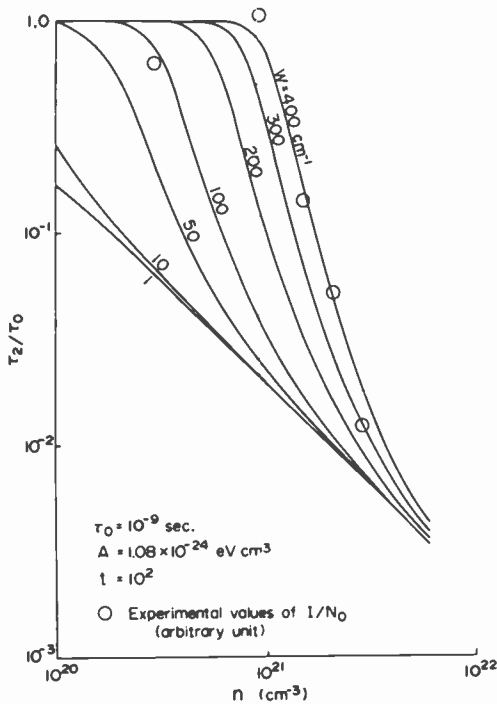


Fig. 9—The normalized life time τ_2/τ_0 plotted as a function of concentration for varying the values of the inhomogeneous width. The experimental values of the emission intensity per ion is represented by solid circles.

The values of parameters involved in τ_2 for the 2550 Å excitation level of Tb^{3+} in a phosphate glass are estimated approximately as follows. The intrinsic life time of the $4f^75d$ level of Tb^{3+} cannot be directly measured since it decays nonradiatively. We assume that τ_0 is much shorter than 10^{-7} sec, the upper limit experimentally determined for Tb^{3+} in YAG.¹⁵ The dipolar coupling constant A is given by

$$A = \sqrt{\frac{2}{3}} \frac{e^2}{n_0^2} |\langle \hat{x}_{02} \rangle|^2, \quad [35]$$

where n_0 is the refractive index, and \hat{x}_{02} is the matrix element of electron position between the ground $4f^8$ level and the excited $4f^75d$ level at 2550 Å. The inhomogeneous width of the 2550 Å line from the observed spectrum⁷ is of the order of 10^2 cm $^{-1}$. The energy sink fraction in the total number of donors is difficult to determine since the nature of the energy sink is not identified for our system. We simply assume that the fraction of the energy sink is of the order of 1%. The values of parameters

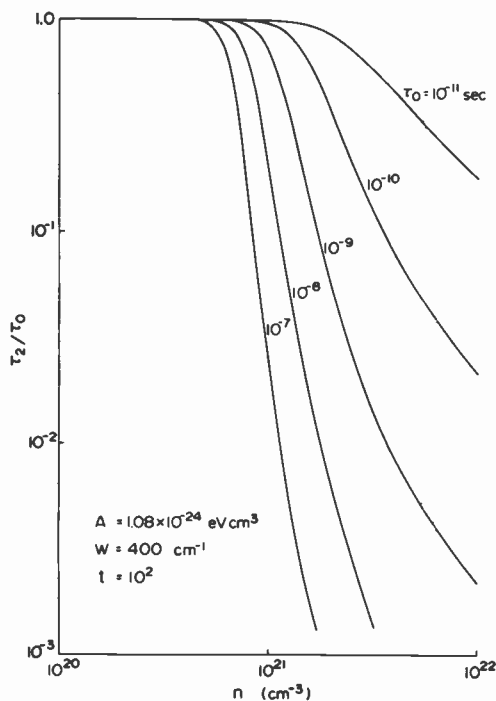


Fig. 10—The normalized life time τ_2/τ_0 plotted as a function of concentration for various values of intrinsic life time.

of Tb^{3+} in a phosphate glass are:

$$\begin{aligned}
 \tau_0 &= 10^{-9} \text{ sec,} \\
 A &= 1.08 \times 10^{-24} \text{ eV cm}^3, \\
 W &= 400 \text{ cm}^{-1}, \\
 n_a &= 10^{-2}.
 \end{aligned}
 \tag{36}$$

In Fig. 9, the normalized life time τ_2/τ_0 is plotted as a function of donor concentration n for the values of τ_0 , A and n_a given above, and for different values of W . The experimental value of I/N_0 as a function of Tb^{3+} concentration is compared with the theoretical results in Fig. 9. Reasonable agreement is obtained for $W = 400 \text{ cm}^{-1}$. Fig. 9 clearly illustrates the significant effect of the inhomogeneous level width. The increase of W rapidly shifts the onset of concentration quenching of τ_2 towards higher concentrations. This in turn increases the luminescence efficiency of the system. From Eq. [33] the emission intensity I is expected to show a peak at the concentration determined by the condition $\partial I/\partial n = 0$. The

peak position shifts toward higher concentration as W increases. The peak height also increases significantly with the increase of W . Since there is no critical concentration at which migration abruptly appears in a dipolar-coupled random system, concentration quenching is important in the range of concentration where the migration decay time becomes comparable with or shorter than the intrinsic life time of the donor. Fig. 10 shows τ_2/τ_0 as a function of concentration for varying τ_0 and fixed values of the other parameters. For 2550 Å excitation of Tb^{3+} in phosphate glass, large values of A , W , and τ_0^{-1} make concentration quenching of this system appear at fairly high Tb concentrations, $n \geq 10^{21} \text{ cm}^{-3}$.

2.5 Discussion and Conclusions

The migration of a Frenkel exciton in a dipolar-coupled random system was studied using Anderson's probabilistic approach, and the results were applied to explain the anomalous concentration quenching for the 2550 Å excitation of Tb^{3+} in $\text{Na}_2\text{Tb}_x\text{Y}_{1-x}\text{P}_4\text{O}_{12}$. The present result is to be compared with that obtained from 2nd order perturbation theory. The Golden Rule gives the single jump rate s_r between the two sites,

$$s_r = \frac{2}{\hbar} \langle |V_{jl}|^2 \rangle_{av} \rho(E), \quad [37]$$

where $\langle |V_{jl}|^2 \rangle_{av}$ is the average over the spatial distribution of the two sites, and $\rho(E)$ is the state density. If one replaces $\rho(E)$ by a value determined by the distribution function for site energy, as is sometimes done, one gets for the square distribution,⁴

$$s_r = \frac{2}{\hbar} \langle |V_{jl}|^2 \rangle_{av} \frac{1}{W}. \quad [38]$$

This is very different from the jump rate, Eq. [24], calculated from Anderson's approach.¹⁷ For example, for very large values of W , the rate from Eq. [38] has an exceedingly large value compared with that from Eq. [24]. Even worse, s_r of Eq. [38] diverges in the limit of vanishing inhomogeneous width, $W = 0$. In contrast, s_r of Eq. [24] converges to a finite value,

$$s_{r0} = (c_1 A n / 2\hbar). \quad [39]$$

Consider what happens physically at $W = 0$, the condition where all the sites have the same excitation energy. Here the randomness of the system is reduced, and the system approaches more closely to the regular one for which the states are spread over the entire lattice to form bands. Consider the simple case of a constant transfer integral $V_{jl} = V$. The state

density is roughly given by $(KV)^{-1}$, where K is the connectivity of the lattice, so that the jump rate evaluated by 2nd order perturbation Eq. [37] becomes

$$s_r = \frac{2V}{\hbar K}. \quad [40]$$

This is roughly equivalent to the result in Eq. [39] from Anderson's theory.

Use of Anderson's approach gives a physically reasonable result in the limit of $W = 0$, and seems to describe the correct state of matter in the whole range of degree of the randomness. Application of the 2nd order perturbation theory, Eq. [38], gives a far less satisfactory, and even erroneous, result for the decay rate s_r .

Strong concentration quenching of exciton life time is expected in the materials in the range of concentration specified by $(W/cAn) \geq 1$. This is the case with the 2550 Å excitation of Tb^{3+} in a phosphate glass and probably also with the 5D_4 excitation of Tb^{3+} in aluminum garnet.¹⁸ For small inhomogeneous widths, $(W/cAn) \ll 1$, the life time is approximated by $\tau_m \simeq 2\hbar/n_a cAn$, which is independent of W and inversely proportional to the donor concentration. Linear concentration dependence has been observed in some substitutional Nd compounds of crystalline state.^{19,20}

Our model includes an energy sink which remains unidentified for the present system, although a 1% fraction of the impurity corresponding to $N_a \leq 10^{19} \text{ cm}^{-3}$, might easily exist in the form of impurity ions such as other rare earth elements, or a defect in the glass matrix. The migration decay can be more conveniently studied in a random system in which both donors and acceptors decay radiatively as in ruby.¹⁶ Here the concentration quenching of the donor life time can be directly measured and simultaneously monitored by the emission of the acceptors.

Finally, our study yields the conclusion which may be of some interest in developing the efficient phosphor or laser materials. In materials that show concentration quenching due to migration decay, the luminescence efficiency can be improved by increasing the inhomogeneous width. This can be achieved, for instance, by changing the material from the crystalline to the amorphous state, or by increasing the local strain on the donor site.

Acknowledgements

The author expresses her gratitude to Dr. H. Fujita for providing the experimental information and to E. O. Johnson and Dr. S. Tosima for their support and reading of the manuscript.

References:

- ¹ See, e.g., earlier works on the luminescence energy migrations: W. J. G. Grant, "Role of Rate Equations in the Theory of Luminescent Energy Transfer," *Phys. Rev.*, **B4**, p. 648 (1971) and M. J. Weber, "Luminescence Decay by Energy Migration and Transfer: Observation of Diffusion-Limited Relaxation," *Phys. Rev.*, **B4**, p. 2932 (1971).
- ² P. W. Anderson, "Absence of Diffusion in Certain Random Lattices," *Phys. Rev.*, **109**, p. 1492 (1958).
- ³ N. F. Mott, "Electrons in Disordered Structures," *Advan. Phys.*, **16**, p. 49 (1967).
- ⁴ A. M. Portis, "Spectral Diffusion in Magnetic Resonance," *Phys. Rev.*, **109**, p. 584 (1956).
- ⁵ S. K. Lyo, "Critical Concentration for Single-Ion-Single-Ion Energy Transfer in Ruby," *Phys. Rev.*, **B3**, p. 3331 (1971); J. Koo, L. R. Walker, and S. Geschwind, "Anderson Localization and Mobility Edges in Ruby," *Phys. Rev. Lett.*, **35**, p. 1669 (1975).
- ⁶ T. Takahashi, O. Yamada, and H. Fujita, private communication.
- ⁷ H. Fujita, private communication.
- ⁸ D. J. Thouless, "Anderson's Theory of Localized States," *J. Phys. C; Solid St. Phys.*, **3**, p. 1559 (1970); *Phys. Rep.*, **13**, p. 93 (1974).
- ⁹ E. W. Montroll, "Random Walks on Lattices Containing Traps," *J. Phys. Soc. Japan Suppl.*, **26**, p. 6 (1969); "Random Walks on Lattices. III. Calculation of First-Passage Times with Application to Exciton Trapping on Photosynthetic Units," *J. Math. Phys.*, **10**, p. 753 (1969).
- ¹⁰ K. Lakatos-Lindenberg and K. E. Shuler, "Random Walks with Nonnearest Neighbor Transitions. I. Analytic 1-D Theory for Next-Nearest Neighbor and Exponentially Distributed Steps," *J. Math. Phys.*, **12**, p. 633 (1971).
- ¹¹ S. Chandrasekhar, *Rev. Mod. Phys.*, **15**, p. 1 (1943).
- ¹² R. Abou-Chakra, P. W. Anderson, and D. J. Thouless, "A Selfconsistent Theory of Localization," *J. Phys. C*, **6**, p. 1734 (1973).
- ¹³ Y. Tsujimoto, Y. Fukuda, and M. Fukai, *J. Electrochem. Soc. Solid-State Sci. and Tech.*, **124**, p. 553 (1971).
- ¹⁴ H. Y. P. Honig, "The Crystal Structure of Ytterbium Metaphosphate, YbP_3O_9 ," *Acta Crystallogr. Sect. B*, **30**, p. 1857 (1974).
- ¹⁵ M. J. Weber, "Nonradiative Decay from 5d States of Rare Earths in Crystals," *Sol. St. Comm.*, **12**, p. 741 (1973).
- ¹⁶ G. F. Imbusch, "Energy Transfer in Ruby," *Phys. Rev.*, **153**, p. 326 (1967).
- ¹⁷ P. W. Anderson, *Comment Solid State Phys.*, **2**, p. 193 (1970).
- ¹⁸ J. P. van der Ziel, L. Kopf, and L. G. Van Uitert, "Quenching of Tb^{3+} Luminescence by Direct Transfer and Migration in Aluminum Garnets," *Phys. Rev.*, **6B**, p. 615 (1972).
- ¹⁹ A. Lempicki, "Concentration Quenching in Nd^{3+} Stoichiometric Materials," *Opt. Comm.*, **23**, p. 376 (1977).
- ²⁰ S. R. Chinn, H. Y. P. Hong, and J. W. Pierce, "Minilasers of Neodymium Compounds," *Laser Focus*, p. 64 (May 1976); S. Singh, D. C. Miller, J. R. Potopowicz, and L. K. Schick, "Emission Cross Section and Fluorescence Quenching of Nd^{3+} Lanthanum Pentaphosphate," *J. Appl. Phys.*, **46**, p. 1191 (1975).

Luminescence of Certain Terbium Metaphosphate Glasses under X-Ray Excitation

T. Takahashi and O. Yamada

RCA Research Laboratories, Inc., Machida City, Tokyo, Japan

Abstract—Luminescence properties under x-ray excitation have been investigated for metaphosphate glasses having the composition $n\text{MO}\cdot\text{Tb}_2\text{O}_3\cdot(n+3)\text{P}_2\text{O}_5$, where $n \geq 0$, M = Mg, Ca, Sr, Ba or Pb, at an x-ray tube voltage between 20 and 60 kV. Measured relative light output, using a $\text{Bi}_4\text{Ge}_3\text{O}_{12}$ crystal as a standard, was found to increase with Tb concentration in the respective glass system, but decreased with increasing atomic weight of M at the same value of n . Light output was further improved by Ce-coactivation. An abrupt increase in relative light output occurred at 60 kV, corresponding to the increase in x-ray absorption coefficient of Tb at its K absorption edge. Light output of a Tb-Ce or Mg-Tb-Ce glass, formed into a suitable shape to converge the emitted light, surpassed that of the $\text{Bi}_4\text{Ge}_3\text{O}_{12}$ crystal at 60 kV. At x-ray energies used in the medical field, 80 to 120 kV, the advantage of the glass should be even greater. Calculations suggest that the use of fibers in an x-ray intensifying screen should be advantageous compared to phosphor screens.

1. Introduction

Several requirements exist for a phosphor used in x-ray radiology and x-ray spectrometry applications. It must have (1) high x-ray absorption, (2) high x-ray to light conversion efficiency, (3) fast on-off response, and (4) chemical and physical stability. The x-ray phosphors that are currently used include CaWO_4 ,¹ $\text{Gd}_2\text{O}_2\text{S:Tb}$,² LaOBr:Tb ³ and CsI:Na ⁴ for x-ray intensifying screens, and NaI:Tl ¹ and $\text{Bi}_4\text{Ge}_3\text{O}_{12}(\text{BGO})$ ⁵ for x-ray scintillation counters. More recently, CdWO_4 is being used as a new x-ray scintillator crystal.⁶ However, no vitreous or glassy phosphor has been

reported as practical for such x-ray applications. A major reason for this must be the low x-ray to light conversion efficiency of the vitreous phosphor as compared to that of the crystalline phosphor.

Recently, a series of alkali terbium yttrium metaphosphate glasses having the composition $nA_2O \cdot (1 - x)Y_2O_3 \cdot xTb_2O_3 \cdot (n + 3)P_2O_5$ was found to luminesce strongly under uv excitation.⁷ The concentration quenching was much reduced in these glasses and their luminescence efficiencies were comparable to other crystalline phosphors. Furthermore, the A_2O component in the above glass formula could be substituted by MO , where M is a divalent cation such as Mg , Ca , Sr , Ba , or Pb . The MO -containing glasses were much less hygroscopic and had less tendency to crack during preparation, as compared to the alkali-containing glasses. Moreover, terbium metaphosphate $Tb_2O_3 \cdot 3P_2O_5$ itself can be made into glass. The $Tb_2O_3 \cdot 3P_2O_5$ glass, as well as the Ba and Pb - Tb glasses, has a relatively high x-ray absorption. Therefore, it was thought worthwhile to investigate the luminescence properties of these glasses under x-ray excitation.

This paper describes the results of such studies. Relative light outputs of $nMO \cdot Tb_2O_3 \cdot (n + 3)P_2O_5$ with or without Ce coactivation, were measured with x-ray excitation in the 20 to 60 kV range using a BGO crystal as a standard. Possible applications of these glasses as vitreous x-ray phosphors are discussed with emphasis on the easy formability of the glass into any desired shape.

2. Experimental

The glass sample was prepared by casting the glassy melt of a stoichiometric mixture of MCO_3 or MO , Tb_4O_7 , and $(NH_4)_2HPO_4$, plus CeO_2 when needed, at 1150–1350°C into a graphite die. After annealing, the glass sample was cut into a rectangular plate $8 \times 8 \times 2.7$ mm. The glass sample of a hemi-ellipsoidal shape was made by casting into a graphite die having a hemi-ellipsoidal bore. The BGO crystal (Harshaw Chemical Co.), used as a standard, was cut into the same rectangular size as the plate glass sample.

The x-ray source was a Siemens Crystalloflex II Cu target tube, operated at a voltage between 20 to 60 kV at a tube current of 15 mA. The x-ray radiation from the tube was collimated into a beam of 4 mm ϕ . An aluminum block 10-mm thick was placed in front of the collimator tube to cut the low energy portion of x-ray radiation including $Cu K\alpha$ at about 8 keV.

Light emitted from the BGO or glass sample was detected with an RCA C83001E photomultiplier fitted with a Teledyne 1090 preamplifier. A Ba-La glass window transparent down to 300 nm was attached in front of the photomultiplier for protection.

dicates that the portion of x-ray radiation with energies below 25 keV was completely absorbed by the Al filter. The relative light outputs for the Mg-Tb glasses decreased with increasing voltage from 30 to 45 kV and then increased abruptly at 60 kV. The x-ray absorption in these glasses is predominantly due to Tb itself, since the x-ray absorption coefficient of an element is proportional to the cube of its atomic number. The x-ray absorption coefficient of Tb decreases monotonically with increasing photon energy below 50 keV, but increases abruptly at its K absorption edge ($E = 52.0$ keV).⁹ Hence, x-ray absorption of a Tb-containing glass should also increase abruptly for the x-ray radiation containing x-ray photons with $E \geq 52$ keV. In Fig. 3, the calculated x-ray absorption coefficients for BGO, $Tb_2O_3 \cdot 3P_2O_5$, and $6MgO \cdot Tb_2O_3 \cdot 9P_2O_5$ are shown as a function of x-ray photon energy. Since the Tb^{3+} emission was assumed to be generated predominantly from the x-ray photons absorbed by Tb^{3+} ions, its intensity should increase when the x-ray absorption coefficient of Tb increases. The results shown in Fig. 2 confirm that this is indeed the case.

The average energy of x-ray photons, or the most probable energy, in the continuous x-ray radiation is known to have a value about 1/2 of the peak tube voltage. For the Siemens Cu-target tube used in our experiments, an average energy of about 35 keV was obtained at 60 kV from

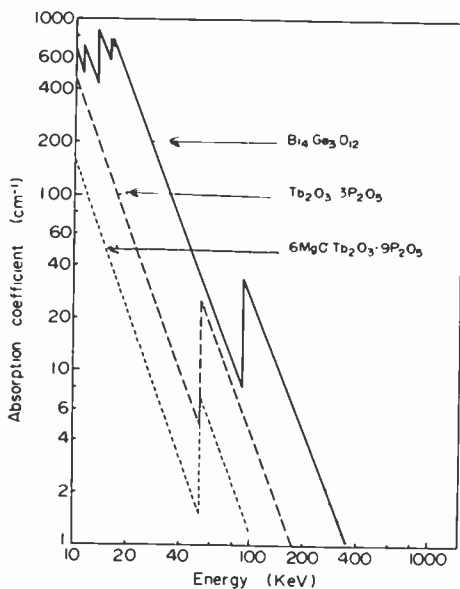


Fig. 3—Calculated x-ray absorption coefficients for $Bi_4Ge_3O_{12}$, $Tb_2O_3 \cdot 3P_2O_5$ and $6MgO \cdot Tb_2O_3 \cdot 9P_2O_5$ versus x-ray photon energy.

the x-ray absorption measurement of aluminum.⁸ On the other hand, the maximum efficiency of the Tb metaphosphate glass should be realized for the x-ray radiation having an average photon energy of 52 keV. Since most x-ray tubes used for medical diagnosis are operated at a voltage between 80 and 120 kV, the use of a Tb or Mg-Tb metaphosphate glass as an x-ray scintillator seems to be promising.

3.3 Enhancement due to Ce Coactivation

The addition of Ce has been known to enhance the Tb^{3+} emission in inorganic glasses under uv excitation.^{7,10} It is not known, however, whether the same sensitization occurs under x-ray excitation. In order to study the effect of Ce coactivation on the x-ray luminescent properties, Ce was added in place of the Tb in the Tb and Mg-Tb metaphosphate glasses. Fig. 4 shows the relative light output data for $nMgO \cdot (1-x)Tb_2O_3 \cdot xCe_2O_3 \cdot (n+3)P_2O_5$ glasses at 60 kV. In all systems, the addition of Ce brought about an increase in light output with x-ray excitation just as in the case of uv excitation. However, the Ce concentration needed to produce a maximum of light output differs in the respective systems. It seems that the optimum Ce concentration is higher in a glass with high MgO content. The highest light output was observed for $MgO \cdot 0.925Tb_2O_3 \cdot 0.075Ce_2O_3 \cdot 4P_2O_5$ glass and it was higher than the light output of BGO standard.

None of these Tb-containing metaphosphate glasses showed any sign of discoloration after repeated exposures to x-ray radiation.

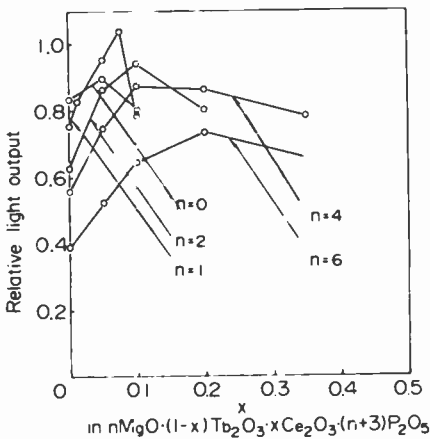


Fig. 4—Relative light outputs of $nMgO \cdot (1-x)Tb_2O_3 \cdot xCe_2O_3 \cdot (n+3)P_2O_5$ glasses.

3.4 Effect of Sample Shape

Several plate samples of different thicknesses of a low x-ray absorbing $6\text{MgO}\cdot\text{Tb}_2\text{O}_3\cdot 9\text{P}_2\text{O}_5$ glass were tested to see whether a change in x-ray absorption induces a proportional change in light output. The results are shown in Table 1, together with the x-ray absorption data, where I/I_0 is the measured intensity ratio of transmitted and incident x-rays. As can be seen, no improvement in light output was achieved for thicker samples, contrary to our expectations. This should mean that any increase in emitted light was dissipated in the thicker samples, probably due to scattering. It was observed that the light emitting area of a plate glass sample was confined to a very thin layer underneath the radiated surface. In such a situation, the loss due to scattering is expected to be considerable, especially when the thickness of sample is increased. Apparently, only a fraction of emitted light reaches the PMT detector in the case of the plate samples.

To reduce the light loss due to scattering, a glass sample may be formed into an appropriate shape to converge or focus emitted light onto a PMT. For example, any light passing through a focal point of an ellipsoid will be reflected into the other focal point on its axis. In the case of a paraboloid, any light passing through its focal point will be reflected to become parallel to its axis. Forming a glass into a desired shape by casting is much easier than machining a scintillator crystal such as NaI:Tl or BGO into a desired shape.

To test the effects of glass shaping, several Tb-Ce and Mg-Tb-Ce glasses were formed into a hemi-ellipsoidal shape ($a/b \sim 3.7$, $a \sim 8$ mm) by casting, and their relative light outputs were measured at 60 kV. The results are summarized in Table 2, together with the data for respective plate samples with a thickness of 2.7 mm. Also included in the table were the relative intensities of the transmitted x-rays for the respective samples. The light output of the hemi-ellipsoidal sample was about 50% better than that of the plate sample in the glasses with $n = 0$ to 4. For

Table 1—Light Output and X-Ray Absorption Data for Plate Samples of Different Thicknesses of $6\text{MgO}\cdot\text{Tb}_2\text{O}_3\cdot 9\text{P}_2\text{O}_5$ Glass for 60 kV X-Ray Excitation. I/I_0 is the Measured Intensity Ratio of Transmitted and Incident X-Rays.

Thickness (mm)	I/I_0	Light Output (Arbitrary Units)
1.00	5.83×10^{-1}	3.10
1.50	4.45×10^{-1}	3.25
2.00	3.40×10^{-1}	3.27
2.45	2.66×10^{-1}	3.26
3.00	1.98×10^{-1}	3.27
3.35	1.64×10^{-1}	3.13
3.45	1.55×10^{-1}	3.11

Table 2—Relative Light Output (RLO) and X-Ray Absorption Data for the Plate and Hemi-ellipsoidal Samples of Tb-Ce and Mg-Tb-Ce Glasses for 60 kV X-Ray Excitation. I/I_0 is the Measured Intensity Ratio of Transmitted and Incident X-Rays.

Sample Composition	$8 \times 8 \times 2.7 \text{ mm}^2$ plate		Hemi-ellipsoid ($a/b \sim 3.7, a \sim 8 \text{ mm}$)	
	I/I_0	RLO	I/I_0	RLO
$\text{Bi}_4\text{Ge}_3\text{O}_{12}$	10^{-8*}	1.000	—	—
$0.95\text{Tb}_2\text{O}_3 \cdot 0.05\text{Ce}_2\text{O}_3 \cdot 3\text{P}_2\text{O}_5$	3.8×10^{-2}	0.897	10^{-5}	1.348
$0.9\text{Tb}_2\text{O}_3 \cdot 0.1\text{Ce}_2\text{O}_3 \cdot 3\text{P}_2\text{O}_5$	7.4×10^{-2}	0.798	10^{-4}	1.118
$\text{MgO} \cdot 0.95\text{Tb}_2\text{O}_3 \cdot 0.05\text{Ce}_2\text{O}_3 \cdot 4\text{P}_2\text{O}_5$	7.6×10^{-2}	0.952	10^{-4}	1.281
$\text{MgO} \cdot 0.9\text{Tb}_2\text{O}_3 \cdot 0.1\text{Ce}_2\text{O}_3 \cdot 4\text{P}_2\text{O}_5$	3.8×10^{-2}	0.789	10^{-4}	1.185
$2\text{MgO} \cdot 0.9\text{Tb}_2\text{O}_3 \cdot 0.1\text{Ce}_2\text{O}_3 \cdot 5\text{P}_2\text{O}_5$	1.2×10^{-1}	0.941	10^{-2}	1.379
$2\text{MgO} \cdot 0.8\text{Tb}_2\text{O}_3 \cdot 0.2\text{Ce}_2\text{O}_3 \cdot 5\text{P}_2\text{O}_5$	9.4×10^{-2}	0.801	10^{-3}	1.264
$4\text{MgO} \cdot 0.9\text{Tb}_2\text{O}_3 \cdot 0.1\text{Ce}_2\text{O}_3 \cdot 7\text{P}_2\text{O}_5$	1.7×10^{-1}	0.873	10^{-3}	1.288
$4\text{MgO} \cdot 0.8\text{Tb}_2\text{O}_3 \cdot 0.2\text{Ce}_2\text{O}_3 \cdot 7\text{P}_2\text{O}_5$	1.3×10^{-1}	0.863	10^{-3}	1.259
$4\text{MgO} \cdot 0.65\text{Tb}_2\text{O}_3 \cdot 0.35\text{Ce}_2\text{O}_3 \cdot 7\text{P}_2\text{O}_5$	1.4×10^{-1}	0.784	10^{-3}	1.077
$6\text{MgO} \cdot 0.9\text{Tb}_2\text{O}_3 \cdot 0.1\text{Ce}_2\text{O}_3 \cdot 9\text{P}_2\text{O}_5$	2.4×10^{-1}	0.645	10^{-2}	1.173
$6\text{MgO} \cdot 0.8\text{Tb}_2\text{O}_3 \cdot 0.2\text{Ce}_2\text{O}_3 \cdot 9\text{P}_2\text{O}_5$	1.9×10^{-1}	0.736	10^{-2}	1.264
$6\text{MgO} \cdot 0.65\text{Tb}_2\text{O}_3 \cdot 0.35\text{Ce}_2\text{O}_3 \cdot 9\text{P}_2\text{O}_5$	6.7×10^{-1}	0.652	10^{-2}	1.206

* Estimated from the calculated absorption coefficient of BGO.

the glasses with $n = 6$, as much as 80% increase in light output was observed. The gain in light output in the glasses with high x-ray absorption ($n = 0$ and 1) can be explained mostly by the light converging effect. However, in the glasses with low x-ray absorption ($n = 4$ and 6), it should also be partially due to an increase in x-ray absorption in the hemi-ellipsoidal sample. Contrary to the case of a plate sample, an increase in x-ray absorption produces a proportional increase in light output in a hemi-ellipsoidal sample as expected. The light outputs for all the hemi-ellipsoidal samples tested surpassed that of the BGO plate. Also, it should be noted that such a high performance of the Tb metaphosphate glass scintillator was accomplished using a photomultiplier whose wavelength-dependent sensitivity was not best suited for the spectrum of the Tb^{3+} emission. Namely, the relative responsivity of RCA C83001E photomultiplier detector at the 544nm Tb^{3+} emission is only 50%, whereas that for the BGO emission maximum at 480nm is about 85%.

The use of Tb metaphosphate glass in fiber form is another way to enhance its efficiency. A bundle of fine glass fibers used as a scintillator could be as efficient as a hemi-ellipsoidal sample. A sheet of piled glass fibers, with the fiber axes aligned parallel to an x-ray beam, could be used as an x-ray intensifying screen. A simple calculation, whose results are tabulated in Table 3, shows that such a glass fiber pile screen is as efficient, or better, than existing powder phosphor screens. In the calculation of Table 3, 100- μm thick screens with packing density of 50% are chosen because the optimum front-screen light output occurs at a small layer thickness.² For back-screen applications, much thicker screens are

Table 3—Calculated Light Outputs* for Several Phosphor Screens at the X-Ray Photon Energy of 55 keV.

Phosphor	X-Ray Absorption ^{**} $1 - I/I_0$ (%)	X-Ray to Light Conversion Efficiency ^{***} η_x (%)	Screen Energy Loss Correction Factor C_s	Light Output $(1 - I/I_0) \cdot \eta_x \cdot C_s$
CaWO ₄	10.0	6.5	0.5	33
Zn ₂ SiO ₄ :Mn	2.5	11.5	0.5	14
ZnS:Ag	3.5	17.0	0.5	30
CsI:Tl	7.0	10.0	0.7	49
La ₂ O ₂ S:Tb	20.0	12.5	0.5	125
Gd ₂ O ₂ S:Tb	22.0	13.0	0.5	143
MgO·Tb ₂ O ₃ ·4P ₂ O ₅ glass fiber	90.0	1.5	1.0	135

* Detection efficiency is not taken into consideration.

** The x-ray absorption data are calculated for 100- μ m-thick screens, except for the glass fiber screen. The packing density is assumed to be 50% for the powder screens, and 90% for the evaporated CsI·Tl and glass fiber screens (see text).

*** The η_x data are taken from Table 2 of Ref. (2). The η_x of MgO·Tb₂O₃·4P₂O₅ glass is estimated from our measurements, assuming $\eta_x = 0.8\%$ for BGO.

preferable. In any case, the optimum screen thickness is different for different phosphors and also depends on whether the screen is used in front- or back-screen applications. Therefore, the comparison of Table 3 could be unfair to one phosphor and too optimistic to another.

Furthermore, it is anticipated that the fiber diameters can be chosen to optimize image resolution with negligible effect on efficiency performance, a circumstance not possible with phosphor screens. If phosphors screens are made thinner to improve resolution, then light output efficiency suffers. On the other hand, decreasing glass fiber diameter should improve image resolution with little if any effect on the visible light output from the fiber screen. A relatively lower x-ray to light conversion efficiency of the Tb metaphosphate glass, therefore, can be more than compensated by its easy formability into any desired shape.

Finally, a preliminary measurement indicated that the rise time for Tb³⁺ emission was of the order of 10⁻⁶ sec, but the decay time was of the order of 10⁻³ sec in the Tb metaphosphate glass.¹¹ For rapid scanning applications such as that used in the early model of x-ray tomography equipment,¹² the decay time of a few milliseconds is much too slow. However, for most x-ray radiology applications, the decay time of this magnitude should not be unacceptable.

4. Summary

Light outputs were measured of the Tb metaphosphate glasses with the composition $n\text{MO} \cdot \text{Tb}_2\text{O}_3 \cdot (n + 3)\text{P}_2\text{O}_5$ for 20 to 60 kV x-ray excitation. A decrease in light output with increasing atomic weight of M was ob-

served and interpreted as nonluminescent x-ray absorption by M^{2+} ions. Light output increased with increasing Tb concentration indicating that Tb^{3+} emission was predominantly generated from the x-ray radiation absorbed directly by Tb^{3+} ions. An abrupt jump in relative light output with respect to a BGO standard at 60 kV was interpreted as an increase in the x-ray absorption coefficient of Tb at its K absorption edge. Ce coactivation enhanced the Tb^{3+} emission under x-ray excitation as in the case of uv excitation. By forming a glass sample into a hemi-ellipsoidal shape to converge the emitted light onto a detector, as much as 50% increase in light output was achieved over that of a plate sample. Light outputs of the hemi-ellipsoidal Tb-Ce and Mg-Tb-Ce glass samples exceeded that of a BGO plate by as much as 40% for 60 kV x-ray excitation. An even greater advantage is anticipated at the higher x-ray energies, 80–120 kV, used in the medical diagnosis field. Calculations suggest that the use of glass fibers for an x-ray intensifying screen will be competitive with phosphors in light output and probably superior with respect to image resolution.

Acknowledgments

The authors wish to thank E. O. Johnson, who first attracted our attention to the x-ray scintillator problem and gave many valuable suggestions throughout the course of this work. They also wish to thank R. W. Engstrom and S. Larach, who provided much useful information on x-ray scintillator material and its applications. The BGO crystal used as a standard was kindly supplied by R. W. Engstrom.

References:

- ¹ H. W. Leverenz, *An Introduction to Luminescence of Solids*, p. 421, Dover, N.Y. (1968).
- ² J. A. dePoorter and A. Brill, "Absolute X-Ray Efficiencies of Some Phosphors," *J. Electrochem. Soc.*, **122**, p. 1086 (1975).
- ³ J. G. Rabatin, *Electrochem. Soc. Spring Meeting Extended Abstract No. 102* (1974).
- ⁴ A. L. N. Stevels and F. Pingault, "BaFCl:Eu²⁺: A New Phosphor for X-Ray-Intensifying Screens," *Philips Res. Repts*, **30**, p. 277 (1975).
- ⁵ M. J. Weber and R. R. Monchamp, "Luminescence of $Bi_4Ge_3O_{12}$: Spectral and Decay Properties," *J. Appl. Phys.*, **44**, p. 5495 (1973).
- ⁶ R. W. Engstrom, private communication.
- ⁷ T. Takahashi and O. Yamada, "Luminescence of Tb-Activated Alkali Rare Earth Metaphosphate Glasses," *J. Electrochem. Soc.*, in press.
- ⁸ T. Takahashi and O. Yamada, unpublished work.
- ⁹ E. Storm and H. I. Israel, *Natl. Tech. Information Service Rept. LA 3753* (1967).
- ¹⁰ S. Shionoya and E. Nakazawa, "Sensitization of Tb^{3+} Luminescence by Ce^{3+} and Cu^{1+} in Glasses," *Appl. Phys. Lett.*, **6**, p. 118 (1965).
- ¹¹ H. Fujita, private communication.
- ¹² T. Iinuma, "Transmission and Emission Computed Tomography," *Oyo Butsuri (Applied Physics)*, **47**, p. 304 (1978) (in Japanese).

Thermal Properties of New Metaphosphate Glasses

O. Yamada and T. Takahashi

RCA Research Laboratories, Inc., Machida City, Tokyo, Japan

Abstract—Thermal properties have been measured of new metaphosphate glasses having a general composition nM_2O or $nMeO \cdot R_2O_3 \cdot (n+3)P_2O_5$, where $n \geq 0$, M = alkali metal, Me = alkaline earth metal, and R = Y or a rare-earth metal. These glasses were prepared easily at relatively low temperatures. The glass transition temperatures (T_g) of these were in the range 440 to 640°C, and the coefficients of linear thermal expansion (α_l) were 5×10^{-6} to $18 \times 10^{-6}/^\circ\text{C}$ at $T < T_g$. The thermal properties changed considerably in alkaline earth rare earth glasses but not so much in alkali rare earth glasses. For example, the change of α_l in the alkaline earth rare earth metaphosphate glasses was much greater than that in the alkali rare earth metaphosphate glasses having a fixed value of n .

1. Introduction

Alkali or alkaline earth metaphosphate (MP) glasses consist of a chain structure in which all PO_4 tetrahedra share the corners to form a continuous one-dimensional network. Thermal properties and crystallization below the glass transition temperature T_g of the MP glasses, especially of the alkaline earth MP glasses, have been extensively studied.^{1,2,3} The structure of these glasses was also investigated in detail^{4,5} by using the fluorescent properties of the glasses when doped with a probing activator at low concentrations.

On the other hand, several new rare earth MP's, $Nd_{1-x}R_xP_3O_9$, pentaphosphate's $Nd_{1-x}R_xP_5O_{14}$, with R = Y or La, and alkali rare earth metaphosphates $MNdP_4O_{12}$, have been investigated.⁶⁻⁸ These materials

exhibited good lasing action despite a high Nd concentration. Recently, lithium rare earth phosphates ($\text{LiY}_{1-x}\text{R}_x\text{P}_4\text{O}_{12}$, $\text{R} = \text{Eu}$ or Tb) and rare earth metaphosphates ($\text{Y}_{1-x}\text{R}_x\text{P}_3\text{O}_9$, $\text{R} = \text{Eu}$ or Tb), also having a high concentration of Tb^{3+} or Eu^{3+} , have been reported to be efficient phosphor materials.⁹ From the determination of the crystal structures, it was found that the PO_4 tetrahedron made up a network sharing the corners of each PO_4 like a helical ribbon except for the pentaphosphate (e.g. $\text{NdP}_5\text{O}_{14}$).^{10,11} It was also found that the active rare earth ions were isolated from each other by a PO_4 network and, consequently, those crystalline phosphates exhibited reduced concentration quenching.

Recently, we have found that a series of transparent glasses having a composition $n\text{M}_2\text{O}$ or $n\text{MeO}\cdot\text{R}_2\text{O}_3\cdot(n+3)\text{P}_2\text{O}_5$, where $n \geq 0$, $\text{M} =$ alkali metal, $\text{Me} =$ alkaline earth metal, and $\text{R} = \text{Y}$ or a rare earth metal, can be prepared easily. Such glasses also can be made to fluoresce effectively if a suitable activator is incorporated.¹²

Glass maintains an internally stored thermal history, and its physical properties are in turn affected by this thermal history. It is, therefore, important to understand and make use of the thermal properties of such glasses in acquiring an understanding of other properties, such as luminescence. Moreover, knowledge of thermal properties is also indispensable in the application of these luminescent glasses, such as for plasma displays¹³ or x-ray scintillators.¹⁴ This paper reports the fundamental thermal properties of some of these new alkali or alkaline earth rare earth metaphosphate glasses.

2. Experimental Procedure

Stoichiometric amounts of M_2HPO_4 , M_2CO_3 , MeO or MeCO_3 , $(\text{NH}_4)_2\text{HPO}_4$, R_2O_3 , and activator (TlCl , Tb_4O_7 , CeO_2) were thoroughly mixed in a ball mill for a day. Y_2O_3 and Tb_4O_7 were of 3N grade obtained from Shinetsu Chemicals, and La_2O_3 and Ce_2O_3 were of 4N grade obtained from Wako Chemicals. The mixture was placed in a high alumina crucible with a lid and was slowly heated to 700°C at the rate of $25\text{--}30^\circ\text{C/hr}$ to prevent overflow from the crucible during strong reactions, especially with $\text{Me} = \text{Mg}$ and Ca . The mixture was kept at 700°C for a few hours to remove evolving gases. After the preheating, the mixture was melted at 1050 to 1400°C and kept at that temperature for a few hours to homogenize. The melt was then poured into a cylindrical graphite die 13 to 20 mm in diameter. The cast glass was annealed at $450\text{--}560^\circ\text{C}$ for a day in a box furnace to remove thermal strain. Afterwards, it was slowly cooled over a day to room temperature. No chemical analyses were made on the glasses thus obtained. The resulting glass was cut with a sintered-silicon carbide blade saw into a rectangular bar shape,

$3 \times 3 \times 10 \sim 15 \text{ mm}^3$ in size, and then ground and polished with 1000 mesh abrasive for the thermal expansion measurements.

Differential thermal dilatometric analyses of the glasses were carried out using a Rigaku Electric Company M8095 standard-type thermal dilatometer. Its deviation detection mechanism is based on a differential transformer method.¹⁵ A quartz glass was used as a standard ($\alpha_t = 6.0 \times 10^{-7}/^\circ\text{C}$). A constant load of 20g was applied on both the sample and the quartz reference. A typical rate of heating was about $5^\circ\text{C}/\text{min}$.

3. Results and Discussion

The glass transition temperature (T_g) was determined experimentally from the thermal expansion curve,² and the linear thermal expansion coefficient (α_t) was also calculated from the straight line region below T_g , as in Fig. 1. Experimental error in the present work was within $\pm 2\%$ for α_t , and within $\pm 2^\circ\text{C}$ for T_g on repeated runs for one sample. The deformation temperature (T_d) varied with the weight of the load applied to the specimen. In Fig. 1, almost the same values of T_g and α_t were obtained in the curves of (a) and (b), although the quenched sample (curve (b)) showed the deviation from the straight line above 434°C . Such deviation occurred in the more poorly annealed samples as a result of thermal stress relaxation.

Figs. 2 and 3 show T_g and α_t of various alkali or alkaline earth terbium MP glasses when n was fixed in $n\text{M}_2\text{O}$ or $n\text{MeO} \cdot \text{Tb}_2\text{O}_3 \cdot (n + 3)\text{P}_2\text{O}_5$. Fig. 2 shows that an increasing atomic number of the alkali metal tends to raise the temperature of T_g , but causes almost no variation in α_t . On

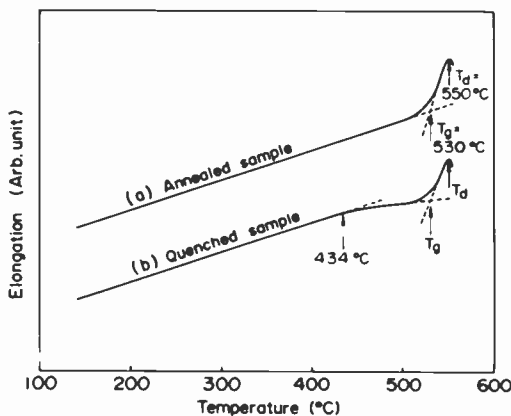


Fig. 1—Typical thermal expansion curve of some MP glasses ($4\text{BaO} \cdot 0.7\text{La}_2\text{O}_3 \cdot 0.3\text{Tb}_2\text{O}_3 \cdot 7\text{P}_2\text{O}_5$, Heating Rate, $4\text{--}5^\circ\text{C}/\text{min}$).

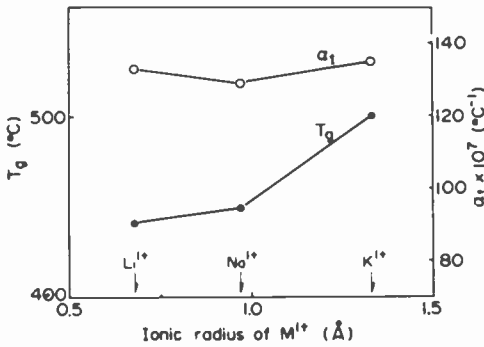


Fig. 2— T_g and α_t of the MP glasses in $2M_2O \cdot Tb_2O_3 \cdot 5P_2O_5$ versus ionic radius of alkali metal ions (M^{1+}).

the other hand, for the alkaline earth terbium MP glasses shown in Fig. 3, T_g was lowered and α_t increased with increasing atomic number (or ionic radius) of the alkaline earth metal. Corresponding to the behavior of α_t in both series, a similar tendency was observed in the density data of those glasses, summarized in Table 1. This suggests a relation between α_t and density in these series. As expected, the thermal properties of alkaline earth terbium MP glasses were found to approach those of the alkaline earth MP glasses³ at low Tb_2O_3 concentrations. The value of T_g decreased gradually and α_t increased with decreasing concentration of Tb_2O_3 in the range below 8.3 mole % Tb_2O_3 , and, finally, each T_g or α_t value approached that of the respective alkaline earth MP glass.

The data of other series of MP glasses are listed in Table 2. In $2Na_2O \cdot (1-x)Y_2O_3 \cdot xTb_2O_3 \cdot 5P_2O_5$ (series A) and $4BaO \cdot (1-x)La_2O_3 \cdot$

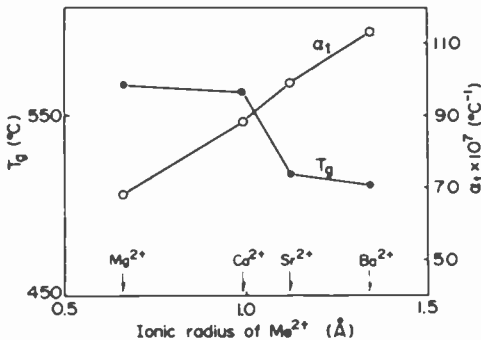


Fig. 3— T_g and α_t of the MP glasses in $4MeO \cdot Tb_2O_3 \cdot 7P_2O_5$ versus ionic radius of alkaline earth metal ions (Me^{2+}).

Table 1—Linear Thermal Expansion Coefficient and Density for Alkali and Alkaline Earth Rare-Earth MP Glasses

Composition	$\alpha_t \times 10^7$ ($^{\circ}\text{C}^{-1}$)	Density (g/cm^3)
2Li ₂ O·Tb ₂ O ₃ ·5P ₂ O ₅	133	3.16
2Na ₂ O·Tb ₂ O ₃ ·5P ₂ O ₅	129	3.14
2K ₂ O·Tb ₂ O ₃ ·5P ₂ O ₅	135	3.10
4MgO·Tb ₂ O ₃ ·7P ₂ O ₅	68	2.94
4CaO·Tb ₂ O ₃ ·7P ₂ O ₅	88	3.11
4SrO·Tb ₂ O ₃ ·7P ₂ O ₅	99	3.40
4BaO·Tb ₂ O ₃ ·7P ₂ O ₅	113	3.72

xTb₂O₃·7P₂O₅ (series B), no anomalous change of thermal properties was observed, especially for α_t . This is due to the small difference in ionic radius between Y³⁺ (0.89Å) and Tb³⁺ (0.92Å) or La³⁺ (1.01Å) and Tb³⁺. Results similar to those for series A and B were found in 2(1 - y)·M₂O·2yTl₂O·R₂O₃·5P₂O₅ (series D), where M = Li or Na, 0.024 ≤ y ≤

Table 2—Data of Thermal Properties for Various Series of MP Glasses

Composition	T_g ($^{\circ}\text{C}$)	$\alpha_t \times 10^7$ ($^{\circ}\text{C}^{-1}$)
Ni Metal (Known Sample)	—	168
(A) 2Na ₂ O·0.95Y ₂ O ₃ ·0.05Tb ₂ O ₃ ·5P ₂ O ₅	449	120
2Na ₂ O·0.9Y ₂ O ₃ ·0.1Tb ₂ O ₃ ·tP ₂ O ₅	460	117
2Na ₂ O·0.7Y ₂ O ₃ ·0.3Tb ₂ O ₃ ·5P ₂ O ₅	456	111
2Na ₂ O·0.5Y ₂ O ₃ ·0.5Tb ₂ O ₃ ·5P ₂ O ₅	457	121
2Na ₂ O·0.3Y ₂ O ₃ ·0.7Tb ₂ O ₃ ·5P ₂ O ₅	459	121
2Na ₂ O·Tb ₂ O ₃ ·5P ₂ O ₅	449	129
(B) 4BaO·La ₂ O ₃ ·7P ₂ O ₅	511	107
4BaO·0.9La ₂ O ₃ ·0.1Tb ₂ O ₃ ·7P ₂ O ₅	523	117
4BaO·0.7La ₂ O ₃ ·0.3Tb ₂ O ₃ ·7P ₂ O ₅	530	115
4BaO·0.5La ₂ O ₃ ·0.5Tb ₂ O ₃ ·7P ₂ O ₅	509	120
4BaO·Tb ₂ O ₃ ·7P ₂ O ₅	511	113
(C) MgO·Tb ₂ O ₃ ·4P ₂ O ₅	605	55
MgO·0.95Tb ₂ O ₃ ·0.05Ce ₂ O ₃ ·4P ₂ O ₅	592	86
MgO·0.9Tb ₂ O ₃ ·0.1Ce ₂ O ₃ ·4P ₂ O ₅	623	66
4MgO·Tb ₂ O ₃ ·7P ₂ O ₅	567	68
4MgO·0.95Tb ₂ O ₃ ·0.05Ce ₂ O ₃ ·7P ₂ O ₅	569	68
4MgO·0.9Tb ₂ O ₃ ·0.1Ce ₂ O ₃ ·7P ₂ O ₅	568	87
(D) 1.95Li ₂ O·0.05Tl ₂ O·Y ₂ O ₃ ·5P ₂ O ₅	425	109
1.8Li ₂ O·0.2Tl ₂ O·Y ₂ O ₃ ·5P ₂ O ₅	432	97
1.6Li ₂ O·0.4Tl ₂ O·Y ₂ O ₃ ·5P ₂ O ₅	407	119
1.4Li ₂ O·0.6Tl ₂ O·Y ₂ O ₃ ·5P ₂ O ₅	380	106
1.2Li ₂ O·0.8Tl ₂ O·Y ₂ O ₃ ·5P ₂ O ₅	409	105
1.8Na ₂ O·0.2Tl ₂ O·Y ₂ O ₃ ·5P ₂ O ₅	444	99
1.8Li ₂ O·0.2Tl ₂ O·Y ₂ O ₃ ·5P ₂ O ₅	434	105
5.1Li ₂ O·0.9Tl ₂ O·Y ₂ O ₃ ·9P ₂ O ₅	308	181
5.4Li ₂ O·0.6Tl ₂ O·Y ₂ O ₃ ·9P ₂ O ₅	363	134

0.4, and $R = Y$ or Gd , despite a large difference in ionic radius between $Li^{1+}(0.68\text{\AA})$ or $Na^{1+}(0.97\text{\AA})$ and $Tl^{1+}(1.47\text{\AA})$. These T_g and α_t results agreed closely with the results in Fig. 2. When the n value was changed to 6, however, T_g dropped about 100°C and α_t increased approximately two-fold compared with the $n = 2$ case. On the other hand, no systematic change in thermal properties was observed in series C, $nMgO \cdot (1-x) \cdot Tb_2O_3 \cdot xCe_2O_3 \cdot (n+3)P_2O_5$, where $n = 1, 4$ and $x = 0, 0.05, 0.1$.

The T_g and α_t values of $nMgO \cdot Tb_2O_3 \cdot (n+3)P_2O_5$ glasses, where $n = 0-6$, are plotted against mole % of Tb_2O_3 in Fig. 4. The T_g value of these glasses rose linearly with increasing mole % of Tb_2O_3 up to about 20% (corresponding to $n = 0.5$), then temporarily fell, and again rose abruptly to the T_g value for $Tb_2O_3 \cdot 3P_2O_5$. On the other hand, the value of α_t decreased gradually with increasing Tb_2O_3 content up to about 17 mole % and then started to exhibit a complicated variation against the concentration of Tb_2O_3 above 19 mole %. It is presumed that above 15 mole % of Tb_2O_3 some changes in the glass structure that have an influence on T_g or α_t might be taking place.

4. Conclusion

In the series of alkali rare earth MP glasses, the value of α_t was hardly affected by alkali or rare-earth metal species, but the value of T_g rose with increasing ionic radius of the alkali metal when the alkali concentration was fixed. However, with increasing alkali concentration, the value of α_t increased and the value of T_g decreased.

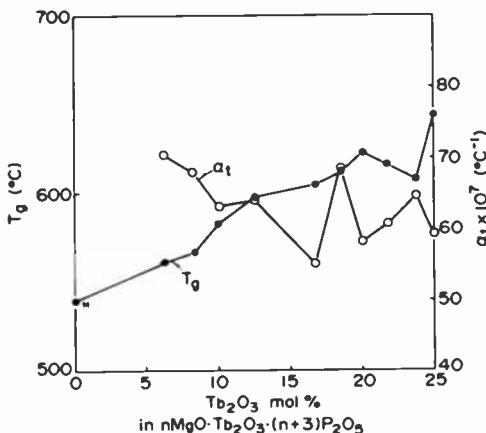


Fig. 4— T_g and α_t versus Tb_2O_3 mole % in $nMgO \cdot Tb_2O_3 \cdot (n+3)P_2O_5$ glasses *: Reference 3)

In the series of alkaline earth rare-earth MP glasses, the values of T_g and α_t varied significantly when the alkaline earth metal species or alkaline earth content is changed. The value of T_g had a tendency to fall with increasing ionic radius and concentration of the alkaline earth metal. The value of α_t increased linearly with increasing ionic radius of the alkaline earth metal, but changed in a very complicated fashion with its concentration, especially in the Mg-Tb MP glass series.

In general, the T_g values of alkali rare earth MP glasses were lower than those of alkaline earth rare-earth MP glasses, and the α_t values of alkali rare-earth MP glasses were higher than those of the alkaline earth rare-earth MP glasses.

Acknowledgment

The authors wish to thank E. O. Johnson for a critical reading of this manuscript. They also wish to thank Prof. Imaoka and Dr. Yasui, the Institute of Industrial Science, University of Tokyo, for the use of the dilatometer and for much valuable advice. Finally, they wish to thank Y. Shimizu for his technical assistance.

References

- ¹ Y. Abe, "Kinetic Studies on Crystallization of Magnesium Metaphosphate Glass," *Yogyo Kyokai Shi*, **82** (1), p. 35 (1974) (in Japanese).
- ² Y. Abe, T. Arahori, and A. Naruse, "Crystallization of $\text{Ca}(\text{PO}_3)_2$ Glass below the Glass Transition Temperature," *J. Am. Ceram. Soc.*, **59** (11-12), p. 487 (1976).
- ³ Y. Abe and H. Saito, "Crystallization of Glass below the Glass Transition Temperature— $\text{Ca}(\text{PO}_3)_2$ Glass and Other Glasses," *Yogyo Kyokai Shi*, **85** (2), p. 45 (1977) (in Japanese).
- ⁴ R. Reisfeld, L. Boehm, M. Ish-Shalom, and R. Fischer, "4f-4f Transition and Charge Transfer Spectra of Eu^{3+} , 4f-5d Spectra of Tb^{3+} , and $^1\text{S}_0 \rightarrow ^3\text{P}_1$ Spectra of Pb^{2+} in Alkaline Earth Metaphosphate Glasses," *Phys. Chem. Glasses*, **15** (3), p. 76 (1974).
- ⁵ T. Komiyama and T. Ueno, "Compositional and Temperature Dependency of Emission Spectra of Eu^{3+} in Glasses," *Yogyo Kyokai Shi*, **80** (6), p. 227 (1972) (in Japanese).
- ⁶ H. G. Danielmeyer and H. P. Weber, "Fluorescence in Neodymium Ultraphosphate," *IEEE J. Quantum Electron.*, QE-8, p. 805 (1972).
- ⁷ H. Y-P. Hong, "The Crystal Structure of Ytterbium Metaphosphate, YbP_3O_9 ," *Acta Cryst.*, **B30**, p. 1857 (1974).
- ⁸ T. Yamada, K. Otsuka, and J. Nakano, "Fluorescence in Lithium Neodymium Ultraphosphate Single Crystals," *J. Appl. Phys.*, **45**, p. 5096 (1974).
- ⁹ Y. Tsujimoto, Y. Fukuda, and M. Fukai, "Preparation and Fluorescence Properties of Lithium Rare Earth Phosphate Phosphors," *J. Electrochem. Soc.*, **124**, p. 553 (1977).
- ¹⁰ H. Y-P. Hong, "Crystal Structures of Neodymium Metaphosphate (NdP_3O_9) and Ultraphosphate ($\text{NdP}_5\text{O}_{14}$)," *Acta Cryst.*, **B30**, p. 468 (1974).
- ¹¹ H. Y-P. Hong, "Crystal Structure of Potassium Neodymium Metaphosphate, $\text{KNdP}_4\text{O}_{12}$, A New Acentric Laser Material," *Mat. Res. Bull.*, **10**, p. 1105 (1975).
- ¹² T. Takahashi and O. Yamada, "Fluorescent Properties of Alkali and Alkaline Earth Rare Earth Metaphosphate Glass Phosphors," *RCA Review*, **41**, p. 65, March 1980 (this issue).
- ¹³ T. Takahashi and O. Yamada, To be published.
- ¹⁴ T. Takahashi and O. Yamada, "Luminescence of Certain Terbium Metaphosphate Glasses under X-Ray Excitation," *RCA Review*, **41**, p. 110, March 1980 (this issue).
- ¹⁵ W. W. Wendlandt, *Thermal Methods of Analysis*, John Wiley and Sons Inc., New York, (1964). Translated into Japanese in 1967, Sangyo Tosho Pub. Co., Ltd., Tokyo, pp. 317-321.

AUTHORS

Hilzu Fujita received his B.S. in Geophysics in 1955, his M.S. in Physical Meteorology in 1957, his M.S. in Radiation Science in 1959, and his Ph.D. in Physics in 1963, all from the University of Tokyo. From 1962 to 1966 he was a Research Associate at the Institute for Solid State Physics of the University of Tokyo where he studied transport phenomenon in insulators. From 1966 to 1969 he studied the optical properties of alkali halides using synchrotron radiation at the University of Illinois, where he served as a Research Assistant Professor in the Department of Physics. Since joining RCA Research Laboratories, Tokyo, in 1969, his interests have been the optical properties of semiconductors. He is a member of the Physical Society of Japan.



Michiko Inoue received her B.A. in Natural Science from the International Christian University in Tokyo in 1958, and her Ph.D. in Physics from Harvard University in 1964. From 1964 to 1969 she was a Research Associate at the Institute for Solid State Physics of the University of Tokyo. Dr. Inoue joined RCA Research Laboratories, Tokyo, in 1969. She is a member of the Physical Society of Japan.



Dalton H. Pritchard received the B.S.E.E. degree in Electronics in 1943, from Mississippi State University. Upon graduation he entered the U.S. Army Signal Corps. In 1946, Mr. Pritchard joined RCA Laboratories at Riverhead, N.Y., as a Member of the Technical Staff where he was engaged primarily in research activities in the area of single sideband, radio-teletype, multiplex communications systems. In 1950, he transferred to the RCA Laboratories in Princeton, N.J., and has been engaged, for a number of years, in research in many aspects of color television systems development, receivers, color kinescopes, transmitting encoders, cameras, magnetic recording of TV, and many associated systems and devices. This work included the planning and testing of systems and circuits proposed for adoption by the National Television Systems Committee (NTSC).



More recently, Mr. Pritchard has been engaged in research in the field of information Display Systems and Devices which has included activities in the related fields of vacuum preparation of materials, specialized electron-optic devices, lasers, the development of electro-optic materials and techniques for purposes of light control and display and color camera special systems development and evaluation. At present, he is engaged in the development and evaluation of video processing circuitry for color TV receivers, particularly in the areas of colorimetry and decoder matrix techniques. The development of analog techniques employing CCD devices for TV applications is included in his present activities.

In the period between 1952 and 1979, Mr. Pritchard received nine RCA Achievement Awards. He has numerous publications and has received over 35 issued patents, with others pending in the fields of Color Television and Information Display. In February, 1975, he was appointed Fellow, Technical Staff, RCA Laboratories. He was elected Fellow of the IEEE, Fellow of SID, and is a member of Sigma Xi, Tau Beta Pi, and Kappa Mu Epsilon and is listed in American Men of Science and Who's Who in the East. Mr. Pritchard was awarded the Vladimir K. Zworykin Award for "Significant Contributions to Color Television Technology," at the IEEE Consumer Electronics Spring Conference in Chicago, June 7, 1977.

Donald J. Sauer studied under a Regents Scholarship at the University of California at Los Angeles, and was awarded the BSEE magna cum laude in 1969. Upon graduation he joined RCA, Electromagnetic and Aviation Systems Division, in Van Nuys, California. There he was responsible for state-of-the-art circuit designs for audio amplifiers, power supplies, and encoding/decoding devices utilizing universal logic arrays. In 1973 he began working on charge-coupled digital memory devices intended for the replacement of rotating magnetic drums, and successfully designed and demonstrated experimental 4K-bit and 16K-bit CCD memories.



In 1974 Mr. Sauer transferred to RCA Laboratories, Princeton, N.J., as a Member of Technical Staff. He continued working on CCD technology and has been responsible for the design, layout, and characterization of charge-coupled devices for imaging, memory, and signal-processing applications. Mr. Sauer has published nine technical papers in the CCD area. He is the inventor or coinventor named in seven U.S. patents and has several patents pending. Mr. Sauer has received two RCA Laboratories Outstanding Achievement Awards. In 1976 he received the award for contributions to a team effort in developing and demonstrating the feasibility of charge-coupled delay-line techniques for video-signal processing applications, and in 1978 for contributions to a team effort in the application of charge-coupled devices in color television receivers.

Tatsuo Takahashi received his B.E. in Industrial Chemistry from the University of Tokyo, his M.S. in Materials Science from Northwestern University in 1964, and his Ph.D. in Materials Science from Stanford University in 1968. From 1958 to 1962 he was with the Onoda Cement Company where he did basic researches on portland cement and related materials. Since joining RCA Research Laboratories in 1968, he has studied the crystal growth and physical properties of phosphors. Dr. Takahashi is a member of the Physical Society of Japan and the Japan Society of Applied Physics.



Osamu Yamada received his B.S. degree from Kogakuin University in Tokyo in 1968. He joined RCA Research Laboratories in 1970. He was primarily engaged in material synthesis research. He is now studying the syntheses and luminescent properties of phosphor materials. He is a member of the Japan Society of Applied Physics.



Patents Issued to RCA Inventors—Fourth Quarter 1979

October

- D. F. Bowman Frequency-Scanned Antenna (4,170,778)
- A. G. Dingwall Integrated Gate Field Effect Transistors Having Closed Gate Structure With Controlled Avalanche Characteristics (4,173,022)
- R. A. Dischert Television Control System (4,170,024)
- H. R. Fecht Raster Distortion Correction Circuit (4,169,988)
- J. R. Harford Signal Attenuator (4,172,239)
- A. C. Ipri and J. H. Scott, Jr. Method for Making Silicon on Sapphire Transistor Utilizing Predeposition of Leads (4,169,746)
- R. W. Jebens Method of Fabrication of a Fresnel Lens (4,170,616)
- H. Khajezadeh Method of Making a Semiconductor Integrated Circuit Device Utilizing Simultaneous Outdiffusion and Autodoping During Epitaxial Deposition (4,170,501)
- W. A. Lagoni and J. B. Webb Burst Gate Circuit (4,173,023)
- A. J. Leidich Self-Biasing Amplifier Stage (4,172,999)
- F. J. Marlowe Multiple Standard Television Sync Generator (4,169,659)
- J. C. Turnbull Method for Coating Cathode Material on Cathode Substrate (4,170,811)
- J. R. Zuber Novel Solvent Drying Agent (4,169,807)

November

- A. P. Arntsen Coupling a Frequency Modulated Signal to a Tuned Load (4,173,743)
- W. E. Babcock and R. L. Hess Television S-Correction Linearity Device (4,176,303)
- R. B. Cornizzoli Chemically Treating the Overcoat of a Semiconductor Device (4,173,683)
- T. L. Credelle and F. W. Spong Recording a Synthetic Focused-Image Hologram on a Thermally Deformable Plastic (4,174,881)
- E. J. Denlinger and H. S. Veloric Contact for Semiconductor Devices (4,173,768)
- A. R. Dholakia Grooved Record Playback System (4,173,348)
- D. W. Flatley Method for Making Semiconductor Structure (4,174,217)
- L. D. Huff Toggle Mechanism for VideoDisc Player (4,175,751)
- H. Kressel and M. A. Spak Method of Defining Contact Openings in Insulating Layers on Semiconductor Devices without the Formation of Undesirable Pinholes (4,174,252)
- W. L. Lehmann Antenna Isolation Device (4,173,742)
- F. J. Marlowe and C. H. Anderson Flat Display Device (4,174,523)
- D. C. McCarthy and M. Rayl Printed Circuit Board with Increased Arc Track Resistance (4,174,531)
- H. M. Scott Regulating Television Horizontal Deflection Arrangement (4,176,304)
- R. P. Stone and A. M. Morrell Cathode-Ray Tube Having a Stepped Shadow Mask (4,173,729)
- M. Toda, Y. Matsumoto, and S. Osaka Signal Pickup Arm Lifting/Lowering and Groove Skipper Apparatus (4,176,378)

December

- L. Abbott System for Transmitting Two Color TV Signals (4,179,703)
- A. A. Ahmed Current Mirror Amplifier (30,173)
- R. C. Allig CRT with Field-Emission Cathode (4,178,531)
- W. J. Bachman, Jr. and F. R. Dimeo Plug-In Circuit Cartridge with Electrostatic Charge Protection (4,179,178)
- K. K. N. Chang Flat Cathode Ray Tube having Magnetically Collimated Electron Beam Device (4,180,760)
- W. Denhollander Raster Correction Circuit with Low Dissipation Resistive Damping (4,179,642)
- D. W. Flatley Process of Making a Planar MOS Silicon-on-Insulating Substrate Device (4,178,191)
- G. Forster Drive Circuit for a Television Deflection Output Transistor (4,177,393)
- P. E. Haferl Current Switching Networks (4,177,392)
- J. M. Hammer and C. C. Neil Fiber-Optic Thermometer (4,176,551)
- J. M. Hammer Fiber-Optic Thermometer (4,176,552)
- S. T. Hsu and J. M. Cartwright, Jr. Complementary MOS Inverter Structure (4,178,605)
- K. C. Hudson and D. G. Herzog Optical Scanner and Recorder (4,180,822)
- L. R. Hulls and T. Dowdell, Jr. Alternator Test Apparatus and Method (4,178,546)
- M. R. Johns Circularly Polarized Antenna System Using a Combination of Horizontal and Bent Vertical

Dipole Radiators (4, 180,820)

L. A. Kaplan Biasing and Drive Circuitry for Quasi-Linear Transistor Amplifiers (4, 180,781)

L. A. Kaplan Phantom Full-Bridge Amplifier (4, 180,782)

J. R. Khalifa Phase Lock Loop Data Timing Recovery Circuit (4, 180,783)

I. Ladany, M. Ettenberg, H. Kressel, and H. F. Lockwood Half Wave Protection Layers on Injection Lasers (4, 178,564)

J. S. Levin Flow Controller (4, 178,974)

H. E. McCandless Method for Establishing Uniform Cathode-to-Grid Spacing in an Electron Gun (4, 176,432)

G. H. Olsen and M. Ettenberg Low Cost High Efficiency Gallium Arsenide Homojunction Solar Cell Incorporating a Layer of Indium Gallium Phosphide (4, 179,308)

M. A. Pollnsky Method of Making a Bipolar Transistor with High-Low Emitter Impurity Concentration (4, 178,190)

W. R. Roach Depth Estimation System Using Diffractive Effects of the Grooves and Signal Elements in the Grooves (4, 180,830)

D. J. Sauer Readout of a Densely Packed CCD (4, 178,614)

P. Sheng and A. H. Firester Optical Playback System having Increased Depth-of-Field (4, 179,708)